DEPARTMENT OF TRANSPORTATION

Ten-Year Review of Monitoring System on I-35W Saint Anthony Falls Bridge

Lauren Linderman, Principal Investigator
Civil, Environmental, and Geo- Engineering
University of Minnesota

JUNE 2020

Research Project
Final Report 2020-19

To request this document in an alternative format, such as braille or large print, call 651-366-4718 or 1-800-657-3774 (Greater Minnesota) or email your request to ADArequest.dot@state.mn.us. Please request at least one week in advance.

Technical Report Documentation Page

1. Report No. MN 2020-19	2.	3. Recipients Accession No.
4. Title and Subtitle Ten-Year Review of Monitoring System on I-35W Saint Anthony Falls Bridge		5. Report Date June 2020 6.
7. Author(s) Riley J. Brown, Rebekka McCoy, Carol K. Shield, Lauren E. Linderman, Brock D. Hedegaard		8. Performing Organization Report No.
9. Performing Organization Name and Address Department of Civil, Environmental, and Geo- Engineering University of Minnesota 500 Pillsbury Drive SE Minneapolis, MN 55455		10. Project/Task/Work Unit No. CTS #2019001 11. Contract (C) or Grant (G) No. (c) 1003325 (wo) 78
12. Sponsoring Organization Name and Address Minnesota Department of Transportation Office of Research & Innovation 395 John Ireland Boulevard, MS 330 St. Paul, Minnesota 55155-1899		13. Type of Report and Period Covered Final Report 14. Sponsoring Agency Code
15. Supplementary Notes http://mndot.gov/research/reports/2020/202019.pdf		

16. Abstract (Limit: 250 words)

The I-35W St. Anthony Falls bridge was highly instrumented with over 500 sensors to verify design assumptions, serve as a testbed to examine bridge sensing techniques, and evaluate the effectiveness of different bridge monitoring strategies. The instrumentation deployed on the bridge to investigate the structural behavior included vibrating wire strain gages (VWSGs), thermistors, fiber optic sensors (SOFO), resistance strain gages, linear potentiometers, accelerometers, and corrosion monitoring sensors. This report documented the successes and challenges of the monitoring program over the first ten years of the bridge's life. In particular, the effectiveness of different strain measurement techniques and sensor distributions were addressed. Previous investigations of temperature-dependent and time-dependent behavior were also expanded with the larger data set to better understand the behavior of post-tensioned concrete box girder structures with the potential to impact future designs.

17. Document Analysis/Descriptors I-35W Saint Anthony Falls Bridge, structural health monitoring		18. Availability Statement No restrictions. Document available from: National Technical Information Services, Alexandria, Virginia 22312	
19. Security Class (this report) Unclassified	20. Security Class (this page) Unclassified	21. No. of Pages 125	22. Price

TEN-YEAR REVIEW OF MONITORING SYSTEM ON I-35W SAINT ANTHONY FALLS BRIDGE

FINAL REPORT

Prepared by:

Riley J. Brown
Rebekka McCoy
Carol K. Shield
Lauren E. Linderman
Department of Civil, Environmental, and Geo- Engineering
University of Minnesota

Brock D. Hedegaard
Civil Engineering Department
University of Minnesota Duluth

June 2020

Published by:

Minnesota Department of Transportation
Research Services & Library
395 John Ireland Boulevard, MS 330
St. Paul, Minnesota 55155-1899

This report represents the results of research conducted by the authors and does not necessarily represent the views or policies of the Minnesota Department of Transportation or the University of Minnesota. This report does not contain a standard or specified technique.

The authors, the Minnesota Department of Transportation, and the University of Minnesota do not endorse products or manufacturers. Trade or manufacturers' names appear herein solely because they are considered essential to this report.

ACKNOWLEDGMENTS

Numerical computations were performed using resources provided by the University of Minnesota Supercomputing Institute.

TABLE OF CONTENTS

CHAPTER 1: Introduction **1**

CHAPTER 2: Bridge Description **2**

CHAPTER 3: Instrumentation and system performance **3**

3.1 Static System 3

3.2 Dynamic System 6

3.3 Fiber Optic Strain Gages (SOFO) 9

3.4 Corrosion Monitoring System (CorSenSys) 10

3.5 Summary of instrumentation performance 11

CHAPTER 4: Comparison of Static Strain Data **12**

4.1 Vibrating Wire Strain Gage Data from Superstructure 12

4.2 Fiber Optic Strain Gage (SOFO) Data 23

4.3 Curvature Comparison between VWSG and SOFO Gages 27

4.4 Conclusion 32

CHAPTER 5: Investigation of Thermal Gradient Effects **33**

5.1 Thermal Gradients Background 33

5.2 Comparison of Measured and Design Thermal Gradients 36

5.2.1 Comparison of Gradient Magnitudes 37

5.2.2 Comparison of Gradient Shapes 41

5.3 Modeling of Design and Measured Thermal Gradients 45

5.3.1 FEM Material Properties 46

5.3.2 Applied Thermal Gradients 47

5.3.3 Thermal Gradient Stress Results 49

5.4 Thermal Gradient Conclusions 51

CHAPTER 6: Long-Term Time-Dependent Behavior of As-Built Structure 52

6.1 Time-Dependent Displacements 53

6.2 Time-Dependent Strains 63

6.3 Conclusion 71

CHAPTER 7: Service load stresses 72

7.1 Service Loads 72

7.2 Stress Results 73

7.3 Service Load Stress Conclusions 76

CHAPTER 8: Conclusions and Recommendations 78

8.1 Summary and Conclusions 78

8.2 Evaluation and Recommendations for Instrumentation 79

8.3 Evaluation and Recommendations for Design 80

Appendix A Monitoring System Outages and Maintenance

Appendix B Linear Potentiometer Monitoring System Checks through April 18, 2019

LIST OF FIGURES

Figure 2.1: Elevation view of the I-35W Saint Anthony Falls Bridge (French et al. 2012) 2

Figure 3.1: Elevation view of the adjacent bridges showing VWSG Locations 3, 4, 5, 6, 7, 8, 9, 14, and 15 (French et al. 2012). 6

Figure 3.2: Thermistor layout (French et al. 2012) 6

Figure 3.3: Long-term accelerometer layout used from May 11, 2010 until present (French et al. 2012) 8

Figure 3.4: Typical linear potentiometer installations at Abutment 1 and Pier 4 (French et al. 2012). 9

Figure 3.5: Elevation view of the adjacent bridges showing SOFO sensor locations (French et al. 2012). 10

Figure 3.6: Typical SOFO sensor layout (French et al. 2012). 10

Figure 4.1: Relative mechanical strain plus creep and shrinkage strains for gages VS03ETL4 (blue; longitudinal gage in top flange at southbound Location 3) and VS03EBL3 (red; longitudinal gage in bottom flange at southbound Location 3). 14

Figure 4.2: Relative mechanical strain plus creep and shrinkage strains for gages VS04ETL1 (blue; longitudinal gage in top flange at southbound Location 4) and VS04EBL2 (red; longitudinal gage in bottom flange at southbound Location 4). 14

Figure 4.3: Relative mechanical strain plus creep and shrinkage strains for gages VS05ITL1 (blue; longitudinal gage in top flange at southbound Location 5) and VS05IBL1 (red; longitudinal gage in bottom flange at southbound Location 5). 15

Figure 4.4: Relative mechanical strain plus creep and shrinkage strains for gages VS07ETL6 (blue; longitudinal gage in top flange at southbound Location 7) and VS07EBL3 (red; longitudinal gage in bottom flange at southbound Location 7). 15

Figure 4.5: Relative mechanical strain plus creep and shrinkage strains for gages VS08ITL1 (blue; longitudinal gage in top flange at southbound Location 8) and VS08IBL1 (red; longitudinal gage in bottom flange at southbound Location 8). 16

Figure 4.6: Relative mechanical strain plus creep and shrinkage strains for gages VS09ETL1 (blue; longitudinal gage in top flange at southbound Location 9) and VS09EBL1 (red; longitudinal gage in bottom flange at southbound Location 9). 16

Figure 4.7: Relative mechanical strain plus creep and shrinkage strains for gages VS14ITL1 (blue; longitudinal gage in top flange at southbound Location 14) and VS14IBL1 (red; longitudinal gage in bottom flange at southbound Location 14). 17

Figure 4.8: Relative mechanical strain plus creep and shrinkage strains for gages VS15ETL1 (blue; longitudinal gage in top flange at southbound Location 15) and VS15EBL1 (red; longitudinal gage in bottom flange at southbound Location 15). 17

Figure 4.9: Relative mechanical strain plus creep and shrinkage strains for gages VN03ITL1 (blue; longitudinal gage in top flange at northbound Location 3) and VN03IBL1 (red; longitudinal gage in bottom flange at northbound Location 3). 18

Figure 4.10: Relative mechanical strain plus creep and shrinkage strains for gages VN05ETL1 (blue; longitudinal gage in top flange at northbound Location 5) and VN05EBL1 (red; longitudinal gage in bottom flange at northbound Location 5). 18

Figure 4.11: Relative mechanical strain plus creep and shrinkage strains for gages VN07ETL1 (blue; longitudinal gage in top flange at northbound Location 7) and VN07EBL1 (red; longitudinal gage in bottom flange at northbound Location 7). 19

Figure 4.12: Relative mechanical strain plus creep and shrinkage strains for gages VN08ETL1 (blue; longitudinal gage in top flange at northbound Location 8) and VN08EBL1 (red; longitudinal gage in bottom flange at northbound Location 8). 19

Figure 4.13: Relative mechanical strain plus creep and shrinkage strains for gages VN09ETL1 (blue; longitudinal gage in top flange at northbound Location 9) and VN09EBL1 (red; longitudinal gage in bottom flange at northbound Location 9). 20

Figure 4.14: Relative mechanical strain plus creep and shrinkage strains for gages VN14ETL1 (blue; longitudinal gage in top flange at northbound Location 14) and VN14EBL1 (red; longitudinal gage in bottom flange at northbound Location 14). 20

Figure 4.15: Relative mechanical strain plus creep and shrinkage strains for gages VN15ITL1 (blue; longitudinal gage in top flange at northbound Location 15) and VN15IBL1 (red; longitudinal gage in bottom flange at northbound Location 15). 21

Figure 4.16: Relative mechanical strain plus creep and shrinkage strains for gages VS07EEV2 (blue; vertical gage at interior face of east web of exterior box, southbound Location 7) and VS07EEV3 (red; vertical gage at exterior face of east web of exterior box, southbound Location 7). 21

Figure 4.17: Relative mechanical strain plus creep and shrinkage strains for gages VS07ETT1 (blue; top transverse gage in top flange at southbound Location 7) and VS07ETT2 (red; bottom transverse gage in top flange at southbound Location 7). 22

Figure 4.18: Relative mechanical strain plus creep and shrinkage strains for gages VS07EBT1 (blue; top transverse gage in bottom flange at southbound Location 7) and VS07EBT2 (red; bottom transverse gage in bottom flange at southbound Location 7). 22

Figure 4.19: Relative mechanical strain plus creep and shrinkage strains for gages 6aT_7014 (blue; longitudinal gage on top flange at southbound Location 6a) and 6aB_7016 (red; longitudinal gage on bottom flange at southbound Location 6a). 24

Figure 4.20: Relative mechanical strain plus creep and shrinkage strains for gages 6eT_7012 (blue; longitudinal gage on top flange at southbound Location 6e) and 6eB_7010 (red; longitudinal gage on bottom flange at southbound Location 6e). 25

Figure 4.21: Relative mechanical strain plus creep and shrinkage strains for gages 6iT_7007 (blue; longitudinal gage on top flange at southbound Location 6i) and 6iB_7005 (red; longitudinal gage on bottom flange at southbound Location 6i). 25

Figure 4.22: Relative mechanical strain plus creep and shrinkage strains for gages 7bT_7008 (blue; longitudinal gage on top flange at southbound Location 7b) and 7bB_7006 (red; longitudinal gage on bottom flange at southbound Location 7b). 26

Figure 4.23: Relative mechanical strain plus creep and shrinkage strains for gages 7gT_7011 (blue; longitudinal gage on top flange at southbound Location 7f) and 7gB_7009 (red; longitudinal gage on bottom flange at southbound Location 7f). 26

Figure 4.24: Relative mechanical strain plus creep and shrinkage strains for gages 7jT_7015 (blue; longitudinal gage on top flange at southbound Location 7j) and 7jB_7013 (red; longitudinal gage on bottom flange at southbound Location 7j). 27

Figure 4.25: Comparisons of VWSG and SOFO curvatures from truck test STI3SB on September 2008 and October 2010 on southbound bridge. 29

Figure 4.26: Comparisons of VWSG and SOFO curvatures from truck test STI6SB on September 2008 and October 2010 on southbound bridge. 30

Figure 4.27: Comparisons of VWSG and SOFO curvatures from truck test STI7SB on September 2008 and October 2010 on southbound bridge. 31

Figure 4.28: Change in curvature from minimum positive thermal gradient to maximum positive thermal gradient on April 20, 2014. 31

Figure 5.1: Comparison of AASHTO LRFD (2017) and New Zealand (Priestly 1978) positive design gradients (French et al. 2012). AASHTO LRFD (2017) design gradients are the same as those specified in AASHTO LRFD (2010). 35

Figure 5.2: Characteristic section dimensions and instrumentation layout in southbound structure Location 7 (French et al. 2012). 36

Figure 5.3: Postive and negative design gradients considered for comparison to measured thermal gradients at southbound Location 7 of the southbound structure. Priestley Linear only prescribed for decks above enclosed air cells in box girders. 37

Figure 5.4: Measured (a) positive and (b) negative gradient magnitudes: design gradient magnitudes considered at a depth of 2 in. (50 mm) below the deck surface for comparison against measured gradients. 39

Figure 5.5: Number of days per month with measured (a) positive and (b) negative gradient magnitudes exceeding the AASHTO LRFD design gradient magnitude at a depth of 2 in. (50 mm) below the deck surface. 39

Figure 5.6: Daily maximum positive gradient magnitude as a function of time. Each subplot represents the hour of the day on which the daily maximum positive gradient occurred. Within each plot, the histogram shows the number of days (count) on which the daily maximum positive gradient magnitude was within a certain temperature range. The vertical dashed line represents the AASHTO LRFD (2017) positive gradient magnitude. 40

Figure 5.7: Daily maximum negative gradient magnitude as a function of time. Each subplot represents the hour of the day on which the daily maximum negative gradient occurred. Within each plot, the histogram shows the number of days (count) on which the daily maximum negative gradient magnitude was within a certain temperature range. The vertical dashed line represents the AASHTO LRFD (2017) negative gradient magnitude. 41

Figure 5.8: Maximum measured positive gradients at southbound Location 7 compared with design gradients through (a) centerline of exterior box, top flange only, and (b) along centerline of west web of exterior box. 43

Figure 5.9: Maximum measured negative gradients at southbound Location 7 compared with design gradients through (a) centerline of exterior box, top flange only, and (b) along centerline of west web of exterior box. 43

Figure 5.10: Measured temperature profiles at the time of (a) the maximum measured positive gradient (5/7/2013 2:00 PM) and (b) the maximum measured negative gradient (1/10/2016 8:00 AM) through the west web of the exterior box and the east web of the interior box at southbound Location 7. 44

Figure 5.11: Measured temperature in top and bottom flanges along the length of the southbound superstructure on July 1, 2011 at 3:00 PM. Corresponds to maximum measured positive gradient over first three years of monitoring (French et al. 2012). 44

Figure 5.12: Simplifications of negative measured thermal gradient. 49

Figure 5.13: Design thermal gradient stresses for FEM model with measured material properties. 50

Figure 5.14: Design thermal gradient stresses for FEM model with nominal material properties. 50

Figure 5.15: Negative thermal gradients stresses using FEM model with measured material properties. 51

Figure 6.1: Average bridge temperature determined by an area-weighted average of thermistor data at the midspan of southbound Span 2 (Location 7). 53

Figure 6.2: Measured and time-dependent LP displacements plotted with respect to unadjusted time. 56

Figure 6.3: Southbound Span 1 time-dependent LP displacements for various assumed time-dependent models plotted with respect to unadjusted time. 57

Figure 6.4: Time-dependent LP displacements plotted with respect to unadjusted time. 57

Figure 6.5: Comparison of estimated time-dependent longitudinal deflections with linear potentiometer data from southbound bridge Span 1. 58

Figure 6.6: Comparison of estimated time-dependent longitudinal deflections with linear potentiometer data from southbound bridge Span 3. 59

Figure 6.7: Comparison of estimated time-dependent longitudinal deflections with linear potentiometer data from southbound bridge combined Span 1 and Span 3. 60

Figure 6.8: Comparison of estimated time-dependent longitudinal deflections with linear potentiometer data from northbound bridge Span 1. 61

Figure 6.9: Comparison of estimated time-dependent longitudinal deflections with linear potentiometer data from northbound bridge Span 3. 62

Figure 6.10: Comparison of estimated time-dependent longitudinal deflections with linear potentiometer data from northbound bridge combined Span 1 and Span 3. 63

Figure 6.11: Time-dependent strains extracted from vibrating wire strain gage data by linear regression plotted with respect to unadjusted time. 66

Figure 6.12: Time-dependent strains extracted from various size vibrating wire strain gage data sets plotted with respect to unadjusted time. 66

Figure 6.13: Comparison of measured longitudinal time-dependent strains to those computed with FEM using all considered time-dependent models at Location 3 of southbound bridge. 67

Figure 6.14: Comparison of measured longitudinal time-dependent strains to those computed with FEM using all considered time-dependent models at Location 5 of southbound bridge. 68

Figure 6.15: Comparison of measured longitudinal time-dependent strains to those computed with FEM using all considered time-dependent models at Location 7 of southbound bridge. 69

Figure 6.16: Comparison of measured longitudinal time-dependent strains to those computed with FEM using all considered time-dependent models at Location 8 of southbound bridge. 70

Figure 6.17: Comparison of measured longitudinal time-dependent strains to those computed with FEM using all considered time-dependent models at Location 9 of southbound bridge. 70

Figure 7.1: Tensile stress in the bottom flange at midspan due to positive thermal gradient, service load combination I 75

Figure 7.2: Tensile stress in the top flange at midspan due to negative thermal gradient, service load combination I or III 76

LIST OF TABLES

Table 5.1: Dates, times, and weather conditions for maximum measured positive thermal gradients during the first ten years of monitoring 45

Table 5.2: Dates, times, and weather conditions for maximum measured negative thermal gradients during the first ten years of monitoring. 45

Table 5.3: Modeled material properties – measured case. 47

Table 5.4: Modeled material properties – nominal case. 47

Table 5.5: Thermal gradients applied to finite element model. 49

Table 7.1: Tensile stress in bottom flange at midspan due to positive thermal gradient, service load combination I 75

Table 7.2: Tensile stress in top flange at midspan due to negative thermal gradient, service load combination I or III 76

Table A1: Monitoring system data outages

EXECUTIVE SUMMARY

When the I-35W St. Anthony Falls Bridge was replaced in 2008, the Minnesota Department of Transportation (MnDOT) decided to highly instrument the bridge and use it as a testbed to examine bridge sensing and evaluate the effectiveness of different bridge monitoring strategies. To achieve this goal, the I-35W St. Anthony Falls Bridge was instrumented with more than 500 sensors to capture structural behavior. Measurements for strain, longitudinal bridge displacement, bridge accelerations, temperature, and corrosion were included in the system.

The replacement bridge was constructed as two post-tensioned concrete box girder bridges, one carrying the northbound traffic and one carrying the southbound traffic, built adjacent to each other. The four-span, two-wide box construction of each bridge consisted of a mix of segmental precast and cast-in-place concrete. The southern three spans of each bridge were designed as continuous with an expansion joint separating the fourth (northern most) span from the other three spans. The three span continuous part of the structure was where the instrumentation was placed during construction.

This report documents the successes and challenges of the monitoring program over the first ten years of the bridge's life. In particular, the effectiveness of different strain measurement techniques and sensor distributions were addressed. The larger data set was used to expand the previous investigations of temperature-dependent and time-dependent behavior to better understand the behavior of post-tensioned concrete box girder structures with the potential to impact future designs.

The instrumentation deployed on the bridge to investigate the structural behavior included vibrating wire strain gages (VWSGs), thermistors, fiber optic sensors (SOFO), resistance strain gages, linear potentiometers, accelerometers, and corrosion monitoring sensors. Overall, the instrumentation survival rate of approximately 90% over the ten years was significant given the deployment duration, embedment of gages, and variety of sensor systems. Some of the instrumentation systems had greater losses than others; the linear potentiometers required numerous replacements and the corrosion monitoring system did not function properly. Throughout the ten years, there were significant losses of data from the system that measures the bridge longitudinal displacement. Many of these system failures were assumed to be due to lightning strikes on the bridge. Several changes to this system were made to try to electronically isolate the measurement system from any stray lightening currents. Eventually, the incidence of system failure related to electrical storms was greatly reduced.

The measurement systems were leveraged in different ways throughout the monitoring process. The strain measurements were used to calibrate the Finite Element Method (FEM) model used for behavior comparisons and to validate assumptions. For long-term monitoring, the temperature-corrected expansion and contraction of spans 1-3 of the bridge has provided the most valuable information regarding time-dependent effects and expected behavior.

Thermal gradients were extracted from the temperature data measured along the southbound structure. The heavily instrumented midspan location allowed for comparison of the gradient shapes along the depth of the section. The data emphasized that the New Zealand design gradients scaled to

AASHTO Zone 2 most effectively captured the temperature behavior in both gradient shape and magnitude. The thermal gradients, both measured and design, were applied to the previously developed 2D FEM model to quantify the corresponding temperature stress demands along the length. Although the conservative assumptions in this structure seemed to be adequate, the large thermal stresses could be significant for serviceability considerations in other bridge structures, particularly cracking of the deck in negative moment areas.

The time-dependent behavior of the I-35W Bridge was extracted from the measured bridge expansion and strain gage data, which contain both time- and temperature-related deformations. The time-dependent response of the southbound structure was compared to predicted behavior based on several time-dependent models applied to the finite element model of the bridge. Depending on the location, the measured time-dependent behavior was best approximated by the ACI 209 and 1990 CEB/FIP code models. The measured data were conservative with respect to the 1978 CEB/FIP Model code used in the bridge design.

The measurements collected over the ten years of monitoring, with the aid of material tests, truck tests, and finite element modeling, provided insight regarding the relative strengths of the instrumentation systems and potential considerations for future deployments.

The temperature loading and response of the structure was determined to be essential to understanding structural behavior; as a result, the thermistors, vibrating wire strain gages, and bearing displacements were considered the most important for long-term monitoring of these stiff concrete structures. However, leveraging one heavily instrumented cross-section to capture the temperature distribution throughout the structure limited the ability to interpret structural behavior near the piers, where the cross section varies significantly. Additional cross sections with temperature measurements would provide a more accurate representation of the temperature distribution throughout the structure. This could be essential as the temperature-dependent behavior starts to dominate the system response over initial creep and shrinkage.

In future monitoring system deployments, several considerations during design and installation will improve performance and the evaluative power of the data. The electrical grounding and ease of power cycling should be carefully considered in the system design to limit outages and associated downtime due to electrical storms. Having researchers on site during sensor installation will limit errors due to location uncertainty and labeling. In addition, researchers should be on site for initial measurements to ensure that complete data is captured, which would then allow for absolute strains to be determined, instead of just changes in strain.

CHAPTER 1: INTRODUCTION

The I-35W St. Anthony Falls Bridge monitoring system has operated since construction of the structure, which opened to traffic on September 18, 2008. The operation of the system for over ten years is one of the longest continuous monitoring systems (Webb et al. 2014). The monitoring system deployed incorporates many sensor types, including strain, temperature, acceleration and displacement sensors, and has generated a uniquely large data set. This data set offers an unmatched opportunity to evaluate long-term monitoring approaches.

The design and long-term performance of post-tensioned concrete bridges are highly affected by time-dependent and temperature-dependent behavior. The expected in-situ behavior is challenging to predict given the large thermal gradients experienced in Minnesota and the conflicting time-dependent displacement models that form the basis for different design codes. The I-35W St. Anthony Falls Bridge monitoring system allows for the behavior of the as-built structure to be determined and compared with existing design and behavior models.

Previous work with the I-35W monitoring system has provided essential understanding of the time-dependent and temperature-dependent behavior of post-tensioned concrete bridges (French et al. 2012; French et al. 2014). Assessment of the data through the first three years of the deployment showed that the 1990 CEB/FIP Model Code and ACI-209 models best predicted the in-situ creep/shrinkage behavior and that there were no long-term concerns with excessive deflections after three years of monitoring. The assessment also found that temperature-dependent behavior was significant for modeling time-dependent deflections and can account for significant strains. These results informed the design and operation of a short-term and long-term monitoring algorithm.

The research conducted for this project focused on a ten-year review of the I-35W Bridge monitoring system to analyze the time-dependent and temperature-dependent behavior of the as-built structure and to provide insight on how to effectively monitor structures. Specifically, the research focused on four main components: long-term system and sensor performance, strain measurement approaches, thermal gradients, and long-term time-dependent deformations. The summary of the system's performance addressed both the successes and challenges of operating a large-scale monitoring system over ten years. The previous analysis of the thermal gradients and time-dependent behavior was updated with the extended data to characterize the significance of these findings for future bridge designs.

The report is organized as follows: Chapter 2 contains a description of the bridge; Chapter 3 describes the instrumentation and summarizes the sensing system performance; Chapter 4 compares the vibrating strain gage and fiber optic strain gage data; Chapter 5 presents the measured thermal gradients, as well as the corresponding thermal stresses, in comparison with the American Association of State Highway and Transportation Officials (AASHTO) and New Zealand design codes; Chapter 6 presents an extended analysis of the time-dependent strain and displacement behavior and compares the as-built response to the predicted behavior from several existing models; and Chapter 7 summarizes the conclusions from the report.

CHAPTER 2: BRIDGE DESCRIPTION

The I-35W Saint Anthony Falls Bridge, which opened to traffic on September 18, 2008, is a post-tensioned concrete box girder bridge comprised of two separate structures built adjacent to each other: a northbound bridge and a southbound bridge. Figure 2.1 shows an elevation view of the bridge. Each structure contains four spans numbered in ascending order from south to north, with the main span (Span 2) crossing the Mississippi River. The span lengths for each bridge are also provided in Figure 2.1. In total, each bridge is 90 ft-4 in (27.5 m) wide and carries five 12 ft (3.7 m) lanes of traffic with a 13 ft (4.0 m) wide shoulder on the exterior side of the bridge and a 14 ft (4.3 m) wide shoulder on the interior side of the bridge. The bridge was designed to accommodate future contingency dead and live loads, such as light-rail train along the interior shoulder and a pedestrian bridge hanging beneath the superstructure.

The first three spans of the bridge are continuous, with the fourth span separate. The bridge design includes an expansion joint at the south end of Span 1, pins at Piers 2 and 3, and another expansion joint at the north end of Span 3 (south side of Pier 4). Span 4 is pinned on the south end (north side of Pier 4) and built integrally with Abutment 5 at the north end.

The main span was constructed using segmental precast construction while the other spans were cast-in-place. In Spans 1, 2, and 3, each bridge design consists of two boxes with varying depth, which are approximately 25 ft (7.6 m) deep near the pier and approximately 11 ft (3.4 m) deep at the midspan. The width between the inner sides of the webs at the top of the boxes is 21 ft-2 in. (6.5 m). The thinnest portion of the top flange across the width of the section has a nominal thickness of 11.5 in. (0.29 m) and remains constant along the entire length of Spans 1, 2, and 3. The bottom flange is 9 in. (0.23 m) thick at midspan of Span 2 and increases to 4 ft-10 in. (1.5 m) thick near each pier in Span 2. The bottom flange of Span 1 and Span 3 vary similarly. The webs are 1 ft-4 in. (0.41 m) thick in Spans 1 and 2, and 2 ft (0.61 m) thick in Span 3. The northbound and southbound bridge designs have similar cross sections for Spans 1 and 2 but differ in Span 3 where the north end of northbound Span 3 widens to allow for exiting traffic onto University Avenue. The design of Span 4 consists of two multi-celled boxes for each bridge. The northbound bridge contains three cells per box while the southbound bridge contains two cells per box in Span 4.

A detailed bridge description, including the construction sequence of both structures, is presented in French et al. (2012).

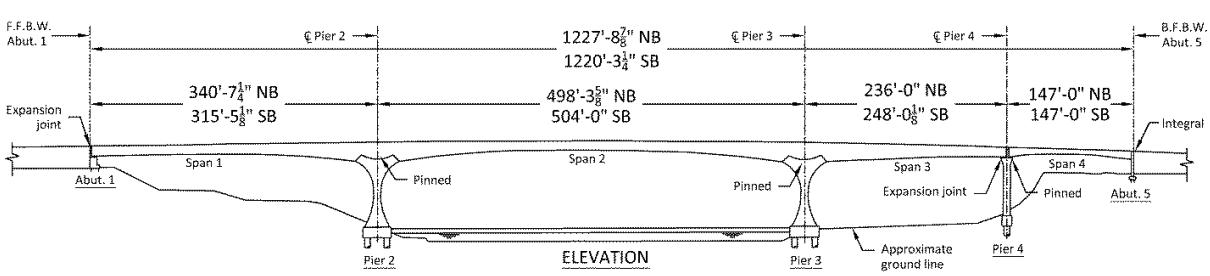

Figure 2.1: Elevation view of the I-35W Saint Anthony Falls Bridge (French et al. 2012)

CHAPTER 3: INSTRUMENTATION AND SYSTEM PERFORMANCE

Over 500 sensors were deployed on the bridge to investigate the structural behavior, including vibrating wire strain gages (VWSGs), thermistors, fiber optic sensors (SOFO), resistance strain gages, linear potentiometers, accelerometers, and corrosion monitoring sensors. The VWSGs and thermistors were wired to a slow-rate data acquisition system, referred to as the "static" system. Resistance strain gages, accelerometers, and the linear potentiometers were wired to a system capable of high data acquisition rates, termed the "dynamic" system. The SOFO sensor data was collected with a slow-rate data acquisition system; however, these same gages could be attached to a data processing system capable of dynamic rates. The instrumentation of the bridge is detailed in the MnDOT report "Instrumentation, Monitoring, and Modeling of the I-35W Bridge" by French et al. (2012).

This chapter provides a summary of the sensing system performance, and addresses both the successes and challenges of operating a large-scale monitoring system over ten years. A list of system outages and other maintenance issues are given in Appendix A.

3.1 STATIC SYSTEM

The static system originally contained 148 vibrating wire strain gages (VWSGs) and 48 thermistors in total deployed on both the northbound and southbound superstructures, and an additional 50 VWSGs located in the piers and drilled shafts of southbound Pier 2. Each VWSG had an integral thermistor to measure the temperature at the location where the strain is read. Most of the VWSGs were cast within the concrete; however, some VWSGs were mounted externally as replacements of malfunctioning embedded strain gages or because the final gage locations were not determined prior to casting. All thermistors were embedded in the concrete. Figure 3.1 shows the superstructure locations of static system instrumentation on the elevation view of the bridge. The vibrating wire strain gages have been used to monitor static strain in the concrete, which can be used to compute changes in curvature and estimate changes in stress. The thermistors have been used to provide information on the thermal gradients through the cross section of the bridge and have been instrumental for implementation of the linear potentiometer monitoring system developed in French et al. (2014).

During construction of the bridge, data was collected from only the substructure portion of the static system gages. The gages located in the southbound Pier 2 and associated drilled shafts were analyzed by the University of South Florida (USF) throughout the construction process to monitor the construction loads in the foundation as well as the axial deformations and curvature of the southbound Pier 2. The strain data from the drilled shafts was not believed to provide results relevant to monitoring the structure after construction was complete; therefore, data from the drilled shaft gages have not been analyzed in further detail. For this project, focus was placed on the long-term monitoring efforts of the superstructure and does not include construction data, which is specifically addressed in Collins et al. (2014).

The majority of the VWSGs were located in just a few sections of the bridge to provide a more thorough understanding of the behavior of the bridge at those locations. VWSGs were placed in at least the top and bottom flanges at southbound structure Locations 3, 4, 5, 6, 7, 8, 9, 14, and 15 and northbound structure Locations 3, 5, 6, 7, 8, 14, and 15. The heavily instrumented sections included Location 3 (near midspan of Span 1), Location 4 (negative moment region just to the south of the Pier 2 diaphragm section), Location 5 (negative moment region just to the north of the Pier 2 diaphragm section), and Location 7 (near midspan of Span 2 within the precast segment adjacent to the closure pour). The assumption was that, if the behavior at those locations could be well understood and modeled with a finite element model, then the model could be used to infer the behavior at other locations. Most of the VWSGs were oriented longitudinally within the bridges, and the bulk of the VWSG instrumentation was located within the exterior box of the southbound bridge.

The individual thermistors were used in conjunction with the VWSG thermistors to provide information on the thermal gradients through the cross section of the bridge. Of the 48 total individual thermistors installed in both structures, 42 were located at midspan of Span 2 of the southbound bridge. The remaining six were located at midspan of Span 2 of the northbound bridge. Figure 3.2 shows the thermistor layout at Location 7 of the northbound and southbound structures.

Of the 148 VWSGs installed in the superstructure, 134 survived installation and casting of the concrete (90.5% survival). Twelve of the nonoperational VWSGs were replaced with externally mounted VWSGs on May 11, 2010 and June 18, 2010, of which nine provided reasonable data values. Five gages were deemed unrecoverable due to either multiplexer connection problems, impossibility of replacement, or anchorage difficulties.

Four thermistors of the 48 originally installed did not survive installation (91.7% survival). No repairs were performed on any thermistors, as it was not feasible to embed new gages in the concrete, and external gages would not provide the information necessary for investigating thermal gradients through the concrete. A set of six thermistors intended to measure gradients above the east web of the interior box of the southbound structure at midspan of Span 2 had an uncertain location, and therefore were not used for investigation of thermal gradients.

As mentioned in French et al. (2012), a source of uncertainty in the VWSG and thermistor installation was the gage locations themselves. The contractor installed the gages, and did so largely when UMN personnel were not present, so gage location measurements were provided to the UMN. However, ambiguous as-built measurements required the true location to be interpreted and discussed with the contractor, which left some uncertainties as to the accuracy of the coordinates. Additional uncertainty was associated with the orientation of each VWSG, as some were not installed as desired.

Additionally, French et al. (2012) noted that certain VWSGs and thermistors were found to be wired incorrectly, as deduced by analyzing the data, so efforts were required to assign the correct channels to each sensor. These channel assignments were to the best of the researcher's knowledge, but other unknown wiring issues may still be present.

French et al. (2012) provides a complete list of static system sensor wiring, replacements, and initial operational status; no VWSGs or thermistors have been replaced since, and the operational status of the individual sensors remains mostly the same.

The static data collection system has been reliable. There have been three periods of data loss, caused by (1) a malfunction in the power supplies to media converters for both dataloggers, (2) a bad battery for the northbound datalogger, and (3) a faulty media converter for the southbound datalogger. Datalogger battery voltage is now monitored via weekly emails so the batteries can be replaced before any data loss occurs.

Initial static strain data was not effectively recorded. Strain readings were recorded at the time of installation of the gages and typically at a “24 hour” reading around a day after the concrete at the gage location had been poured, but the temperature associated with this strain reading was not recorded. Individual thermistors were also recorded with a “24 hour” reading. Without the reference temperature associated with the initial VWSG data, the initial strain reading was of no value and thus the total strain could not be determined from the gages. Because of this limitation, all long-term monitoring efforts using the VWSG data were based on relative strains. Strain measurements from the VWSGs are presented in Chapter 4.

Initially, static system data was sampled once every six hours (at midnight, 6:00 AM, noon, and 6:00 PM) from both superstructures. To better quantify average strains and to be able to detect anomalous or spurious readings, the average of five readings were taken from every static system gage every six hours. Beginning at 2:00 PM on September 17, 2009 (after approximately one year of monitoring), the routine was changed such that five readings would be taken every hour instead of every six hours. This was done in order to better quantify daily thermal changes given that maximum temperature or thermal gradients would not necessarily occur at the six-hour interval times. From examining the thermistor data (refer to Chapter 5 for a more detailed discussion regarding thermal behavior), a sampling rate of at least 1 sample-per-hour should be used for accurate quantification of the maximum thermal gradients experienced by the structure.

The instrumentation locations of the static system led to only one heavily instrumented cross section (Location 7, midspan of the southbound structure). The initial and long-term behavior of concrete bridges is largely influenced by temperature, and the temperature dependence of the I-35W Bridge behavior can be seen in the data. With only one heavily instrumented section of temperature measurements, it is difficult to correlate the behavior of the entire southbound structure, let alone two separate structures, with the temperature gradients at one location. This may be a shortcoming in the current LP monitoring framework, which is entirely based on the temperatures at midspan of the southbound structure.

The data provided by the VWSGs and thermistors have been extremely useful for the long-term monitoring of the I-35W Saint Anthony Falls Bridge. The VWSG data has been used to validate design assumptions and finite element models (French et al. 2012, 2014); and after ten years of continued collection, there exists a uniquely large data set to better understand the time-dependent properties of

full-scale concrete structures (Chapter 6). The thermistors have been used to compare measured and design thermal gradients (Chapter 5), and are an essential component of the linear potentiometer monitoring system.

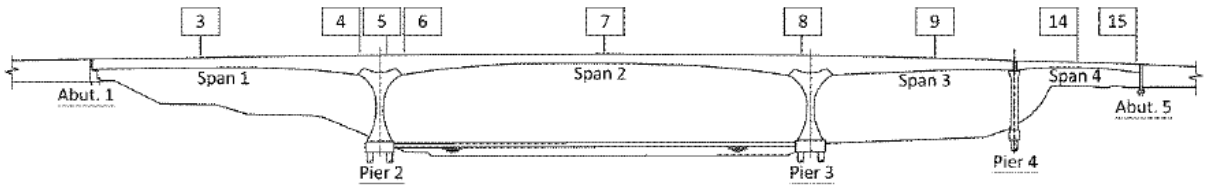

Figure 3.1: Elevation view of the adjacent bridges showing VWSG Locations 3, 4, 5, 6, 7, 8, 9, 14, and 15 (French et al. 2012).

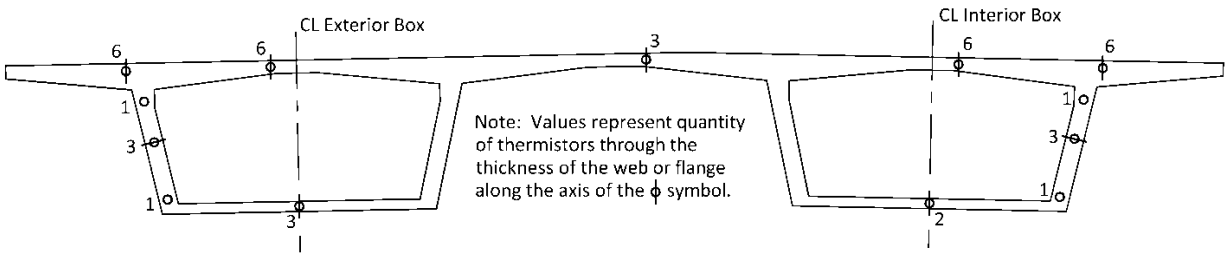

(a) Near midspan of Span 2 on the southbound bridge (Location 7SB) looking north.

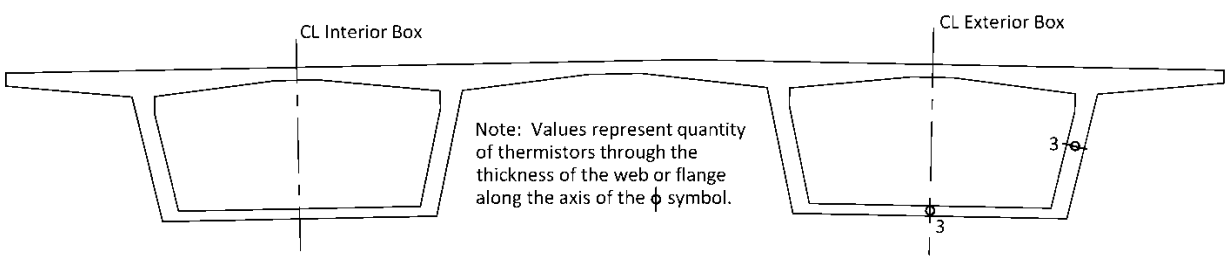

(b) Near midspan of Span 2 on the northbound bridge (Location 7NB) looking north.

Figure 3.2: Thermistor layout (French et al. 2012).

3.2 DYNAMIC SYSTEM

The dynamic system collected data from all accelerometers, linear potentiometers (LPs), and resistive strain gages installed on the bridge. Accelerometers measured the dynamic response of the structure at a given point. A total of 26 accelerometers were included in the superstructure of the bridge (20 in the southbound structure, 6 in the northbound structure). They were typically oriented in the vertical direction, but angle mountings allowed for a horizontal orientation at a limited number of locations. The long-term accelerometer layout is shown in Figure 3.3. The LPs measured the total longitudinal movement of the superstructure relative to the supports at Abutment 1 and Pier 4, as shown in Figure 3.4. Twelve linear potentiometers were installed at the bridge expansion joints (6 in the southbound structure, 6 in the northbound structure). Measurements collected by the dynamic system also included

the 24 resistive strain gages installed by the University of South Florida in the southbound bridge Pier 2 columns and drilled shafts.

The resistive strain gages were not well suited for long-term monitoring due to signal drift unrelated to structural deformation changes and were not expected to last far beyond initial monitoring of the construction process. Furthermore, the dynamic strains of the piers were not considered to be of particular value to overall monitoring of the structure. Therefore, the resistive strain gage data is no longer collected.

The initial deployment of the dynamic system had mixed success. Six of the twenty-four resistive strain gages were not originally collected in the dynamic system (75% connected) and it is unclear why these gages were not connected. The four LPs attached to the southbound bridge at Pier 4 were not collecting data at bridge opening because they were not powered properly (67% initial deployment success). The LP issue was resolved one year later, and all initial data at those sensor locations was lost. On the other hand, all 26 accelerometers were initially operational.

Many alterations have been made to the dynamic system collection protocol since its installation, mainly to address the vast amount of hard disk space that the data required on the server. Data collection for the dynamic system began on October 31, 2008 with an effective sampling rate of 200 Hz. Currently, the dynamic system collects acceleration measurements at 100 Hz and LP measurements at 4 Hz. All the dynamic data from the server must be moved periodically onto an external hard drive to free up hard disk space on the server. One year of dynamic data is approximately 250 GB.

The dynamic system has experienced many outages and typically requires personnel to visit the bridge to get the system running again. The timing for the dynamic system outages usually coincided with electrical storms in the area, and repairs for the system usually involved replacement of the data-logger boards or repeater nodes. In some instances, the system was brought back online by cycling power from an electrical box at ground level.

Because the dynamic data collection nodes are wired in series, if the connection in any one node fails, then all nodes down the chain will also fail. For example, if communication is lost to Node 4, Nodes 5 through 8 will also be down. This made troubleshooting difficult when there was a system failure and was a task that typically required at least two people: one inside the bridge and one on the server (accessed either remotely or at the server shed). Finding the location of the faulty node was most efficiently achieved using two spare functional boards.

Fourteen replacement linear potentiometers have been installed over the course of the monitoring period. Each time the sensors were replaced, a variety of errors may have been introduced into the readings. Examples of error include a small positional error by moving and reattaching the sensors and strings, different calibration between the old sensor and replacement sensor, and changing the recording channels thereby introducing differing resistance into the circuit. These errors make implementation of the long-term LP monitoring system difficult, as accounting for the possible shift in data due to sensor replacement is not straightforward. Some difficulties associated with implementing a long-term monitoring system on linear potentiometer data are given in Appendix B.

The data from some accelerometers was observed to contain erroneous readings. Some of the accelerometer data was observed to contain spurious jumps (offsets in baseline 'zero') in readings between daily collection data files. Also, bursts in the magnitude of some, but not all, accelerometer measurements over several minutes were observed. The bursts, as well as the abrupt offsets, were assumed to be due to power issues and were not representative of the bridge response. In addition, there is seasonal and daily variation of the baseline 1g offset of the DC accelerometers. This variation in the measured offset was attributed to temperature effects on the accelerometers themselves, and was deemed not useful for the task of estimating static displacements of the structure (Brown et al. 2019).

In an attempt to increase resolution of the accelerometer measurements, a 16-channel prototype filter board was installed on acquisition channels 17-32 of dynamic junction box "Node 6" on October 16, 2018. The prototype filter board is described in detail in Appendix A. At the time of this report, the acceleration data collected using the prototype filter board had not been analyzed.

Even though maintaining the dynamic system required much effort over the past 10 years, the supplier was very helpful in the event of system malfunctions. Josh Sebasky (Minnesota Measurement Engineering) routinely supplied assistance with troubleshooting hardware failures and Ken Spikowski (DATAQ Instruments, Inc.) provided software support. As Ken Spikowski nears retirement, it will become essential that a MnDOT representative become familiar with the DATAQ data collection system.

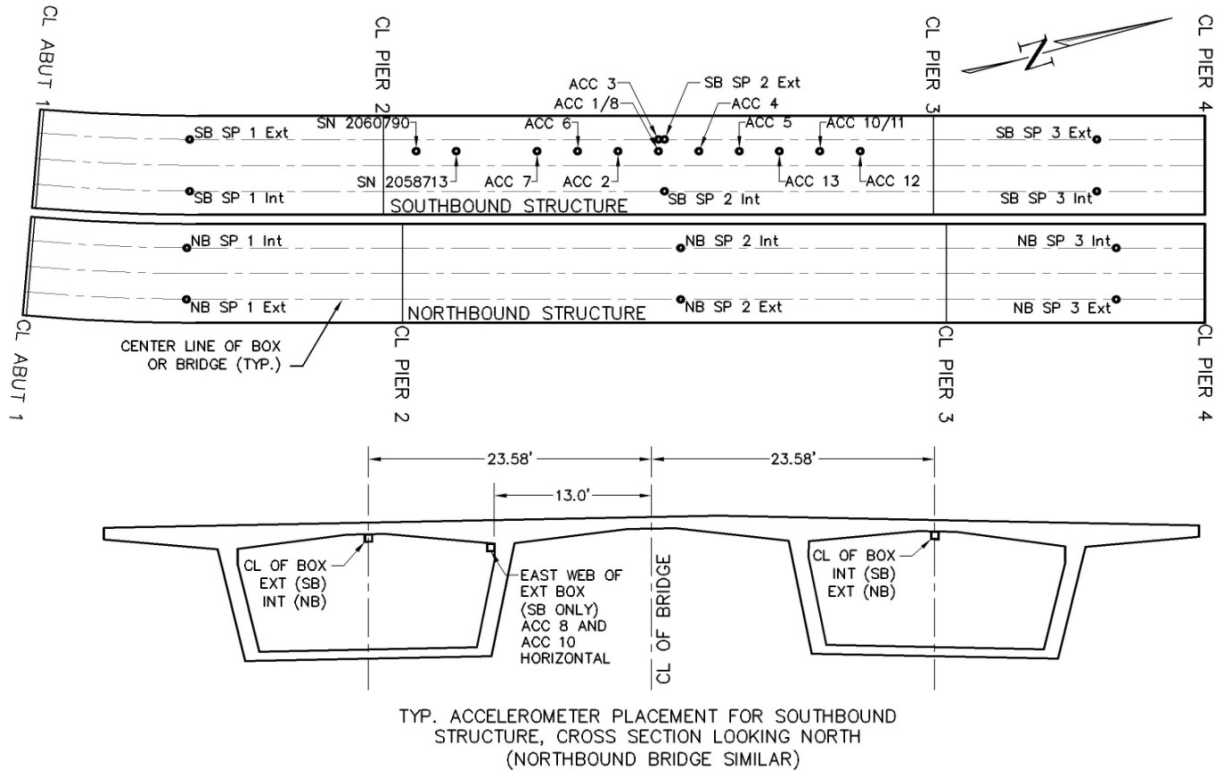

Figure 3.3: Long-term accelerometer layout used from May 11, 2010 until present (French et al. 2012)

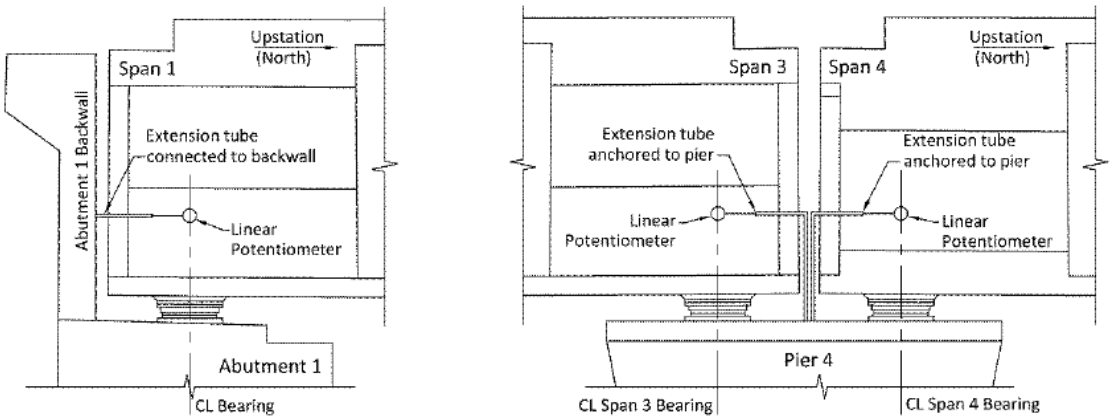

Figure 3.4: Typical linear potentiometer installations at Abutment 1 and Pier 4 (French et al. 2012).

3.3 FIBER OPTIC STRAIN GAGES (SOFO)

The SOFO (Surveillance d'Ouvrages par Fibres Optiques) system contains fiber optic strain gages installed in the exterior box of the southbound bridge. These gages are externally mounted, with six attached to the top flange and six to the bottom flange, all within the exterior box of Span 2. The locations of the SOFO gages and the typical sensor layout are shown in Figure 3.5 and 3.6, respectively.

SOFO fiber optic gages collect averaged strain measurements over the sensor gage length of 13.1 ft (4.0 m). These sensors, much like the VWSGs from the static system, are intended to measure static behavior due to thermal behavior or truck tests and are not meant for transient loading. Compared to the gage length of the Roctest EM-5 VWSGs equal to 6.75 in (0.17 m), the SOFO sensors provided average strain over relatively long gage lengths. Each SOFO gage has two parallel optic fibers, one that is used to measure strains of the structure and one that is used as a reference to enable compensation for temperature changes. A comparison between the strain measurements taken from the fiber optic strain gages and vibrating wire strain gages is given in Chapter 4.

Currently, the SOFO system records static strains, however it can be used to measure dynamic strains as long as the proper datalogger is used. The supplier of the SOFO system (Smartec) committed to providing a dynamic data acquisition system a total of four times over the course of the monitoring project. Thus far, the system has been used twice: the first time during July of 2010 and the second time during the truck tests performed in October of 2010.

Previously, an issue with the dynamic collection unit was that only eight channels could be simultaneously attached to the acquisition system, meaning that four of the sensors were excluded from measurements. For future uses of the dynamic SOFO system, French et al. has detailed which sensors should be used if only a subset can be recorded. In addition, the acquisition system required approximately an hour of "warm-up time." If data was collected before the system had warmed-up, then a strong linear drift unrelated to deformations of the bridge would be seen. The dynamic SOFO

acquisition system always began collection of the strain readings for each data block at zero (regardless of the absolute level of sensor deformation) and thus was only used to measure the changes in strain over the measurement block.

For nearly the first year and a half of the SOFO system being installed on the bridge, the data collection was often erratic and the system would randomly miss data readings. Occasionally, these skips would be chronic and one sensor would appear to be down for several days at a time. The problems were not necessarily unique to any particular sensor. When the system did manage to read the sensors, the strain values appeared to be reasonable. The system supplier (Smartec) resolved the issue with an update to the data collection software and data-logger firmware on January 9, 2010.

The SOFO system has experienced many data outages, several of which have unknown/undocumented causes. A reoccurring cause for the data loss is the database file size becoming too large so no more data can be added to the file. An automatic file backup was set up to run on the first of every month to address this issue, but on rare occasions it does not perform as planned.

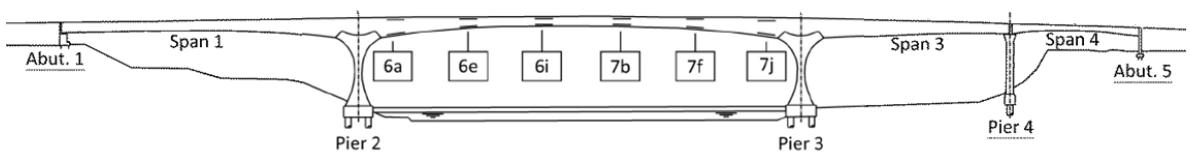

Figure 3.5: Elevation view of the adjacent bridges showing SOFO sensor locations (French et al. 2012).

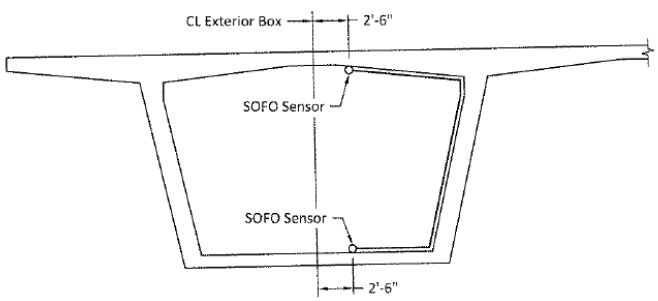

Figure 3.6: Typical SOFO sensor layout (French et al. 2012).

3.4 CORROSION MONITORING SYSTEM (CORSENSYS)

The corrosion monitoring system (CorSenSys) was installed to monitor the corrosive environment of the bridge deck. Two types of sensors were installed, each of which consisted of a series of four short pieces of reinforcement that were connected to a bar in parallel layers. The sensors worked by measuring the resistivity between the short pieces of reinforcement, which would change with the reinforcement corrosion level, concrete moisture, pore volume, and temperature.

A total of four of each sensor were installed in the bridge (8 total corrosion potential sensors), located in the deck above the exterior box of each structure near the midspan of Span 1 and Span 3. Four dataloggers were used to read the data hourly.

The CorSenSys has never been fully operational since the system was installed. No user's manual was provided by the suppliers, and the collected data has never been fully analyzed or understood. The company was contacted about this issue, but no useful information was provided. Prior to April 14, 2011, none of the dataloggers provided data usable for any sort of monitoring. On April 14, 2011, two of the dataloggers were replaced, followed by the remaining two dataloggers being replaced on September 13, 2011. The new dataloggers appear to provide data that might be usable for monitoring, but without a user's manual interpretation of the data has proven impossible.

The CorSenSys system is no longer operational. Data has not been collected since May 27, 2012.

3.5 SUMMARY OF INSTRUMENTATION PERFORMANCE

Overall, the instrumentation survival rate of approximately 90 percent over the ten years is significant given the deployment duration, embedment of gages, and variety of sensor types. The static, dynamic, and SOFO systems have helped validate design assumptions and provide insight on the temperature- and time-dependent behavior of the bridge. Specifically, the static, dynamic, and SOFO instrumentation systems have helped calibrate the FEM model used for behavior comparisons and to validate assumptions. For long-term monitoring, the temperatures measured on the static system and LP displacements on the dynamic system have provided the most valuable information regarding time-dependent effects and expected behavior.

In future monitoring systems, having researchers on-site during sensor installation will limit possible errors due location uncertainty and labeling. Additionally, researchers should work with contractors and be present to take initial measurements once the concrete has hardened. Additional care in the system design for electrical grounding and ease of power cycling will limit outages and associated downtime due to electrical storms.

CHAPTER 4: COMPARISON OF STATIC STRAIN DATA

Strain measurements from the vibrating wire strain gages (VWSG) and fiber optic strain gages (SOFO) have been collected on the I-35W Saint Anthony Falls Bridge during the first ten years of service. Vibrating wire strain gages are located in both the southbound and northbound superstructures, as well as Pier 2 of the southbound structure. SOFO fiber optic strain gages are located in the exterior box of the southbound structure. French et al. (2012) has a complete list of the bridge instrumentation.

This chapter compares the vibrating wire strain gage and SOFO fiber optic strain gage data over the ten-year period 9/1/2008 – 10/6/2018, with focus placed on each gage type's sensitivity to temperature changes and time-dependent strains. Only superstructure strains were considered. Positive strains are defined to be tensile, and negative strains are compressive.

4.1 VIBRATING WIRE STRAIN GAGE DATA FROM SUPERSTRUCTURE

Mechanical plus creep and shrinkage strains were computed for the vibrating wire strain gage data in the northbound and southbound bridges using Eqn. (1).

$$\Delta\varepsilon_{mechanical} + \Delta\varepsilon_{creep} + \Delta\varepsilon_{shrinkage} = \Delta\varepsilon_{measured} + \left(\alpha_{gauge} - \alpha_{concrete}\right)\Delta T \qquad (4\text{-}1)$$

The change in strains are $\Delta\varepsilon$, ΔT is the change in temperature measured at the location of the strain gage, and α is the coefficient of thermal expansion (CTE). The CTE of the gage per the Roctest Instrumentation Manual (2006) is α_{gage} = 6.39 $\mu\varepsilon$/°F (11.5 $\mu\varepsilon$/°C) and the experimentally determined CTE of the superstructure concrete is $\alpha_{concrete}$ = 5.60 $\mu\varepsilon$/°F (10.1 $\mu\varepsilon$/°C) (Hedegaard et al. 2013). Reference values from September 21, 2008 11:00 CST were used for computing the change in strains and temperatures. Similar to Figures 7.21 through 7.38 in French et al. (2012), top and bottom flange gages were chosen for investigation of the long-term longitudinal behavior of the structure, as well as additional gages at Location 7 of the southbound structure. Figures 4.1 through 4.8 depict the mechanical, creep, and shrinkage strains (left side of Eq. 4-1) for southbound Locations 3, 4, 5, 7, 8, 9, 14 and 15 (as shown in Figure 3.1). Figures 4.9 through 4.15 depict the mechanical, creep, and shrinkage strains for northbound locations 3, 5, 7, 8, 9, 14, and 15. Plotted temperatures, assumed to be representative of the average temperature for the structure, were taken from thermistor TSEWB002 for plots of gages from the southbound bridge and thermistor TNEEA002 for plots of gages from the northbound bridge. Thermistors TSEWB002 and TNEEA002 were located at approximately mid-depth on the centerline of the exterior box's exterior web at Location 7 of the southbound and northbound structures, respectively.

The plotted strains reflect the daily mechanical strain variation, seasonal variation, as well as time-dependent effects. At Location 7 of both structures (Figures 4.4 and 4.11), the daily strain variations were often on the order of 100 $\mu\varepsilon$. The daily changes correspond to mechanical strain as the changes in creep and shrinkage are negligible in that timeframe. Seasonal variations due to temperature, which are reflected in the consistent relative annual strain variation, were just as significant. Top flange daily

mechanical strain variations were typically larger than the bottom flange daily mechanical strain variations. Long-term creep and shrinkage strains were approximated by fitting a log power equation to data points from October 1 at 5:00 CST of every year with available data. The log power equation was shown to be one of several models that best match the long-term behavior of the bridge (French et al. 2012). Using the fit, bottom flange creep and shrinkage strains at Location 7 were estimated to be around 300 με over the course of the first ten years of monitoring, and top flange creep and shrinkage strains were noted to be considerably less (around 200 με), indicating that the structure continued to camber upwards after erection. For most other locations, bottom flange mechanical strain seasonal and daily variations were much lower than those measured at Location 7, which is located at midspan of the river span. Figure 4.16 shows the long-term mechanical plus creep and shrinkage strains for the vertical gages located in the east (interior) web of the exterior box of the southbound bridge. Daily mechanical strains due to thermal effects were on the order of approximately 20 με measured by the web gages, with seasonal mechanical strains typically less than 50 με. Time-dependent strains from the vertically oriented gages over the first ten years were minimal, approximately 70 με, which is assumed to be primarily attributed to shrinkage.

Figures 4.17 and 4.18 show the long-term mechanical plus creep and shrinkage strains for the transverse gages located in the top flange and bottom flange, respectively, of the southbound bridge. In the top flange, daily mechanical strains due to thermal effects were typically on the order of 50 με, which was expected due to the rapidly varying temperature with depth observed in the top flange. In the bottom flange, daily thermal variations were on the order of 10 to 20 με. Seasonal thermal variations were approximately 30 με in both the top and bottom flanges. Similar to the vertical gages, time-dependent strains in the transverse gages in both the top and bottom flanges were small, typically less than 70 με over the first ten years of monitoring. Time-dependent strains in the transverse gages are larger in the top flange than the bottom flange, likely due to the presence of transverse post-tensioning in the top flange.

Strain data from sensor VN15ITL1 (Figure 4.15, longitudinal gage in top flange at northbound Location 15) appears to contain erroneous readings from October 2012 to present. Strain readings from sensors VN09ITL1, VS15IBL1, VS07EBL1, and VS03EBT2 also appear to contain previously undocumented erroneous strain readings. None of the superstructure vibrating wire strain gages, including those not plotted in Figures 4.1 through 4.18, showed any clear indications of cracking or other damage.

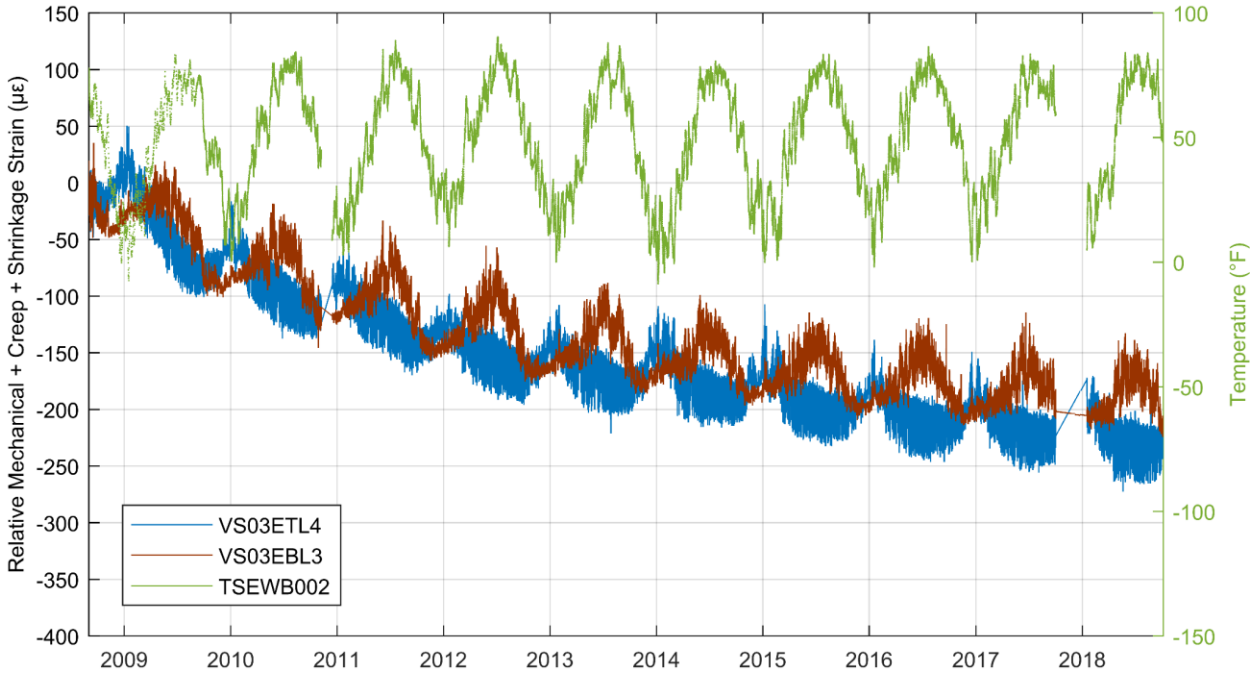

Figure 4.1: Relative mechanical strain plus creep and shrinkage strains for gages VS03ETL4 (blue; longitudinal gage in top flange at southbound Location 3) and VS03EBL3 (red; longitudinal gage in bottom flange at southbound Location 3).

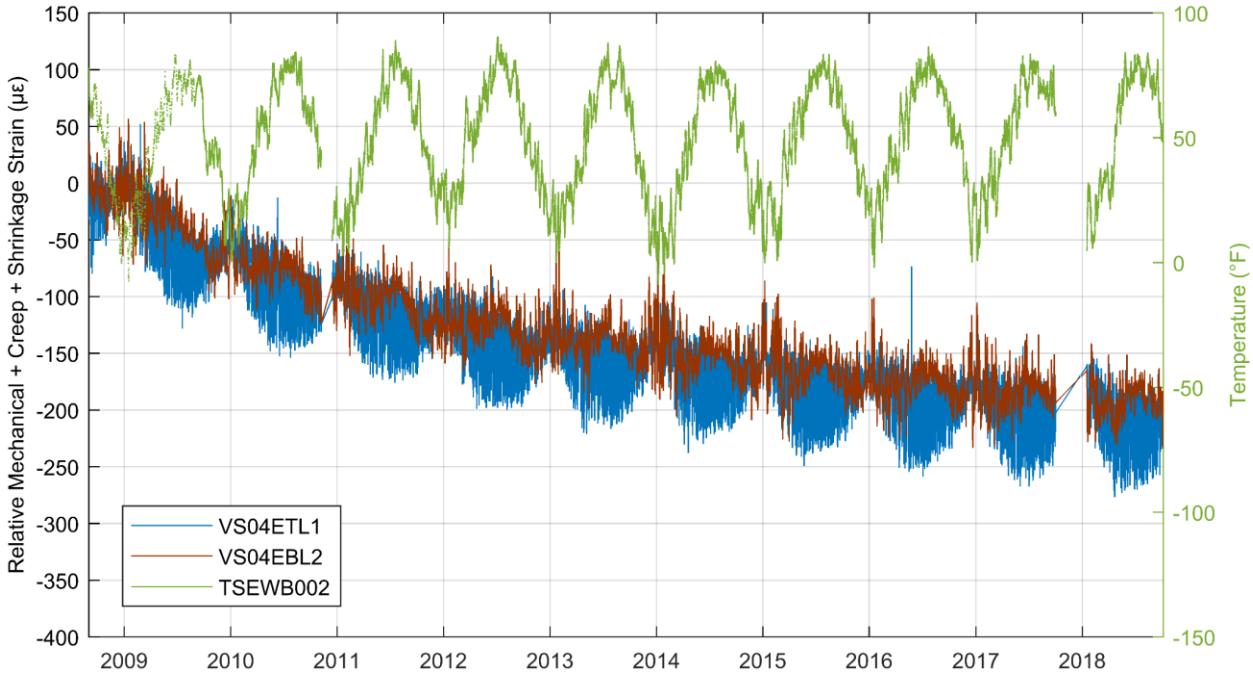

Figure 4.2: Relative mechanical strain plus creep and shrinkage strains for gages VS04ETL1 (blue; longitudinal gage in top flange at southbound Location 4) and VS04EBL2 (red; longitudinal gage in bottom flange at southbound Location 4).

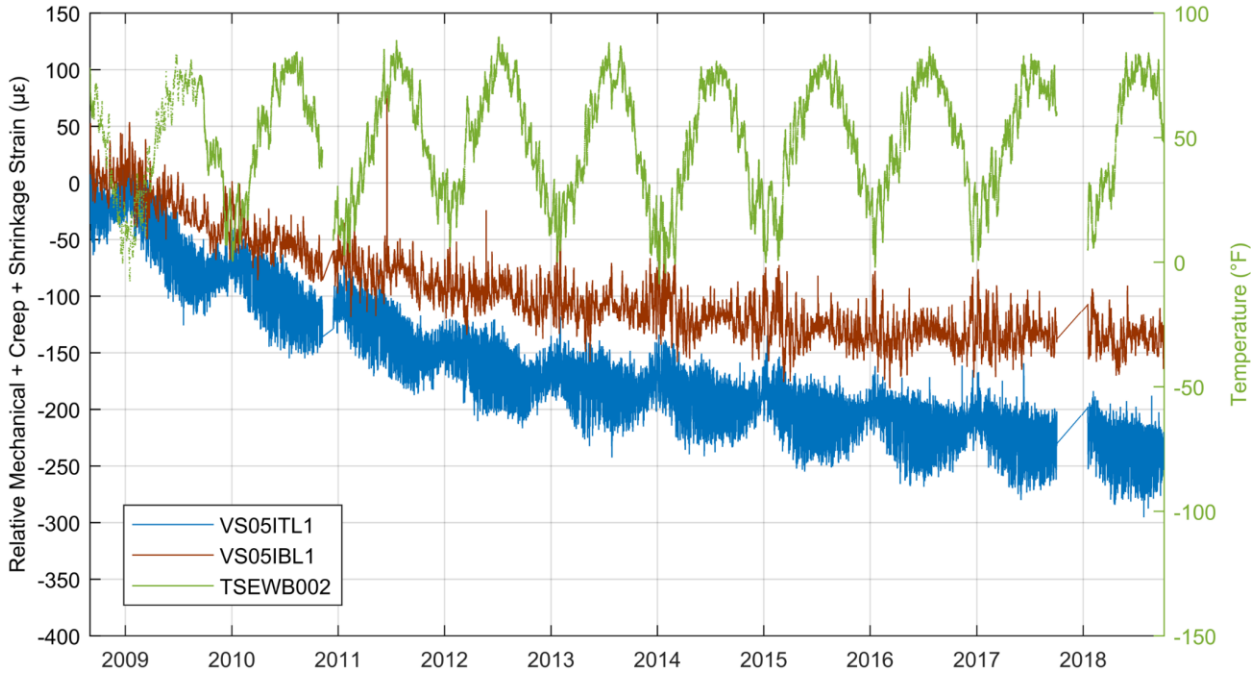

Figure 4.3: Relative mechanical strain plus creep and shrinkage strains for gages VS05ITL1 (blue; longitudinal gage in top flange at southbound Location 5) and VS05IBL1 (red; longitudinal gage in bottom flange at southbound Location 5).

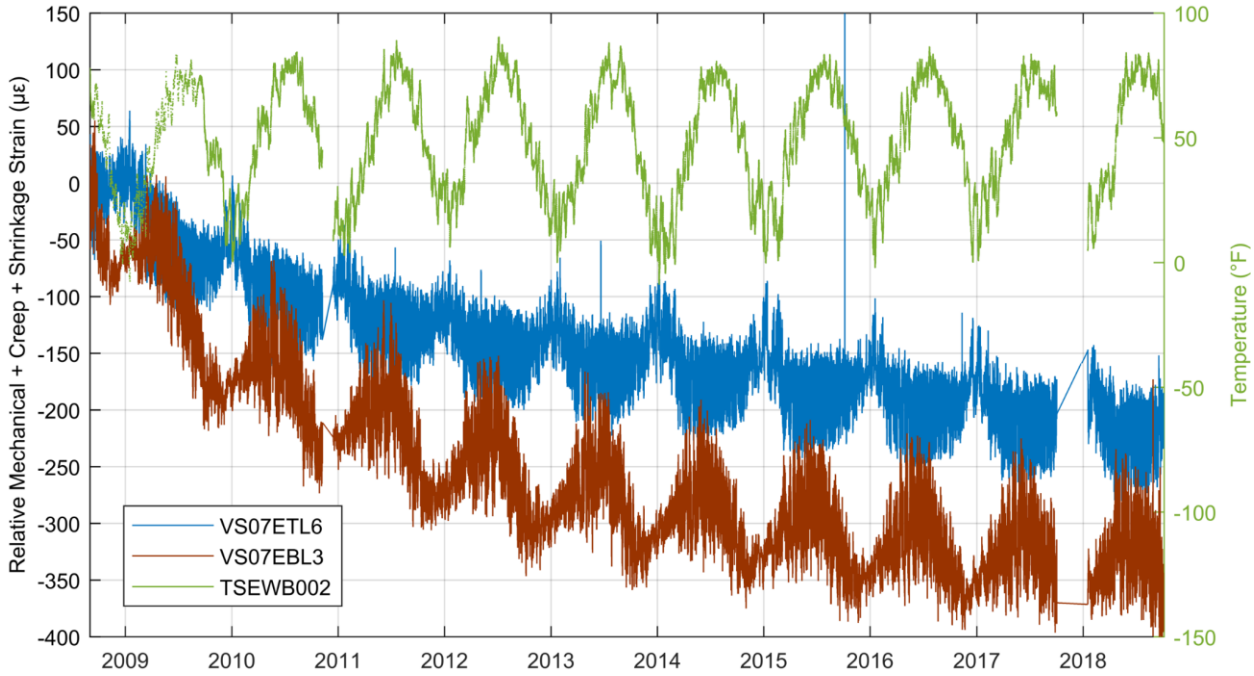

Figure 4.4: Relative mechanical strain plus creep and shrinkage strains for gages VS07ETL6 (blue; longitudinal gage in top flange at southbound Location 7) and VS07EBL3 (red; longitudinal gage in bottom flange at southbound Location 7).

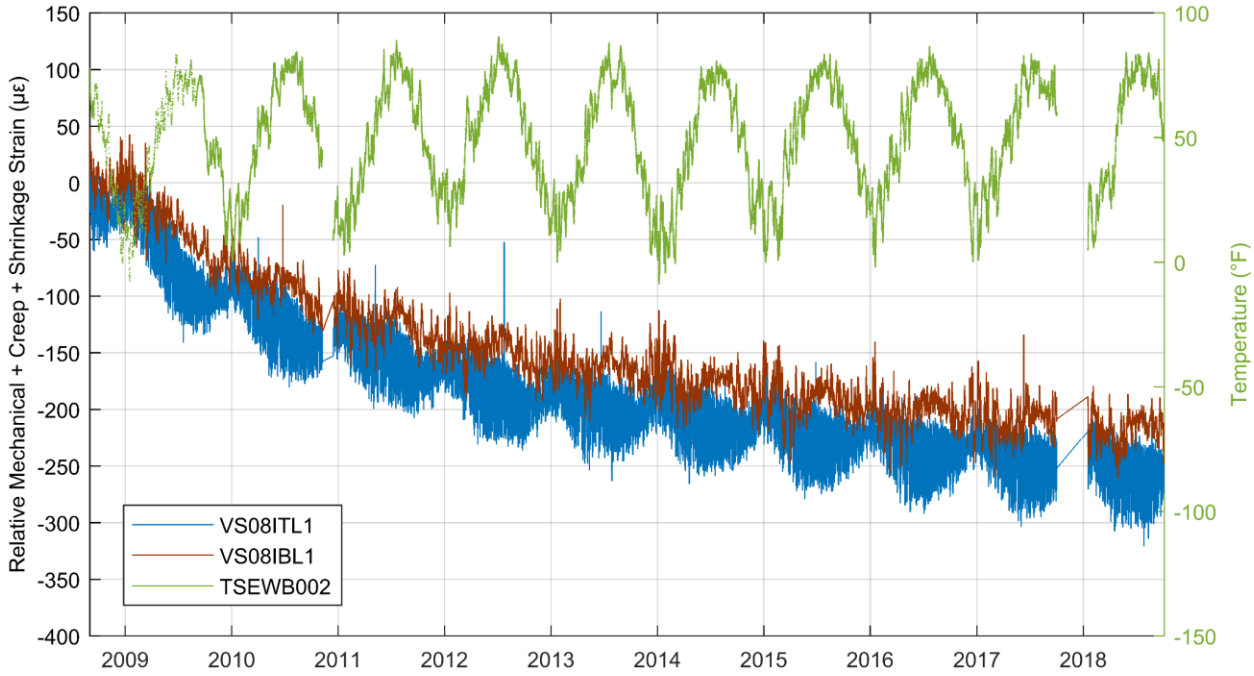

Figure 4.5: Relative mechanical strain plus creep and shrinkage strains for gages VS08ITL1 (blue; longitudinal gage in top flange at southbound Location 8) and VS08IBL1 (red; longitudinal gage in bottom flange at southbound Location 8).

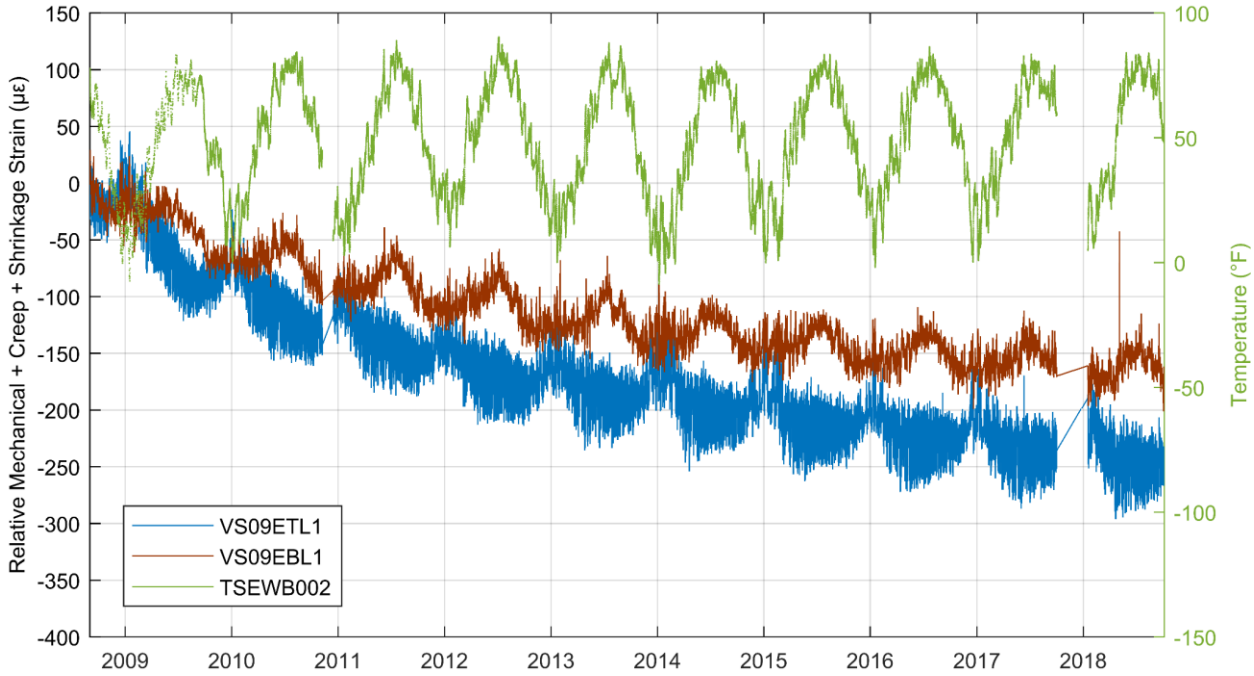

Figure 4.6: Relative mechanical strain plus creep and shrinkage strains for gages VS09ETL1 (blue; longitudinal gage in top flange at southbound Location 9) and VS09EBL1 (red; longitudinal gage in bottom flange at southbound Location 9).

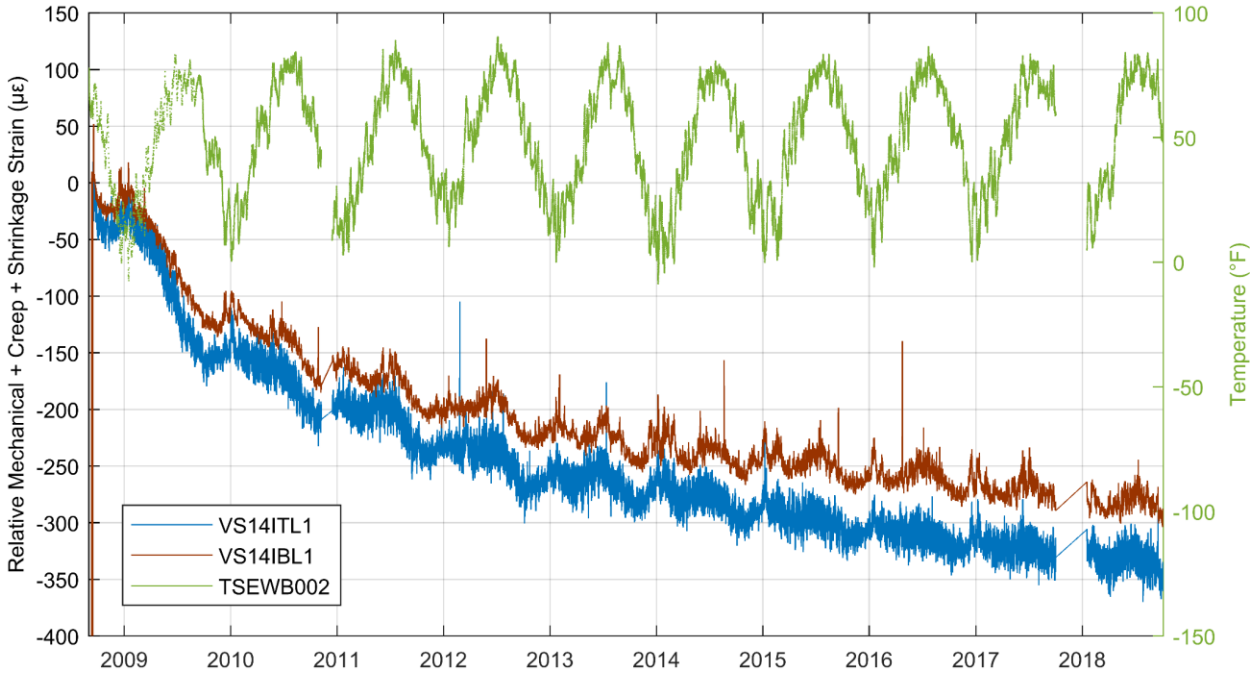

Figure 4.7: Relative mechanical strain plus creep and shrinkage strains for gages VS14ITL1 (blue; longitudinal gage in top flange at southbound Location 14) and VS14IBL1 (red; longitudinal gage in bottom flange at southbound Location 14).

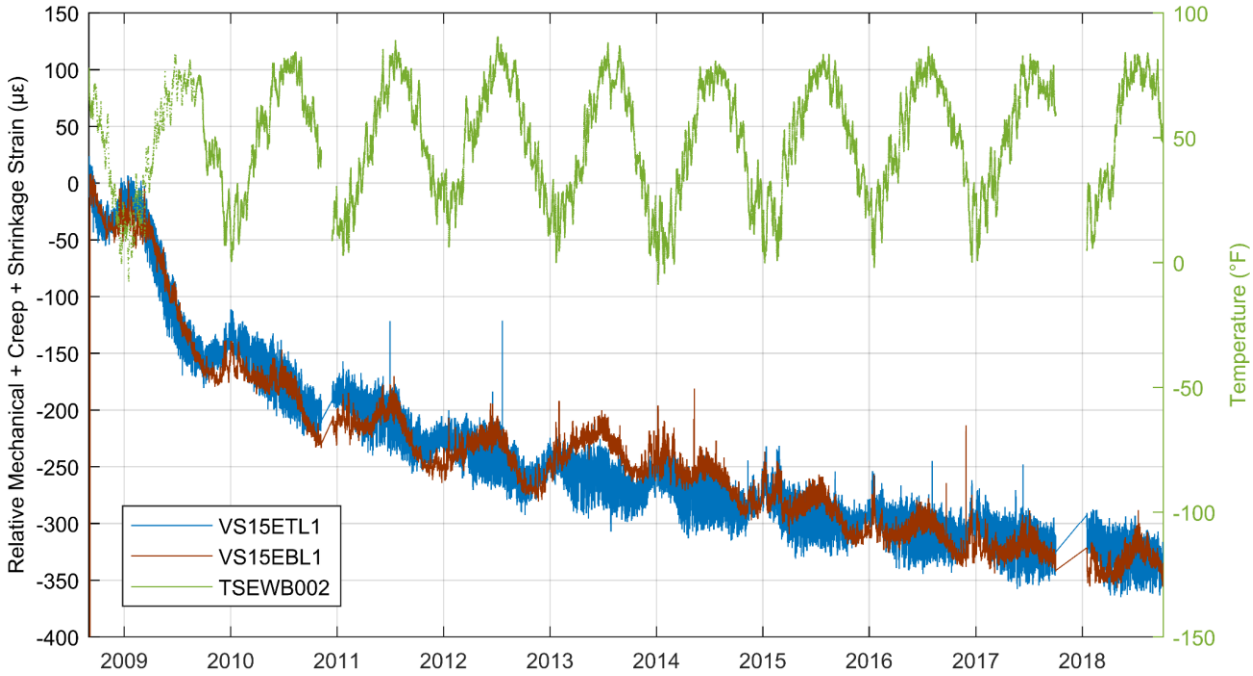

Figure 4.8: Relative mechanical strain plus creep and shrinkage strains for gages VS15ETL1 (blue; longitudinal gage in top flange at southbound Location 15) and VS15EBL1 (red; longitudinal gage in bottom flange at southbound Location 15).

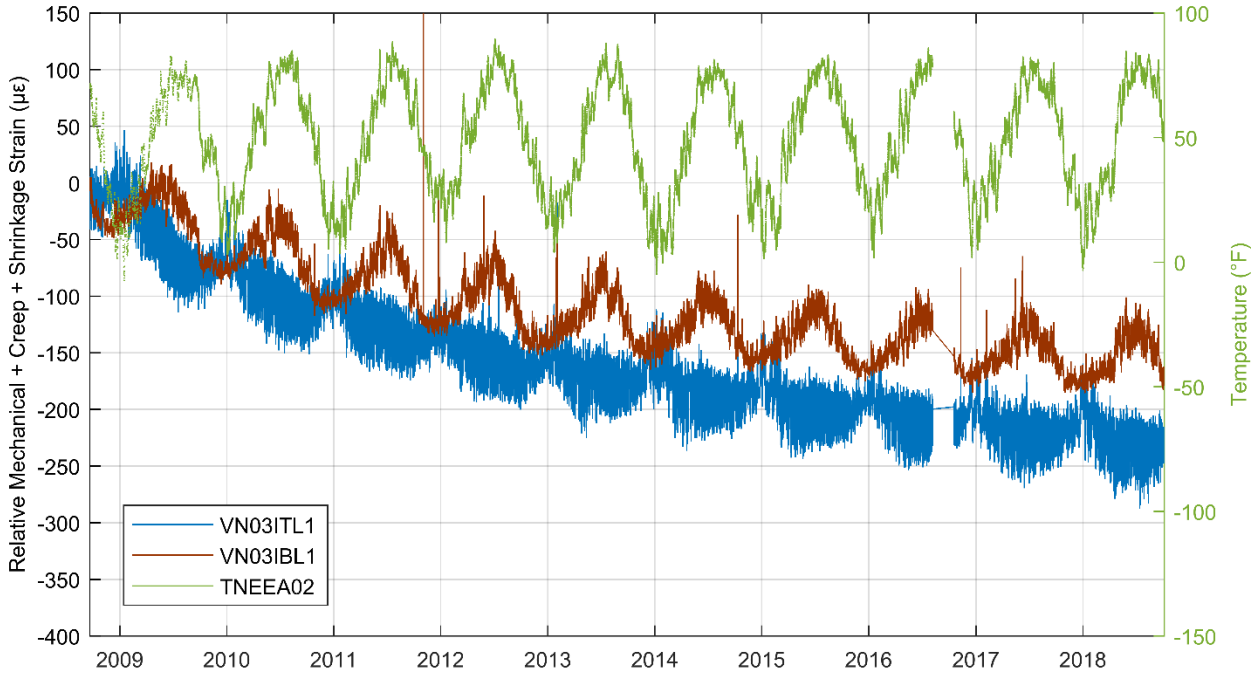

Figure 4.9: Relative mechanical strain plus creep and shrinkage strains for gages VN03ITL1 (blue; longitudinal gage in top flange at northbound Location 3) and VN03IBL1 (red; longitudinal gage in bottom flange at northbound Location 3).

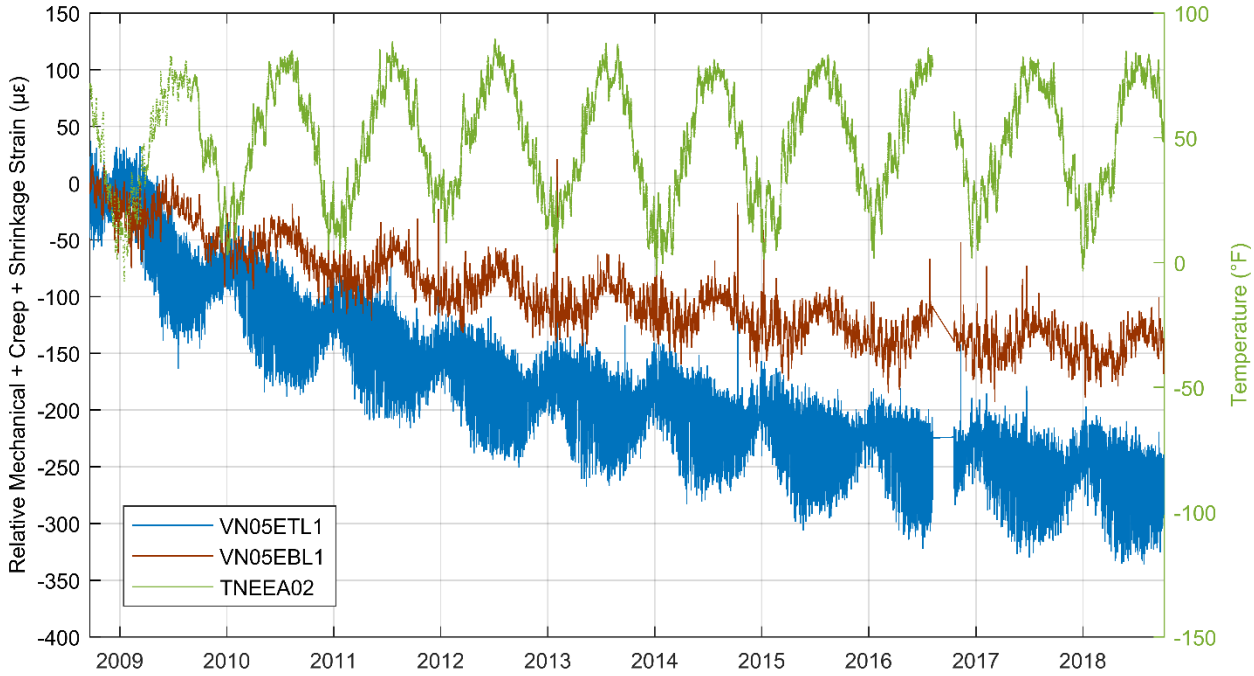

Figure 4.10: Relative mechanical strain plus creep and shrinkage strains for gages VN05ETL1 (blue; longitudinal gage in top flange at northbound Location 5) and VN05EBL1 (red; longitudinal gage in bottom flange at northbound Location 5).

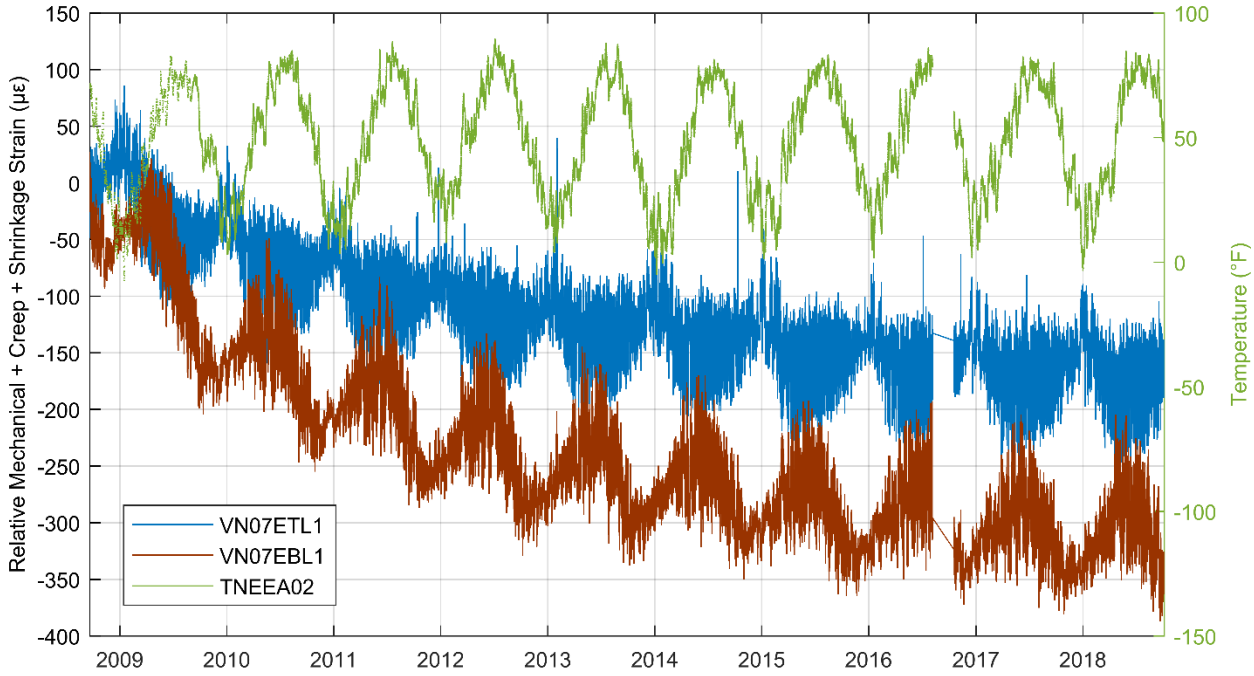

Figure 4.11: Relative mechanical strain plus creep and shrinkage strains for gages VN07ETL1 (blue; longitudinal gage in top flange at northbound Location 7) and VN07EBL1 (red; longitudinal gage in bottom flange at northbound Location 7).

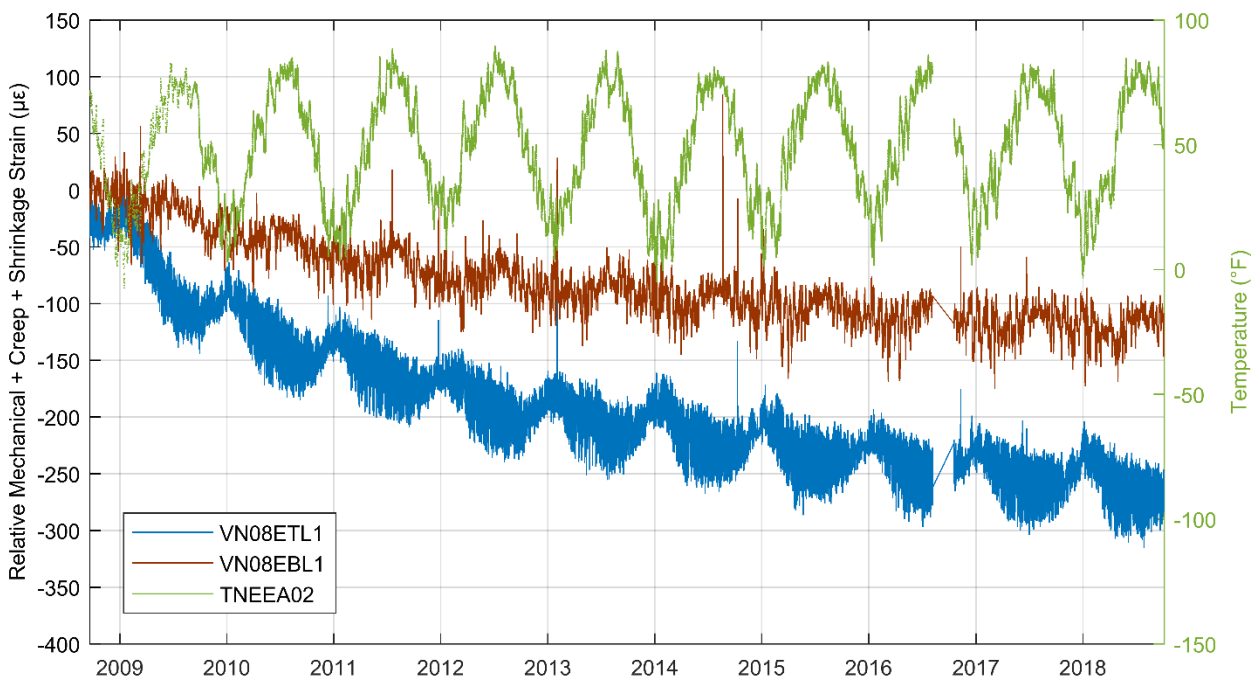

Figure 4.12: Relative mechanical strain plus creep and shrinkage strains for gages VN08ETL1 (blue; longitudinal gage in top flange at northbound Location 8) and VN08EBL1 (red; longitudinal gage in bottom flange at northbound Location 8).

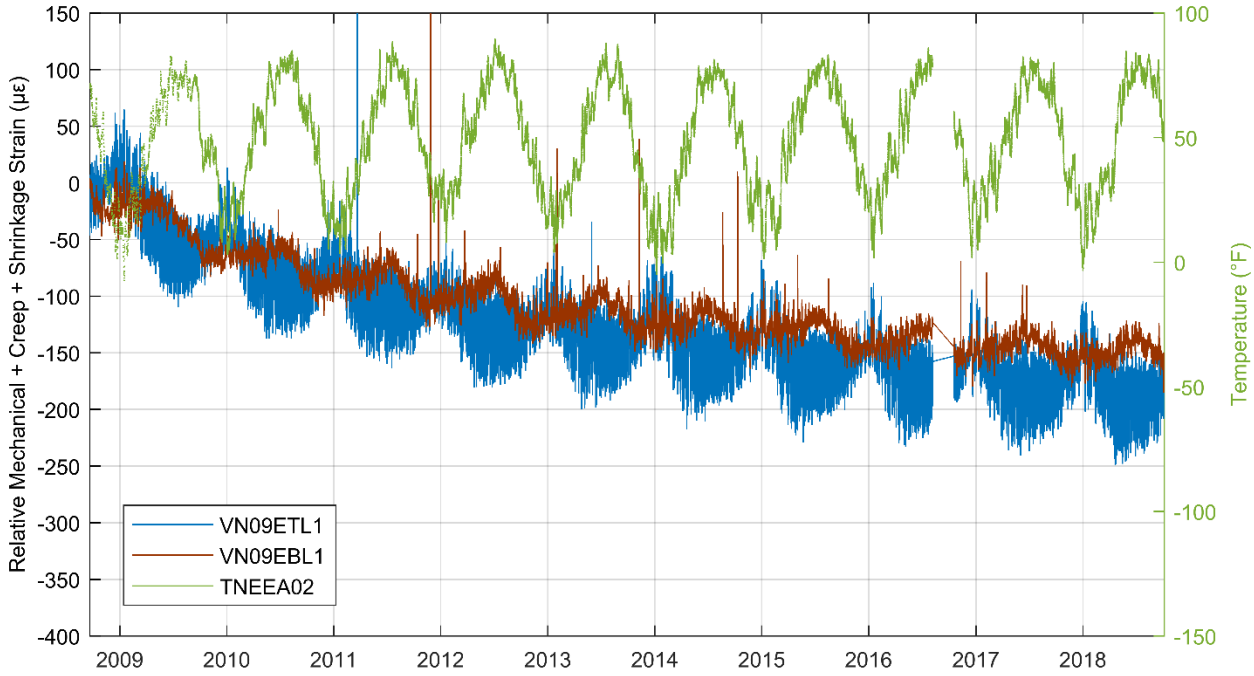

Figure 4.13: Relative mechanical strain plus creep and shrinkage strains for gages VN09ETL1 (blue; longitudinal gage in top flange at northbound Location 9) and VN09EBL1 (red; longitudinal gage in bottom flange at northbound Location 9).

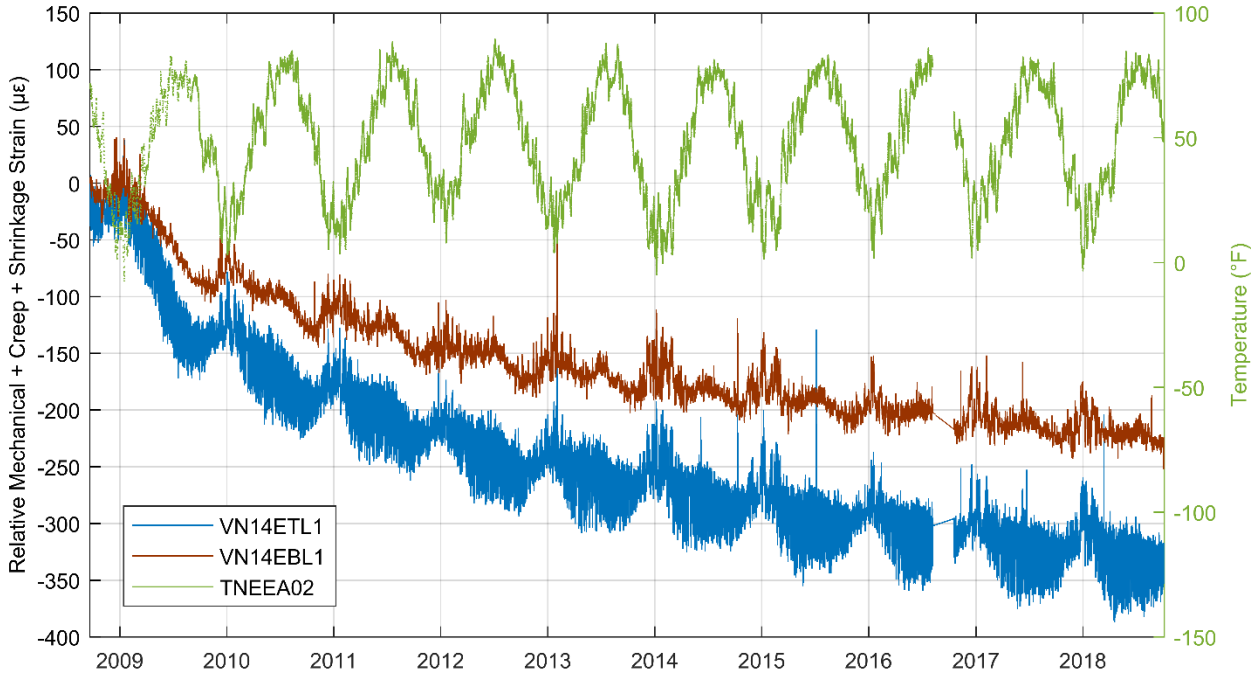

Figure 4.14: Relative mechanical strain plus creep and shrinkage strains for gages VN14ETL1 (blue; longitudinal gage in top flange at northbound Location 14) and VN14EBL1 (red; longitudinal gage in bottom flange at northbound Location 14).

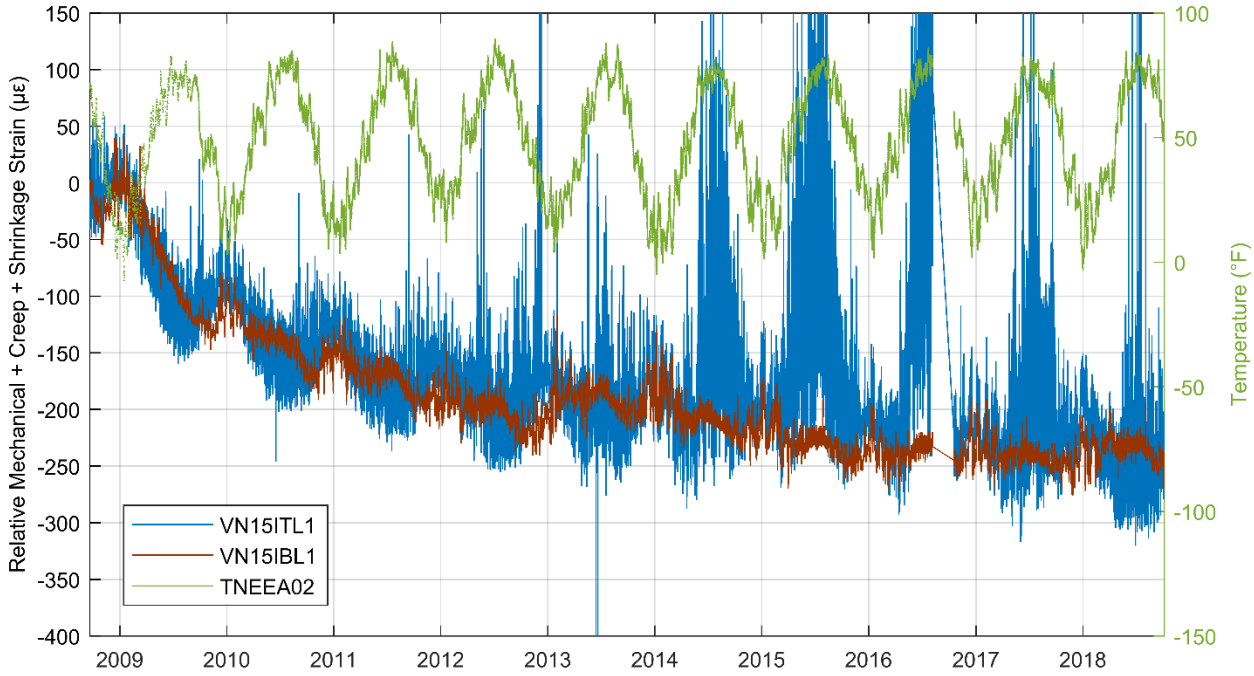

Figure 4.15: Relative mechanical strain plus creep and shrinkage strains for gages VN15ITL1 (blue; longitudinal gage in top flange at northbound Location 15) and VN15IBL1 (red; longitudinal gage in bottom flange at northbound Location 15).

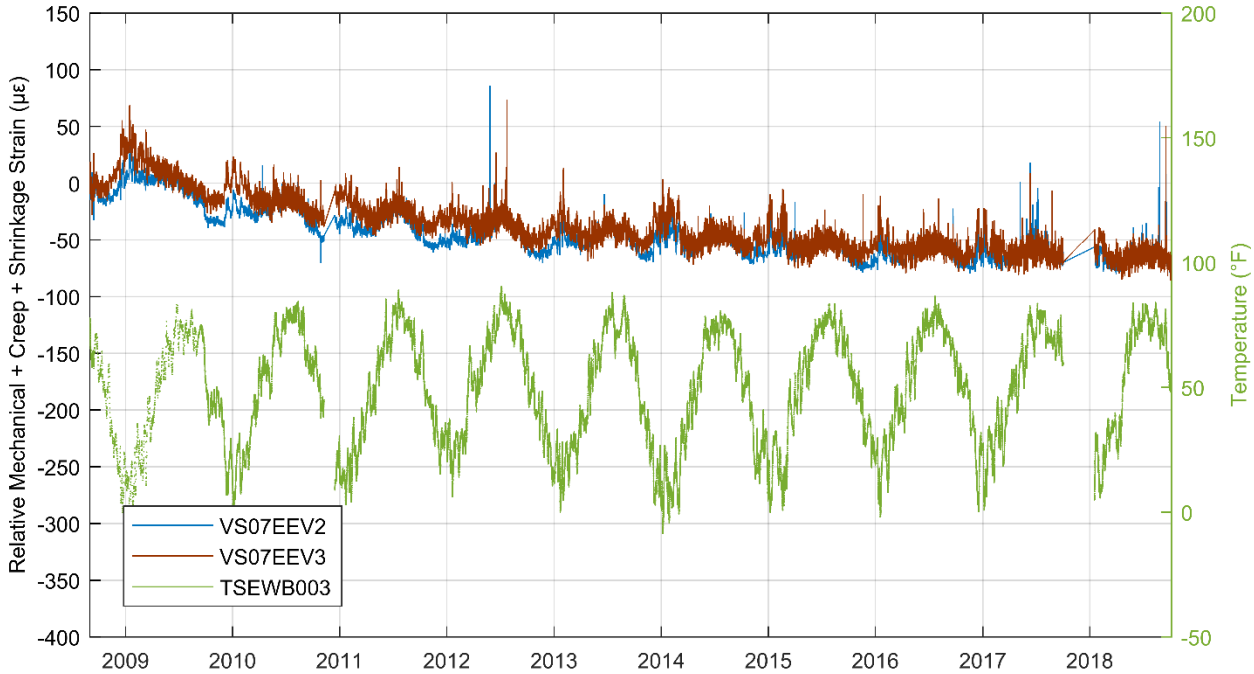

Figure 4.16: Relative mechanical strain plus creep and shrinkage strains for gages VS07EEV2 (blue; vertical gage at interior face of east web of exterior box, southbound Location 7) and VS07EEV3 (red; vertical gage at exterior face of east web of exterior box, southbound Location 7).

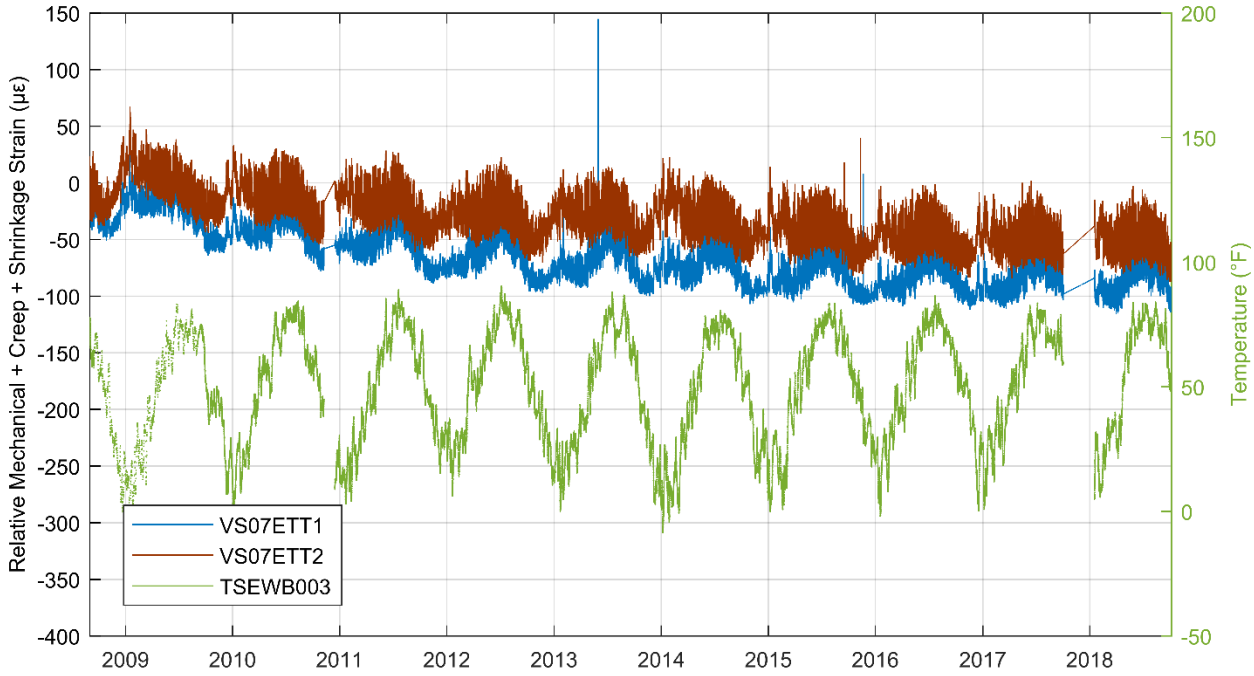

Figure 4.17: Relative mechanical strain plus creep and shrinkage strains for gages VS07ETT1 (blue; top transverse gage in top flange at southbound Location 7) and VS07ETT2 (red; bottom transverse gage in top flange at southbound Location 7).

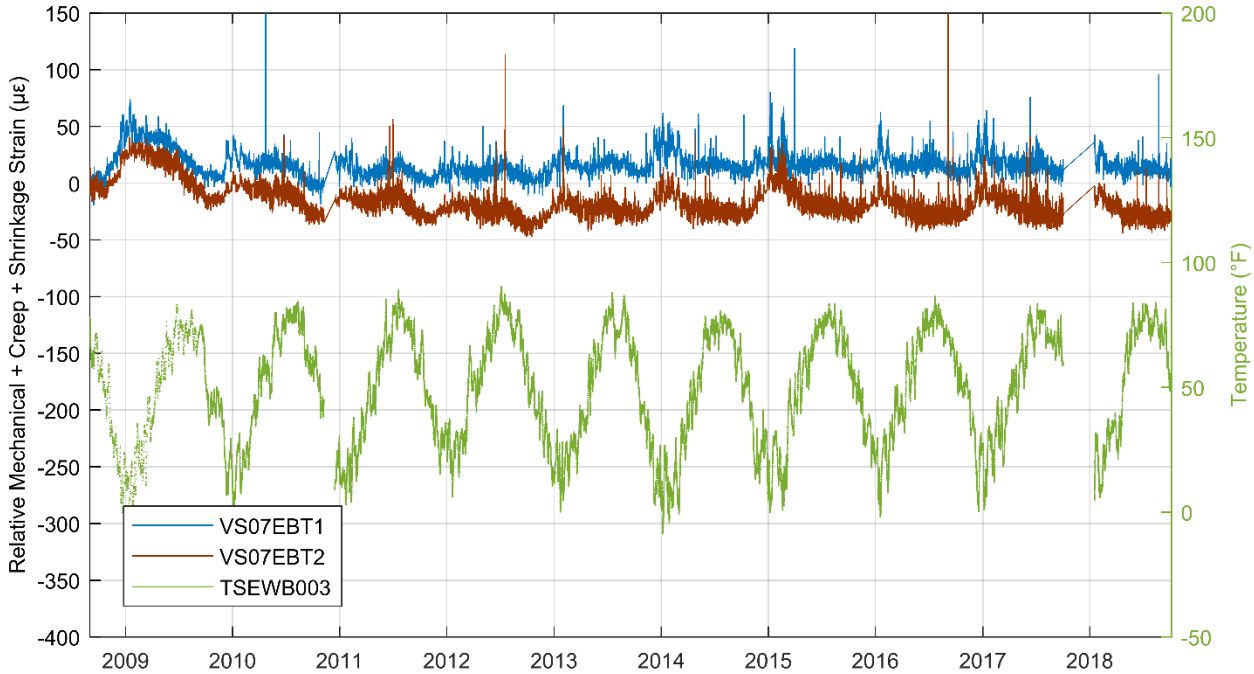

Figure 4.18: Relative mechanical strain plus creep and shrinkage strains for gages VS07EBT1 (blue; top transverse gage in bottom flange at southbound Location 7) and VS07EBT2 (red; bottom transverse gage in bottom flange at southbound Location 7).

4.2 FIBER OPTIC STRAIN GAGE (SOFO) DATA

SOFO data was used to determine mechanical plus creep and shrinkage strains for the southbound bridge, as defined in Eqn. (4-1). The effect of temperature change on the SOFO gages is accounted for by the use of a reference fiber optic strain gage within the box that is not rigidly attached to the structure. Using data from the reference strain gage, the SOFO system removes the effects of temperature on the gage from the measurement before recording it. Therefore, unlike the vibrating wire gages, thermal strains of the gage are already compensated for in the SOFO gage measurements. Reference values at September 19, 2008 10:04 CST were used for computing change in strains and temperatures. Figures 4.19 through 4.24 depict the total strains (mechanical + creep + shrinkage + thermal) at the top and bottom flanges for southbound Locations 6a, 6e, 6i, 7b, 7f, and 7j (as shown in Figure 3.5).

In order to correct the measured total strains for concrete thermal expansion, a representative concrete temperature must be assumed for each SOFO gage. Temperature gradients can be large through the thickness of the concrete section, and selection of a representative temperature gage is difficult. Temperatures taken from surface mounted gages were deemed unrepresentative of the internal concrete temperature. Because thermistors are not embedded at the SOFO locations, thermistors embedded just below the internal surface at a location with a similar cross section to the locations of the SOFO gages were believed to provide the most appropriate compensation of concrete thermal expansion for the SOFO strain measurements. Thermistors in the exterior box at Location 7 of the southbound structure were used for calculation of SOFO mechanical strains: thermistor TSETB006 (nearest gage to interior surface in top flange) for top flange SOFO gages and thermistor TSEBA002 (nearest working gage to interior surface in bottom flange) for bottom flange SOFO gages.

The thermistor and SOFO gage data are collected by two different data acquisition systems. This adds to the complexity of merging data, because the systems may go down at different times. Mechanical strains cannot be computed unless data is available from both the static and SOFO systems. For plots of mechanical plus creep and shrinkage strains, missing segments of long duration are due to static system outages.

Compared to the vibrating wire strain gage mechanical strains, the SOFO mechanical strains likely contain higher error. This is due to the uncertainty imposed by the concrete thermal expansion correction using temperature gages that may not accurately reflect the concrete temperature at the location of the SOFO gage. More error is expected at locations with significantly more thermal mass than at midspan, such as those closer to the piers (Locations 6a and 7j). The magnitude of this error is likely on the order of the daily mechanical strain variation, or around 20 to 50 $\mu\varepsilon$ (approximate temperature error of 2 to 5 °C). To overcome this problem in the future, it is recommended that, at minimum, a temperature gage be installed directly below the concrete surface at the center of each SOFO gage. Depending on the longitudinal temperature variation in the cross section over the length of the SOFO gage, more embedded temperature gages may be necessary to accurately capture the internal concrete temperature.

Long-term creep and shrinkage strains in both the top and bottom gages were similar to those seen from the longitudinal vibrating wire strain gages over Span 2 of the southbound structure, around 220 to 310 με. The time-dependent strains at Locations 6i, 7, and 7b suggest continued cambering after erection.

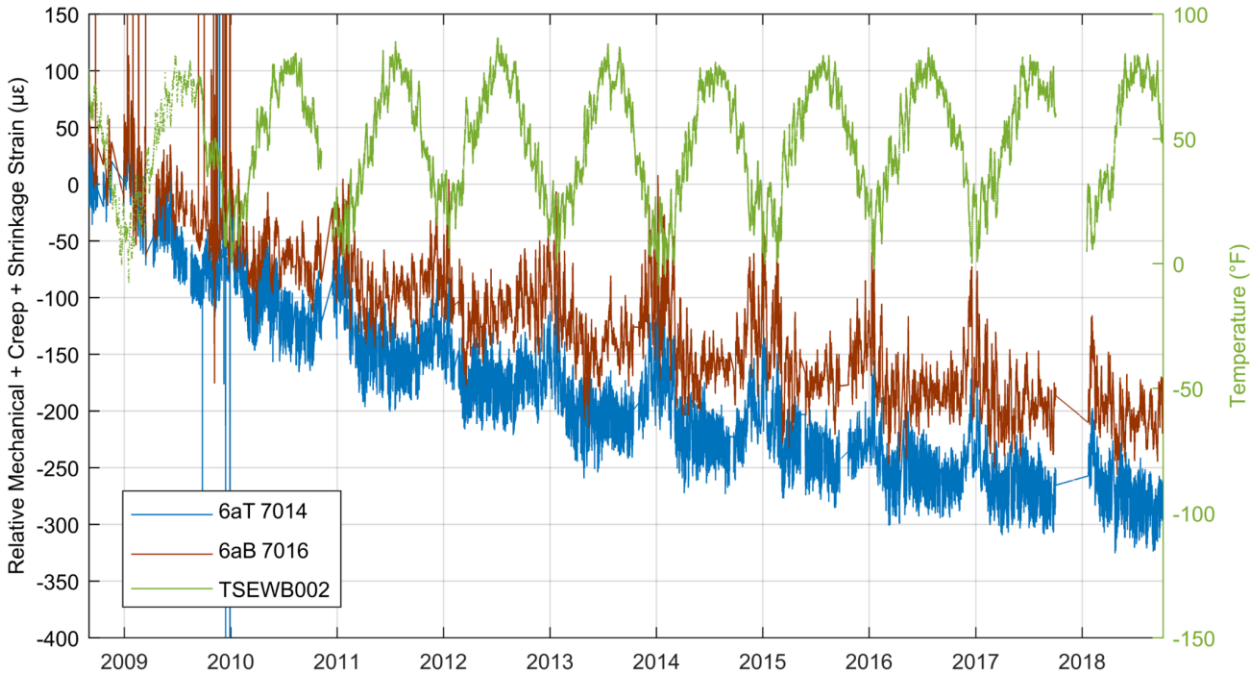

Figure 4.19: Relative mechanical strain plus creep and shrinkage strains for gages 6aT_7014 (blue; longitudinal gage on top flange at southbound Location 6a) and 6aB_7016 (red; longitudinal gage on bottom flange at southbound Location 6a).

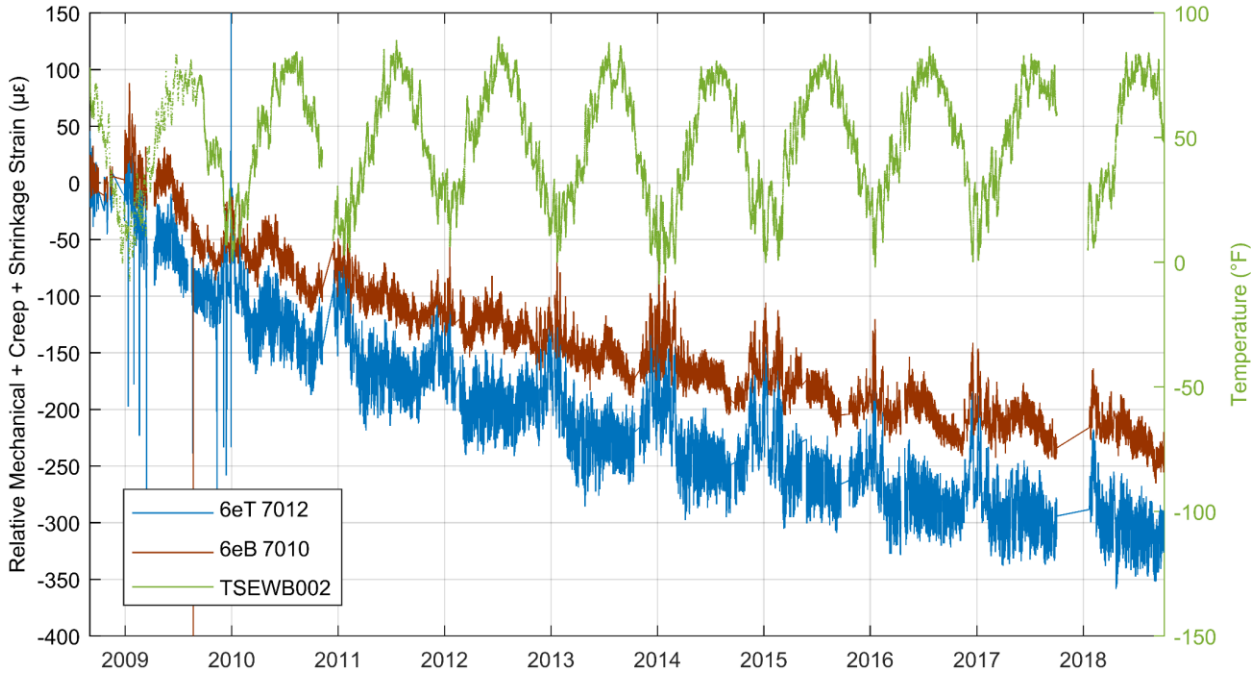

Figure 4.20: Relative mechanical strain plus creep and shrinkage strains for gages 6eT_7012 (blue; longitudinal gage on top flange at southbound Location 6e) and 6eB_7010 (red; longitudinal gage on bottom flange at southbound Location 6e).

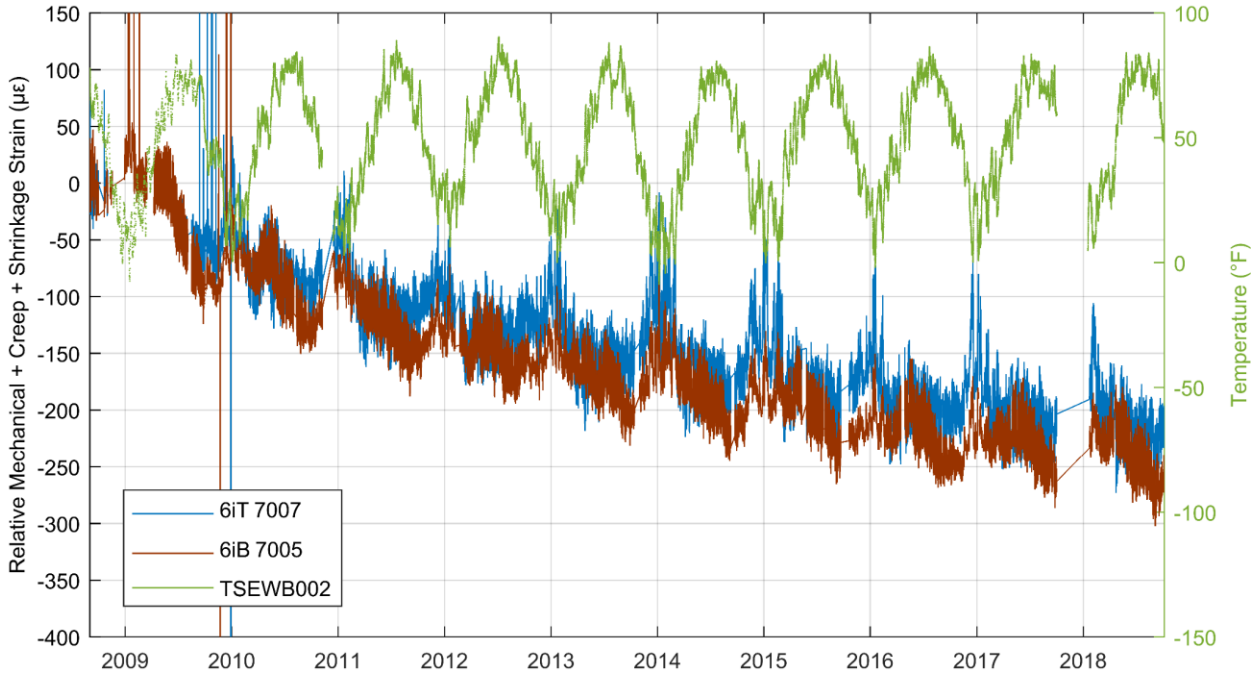

Figure 4.21: Relative mechanical strain plus creep and shrinkage strains for gages 6iT_7007 (blue; longitudinal gage on top flange at southbound Location 6i) and 6iB_7005 (red; longitudinal gage on bottom flange at southbound Location 6i).

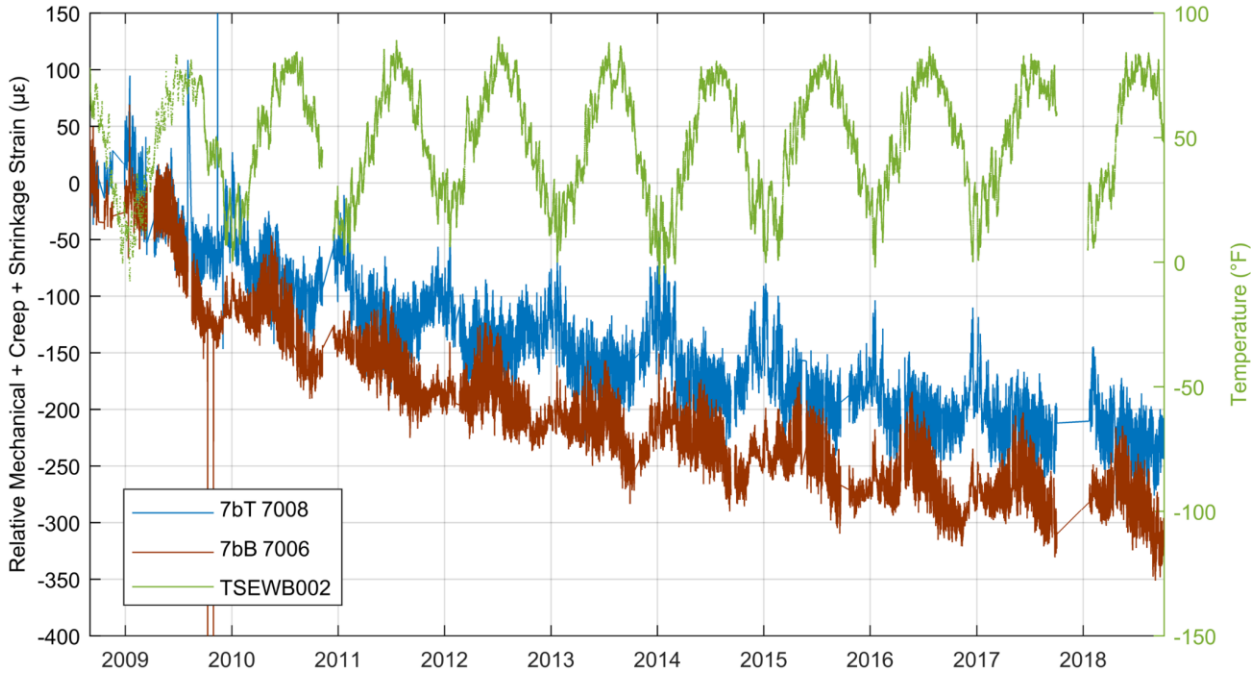

Figure 4.22: Relative mechanical strain plus creep and shrinkage strains for gages 7bT_7008 (blue; longitudinal gage on top flange at southbound Location 7b) and 7bB_7006 (red; longitudinal gage on bottom flange at southbound Location 7b).

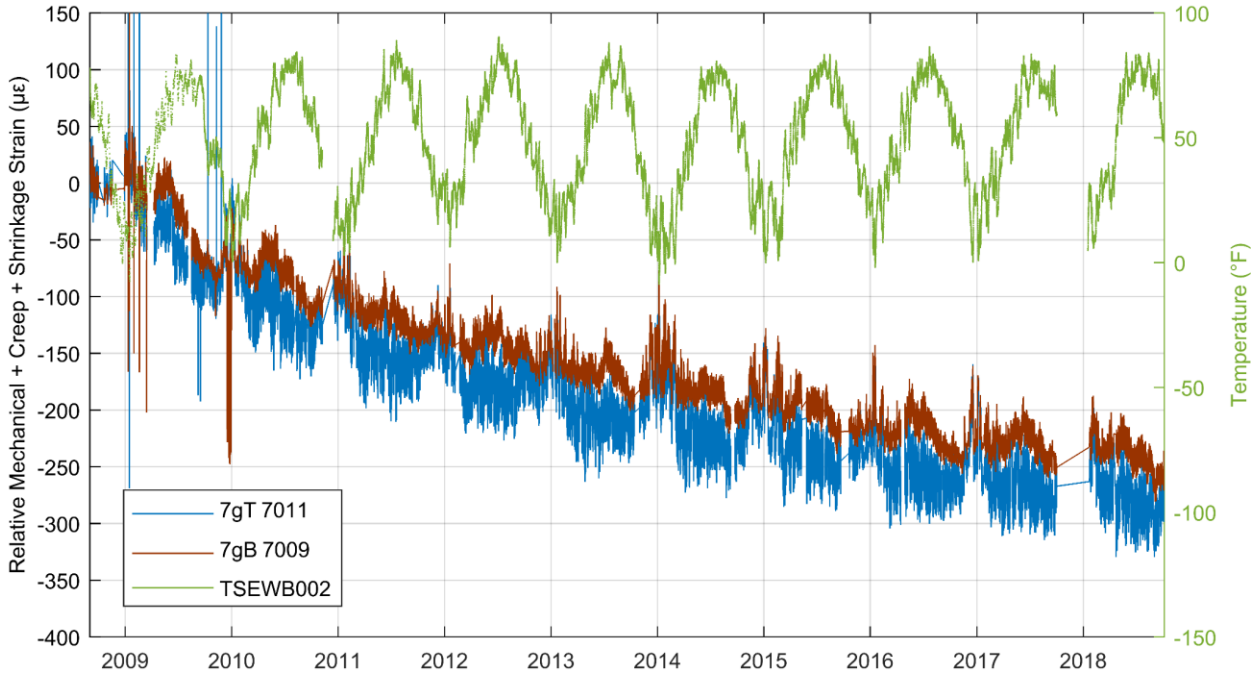

Figure 4.23: Relative mechanical strain plus creep and shrinkage strains for gages 7gT_7011 (blue; longitudinal gage on top flange at southbound Location 7f) and 7gB_7009 (red; longitudinal gage on bottom flange at southbound Location 7f).

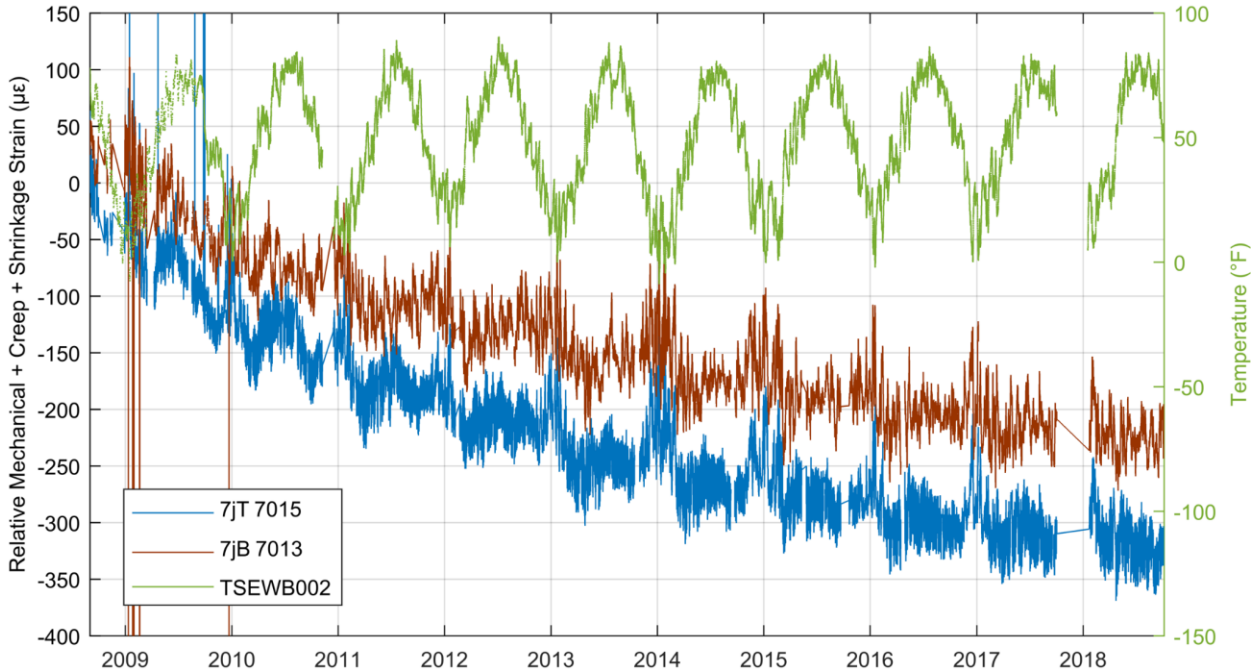

Figure 4.24: Relative mechanical strain plus creep and shrinkage strains for gages 7jT_7015 (blue; longitudinal gage on top flange at southbound Location 7j) and 7jB_7013 (red; longitudinal gage on bottom flange at southbound Location 7j).

4.3 CURVATURE COMPARISON BETWEEN VWSG AND SOFO GAGES

Comparing data from the truck tests completed during September 2008 and October 2010, detailed in French et al. (2012), was determined as the most effective measurement of bridge behavior for gage comparison. Curvature was calculated from the slope of the least-squares line fit to sets of gages through the depth of the cross sections. All strain data presented from the truck tests represents changes in strain due to the applied truck weight load, where unloaded readings were taken immediately before and after the truck tests. Positive curvature has been defined such that the top flange is in compression and the bottom flange in tension. Curvatures calculated from the static truck test data were one of the measurements used to validate the finite element models in French et al. (2012).

Truck test data was previously analyzed by French et al. (2012). The curvature plots from three truck tests (STI3SB, STI6SB, and STI7SB) are shown in Figures 4.25 through 4.27. Note that the vertical axis scale varies for these figures; the intent is to compare curvatures calculated using vibrating wire strain gages and SOFO fiber optic strain gages. Curvatures measured using the SOFO fiber optic sensors are shown with unfilled symbols, whereas locations with VWSGs are presented as filled symbols. Overall, the southbound curvature plots from the October 2010 tests were found to be nearly identical to those from the September 2008 tests, with the exception of test STI6SB (eight trucks across the width of the bridge at Location 6). The SOFO sensors near the midspan of Span 2 gave much higher strains than anticipated during the October 2010 STI6SB test, though curvature magnitudes recorded during STI6SB

tests were far less than during test STI7SB (eight trucks across the width of the bridge at Location 7, Figure 4.27). No malfunctions were detected in the gages at that time, and none of the three values that were averaged to obtain these results appeared to be anomalous. The measured response of the structure due to thermal gradients both before and after the October 2010 truck tests did not exhibit any notable change in the structural response, so it was believed that the differences noted here were not damage related. As mentioned in the previous report by French et al. (2012), the cause for this discrepancy was uncertain.

Generally, curvatures calculated using vibrating wire strain gages and SOFO fiber optic strain gages, when considered together, provide a reasonable curvature profile along the length of the bridge. Compared to the finite element model curvatures, the measured curvature at locations along Span 2 instrumented with SOFO fiber optic strain gages tended to be slightly over-predicted by the finite element model. The increased length of the SOFO fiber optic strain gages of 13 ft (4.0 m), as opposed to the vibrating wire gages with approximate gage lengths of 6.75 in. (170 mm), may have reduced the measured strain; as the fiber optic strains were effectively average strains along a 13-ft (4.0-m) chord along a non-prismatic cross section. This error was minor, and the strain results from the SOFO gages were still considered acceptable for finite element model validation.

Over the first ten years of operation, the maximum measured thermal gradient at Location 7 in the southbound structure occurred on April 20, 2014 at 15:00 CST. Change in curvature from the minimum measured thermal gradient of the previous night (April 20, 2014 at 6:00 CST) was calculated from total strains and mechanical strains and is plotted in Figure 4.28. There is relatively good agreement between curvatures calculated from vibrating wire strain gages and SOFO fiber optic strain gages. The change in curvature at midspan due to thermal gradients is nearly double that seen during truck test STI7SB, which involved eight sand trucks across the SB bridge at location 7 (near midspan).

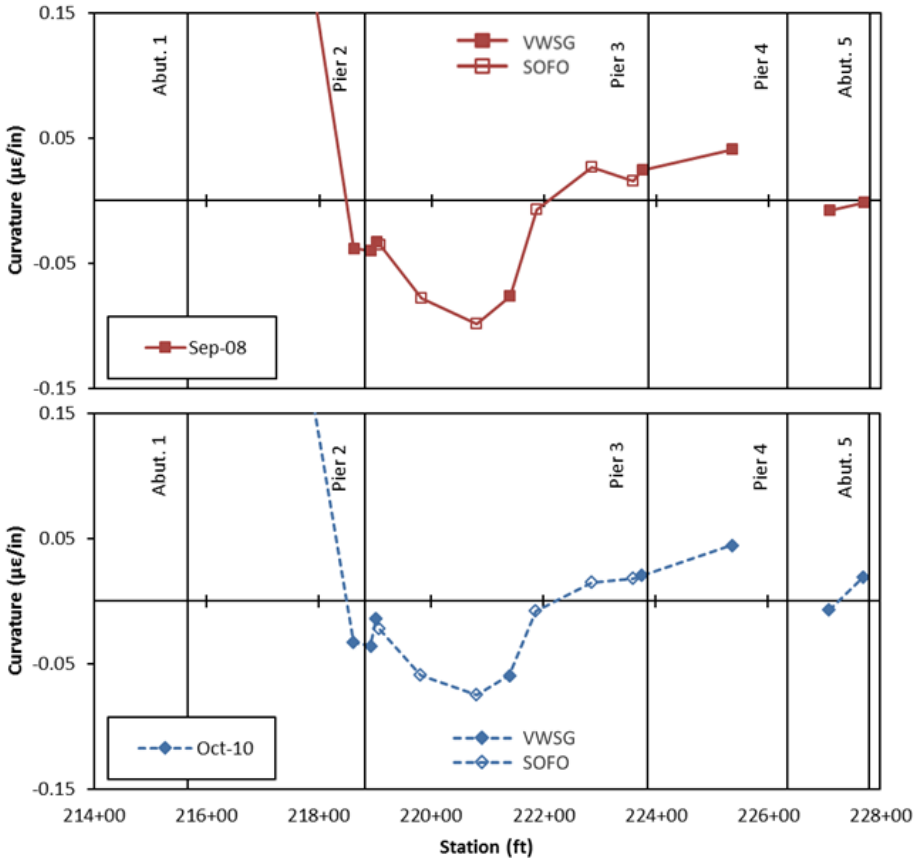

Figure 4.25: Comparisons of VWSG and SOFO curvatures from truck test STI3SB on September 2008 and October 2010 on southbound bridge.

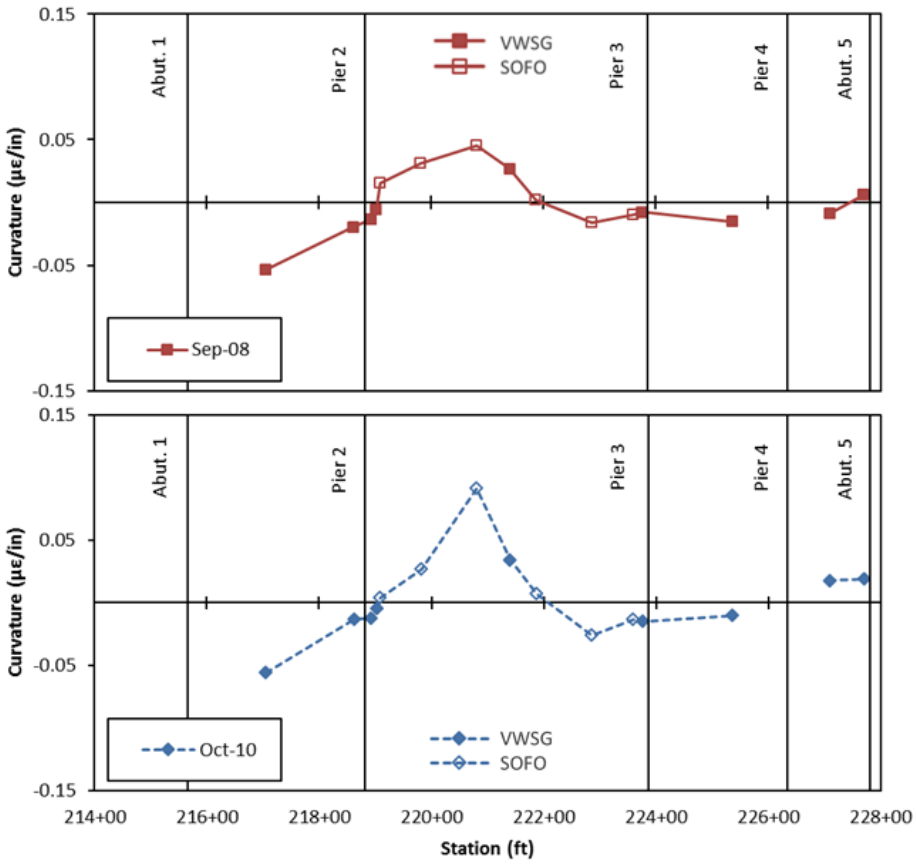

Figure 4.26: Comparisons of VWSG and SOFO curvatures from truck test STI6SB on September 2008 and October 2010 on southbound bridge.

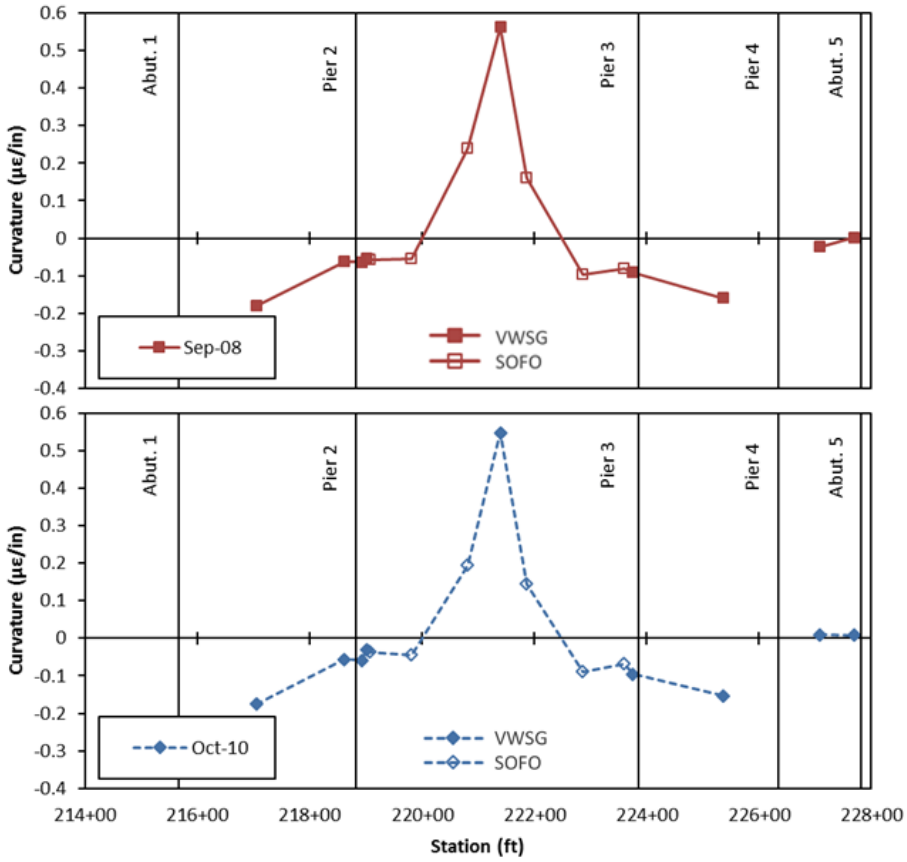

Figure 4.27: Comparisons of VWSG and SOFO curvatures from truck test STI7SB on September 2008 and October 2010 on southbound bridge.

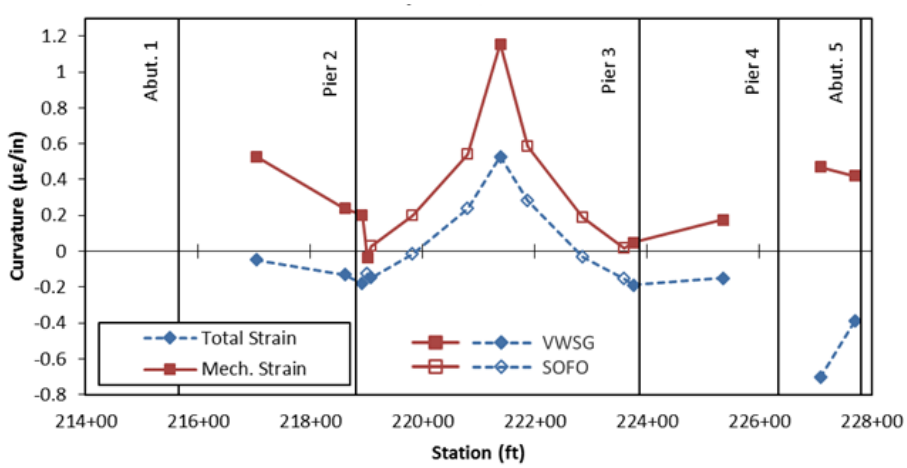

Figure 4.28: Change in curvature from minimum positive thermal gradient to maximum positive thermal gradient on April 20, 2014.

4.4 CONCLUSION

Strain measurements captured by both the vibrating wire strain gages and SOFO fiber optic strain gages were compared over the ten-year period. Temperature and time-dependent effects were heavily apparent in the measured strain changes, so the analysis focused on gage sensitivity to temperature and time-dependent strains. Compared to the vibrating wire strain gage mechanical strains, the SOFO mechanical strains contain higher error. This error is due to uncertainty in the concrete thermal expansion correction, which requires the use of temperature gages that may not accurately reflect the concrete temperature at the location of the SOFO gage. On the other hand, the long-term creep and shrinkage strains measured were similar for both systems.

For future use of SOFO gages, it is recommended that, at minimum, a temperature gage be installed directly below the concrete surface at the center of each SOFO gage. Depending on the longitudinal temperature variation in the cross section over the length of the SOFO gage, more embedded temperature gages may be necessary to accurately capture the internal concrete temperature.

CHAPTER 5: INVESTIGATION OF THERMAL GRADIENT EFFECTS

Temperature data was collected on the I-35W Saint Anthony Falls Bridge over the course of ten years using vibrating wire strain gages and thermistors, as documented in French et al. (2012). Bridge temperatures during the first three years of monitoring were investigated for thermal gradients and uniform temperature changes in French et al. (2012) and Hedegaard et al. (2013). The major findings from the initial investigations remain unchanged with the additional seven years of data.

This chapter presents a summary of the comparisons made between the measured thermal gradients and design gradients using updated data. Several thermal gradients were applied to the finite element model to study the effect of thermal gradient shape on design stresses. All times listed in this chapter are in Central Standard Time and have not been adjusted for daylight savings time.

5.1 THERMAL GRADIENTS BACKGROUND

Thermal gradients (i.e., variations in temperature through the cross section) in concrete bridge structures are caused by a combination of solar radiation, conduction, and convection with the surrounding atmosphere. The comparably low thermal conductivity of concrete causes the section to heat or cool non-uniformly during a daily cycle. These gradients are typically most pronounced through the depth of the cross section; the incident solar radiation heats the top surface of the bridge deck, and the heat flows down through the superstructure. Thermal gradients are defined positive when the top surface temperature is higher than the temperature in the webs and are generally observed in the late spring or early summer on clear, sunny, hot afternoons with high solar radiation. Negative thermal gradients, defined as the top surface temperature being lower than the temperature in the webs, are generally found during early mornings throughout the year.

Temperature differences in a section cause a structure to expand or contract nonuniformly. Under positive thermal gradients, for example, the top surface of the structure will expand more than the bottom surface, causing the structure to deflect upward. Restraints associated with boundary conditions induce axial bending stresses into the cross section. Furthermore, if the thermal gradient profile is nonlinear, compatibility stresses are generated to satisfy the assumption under Bernoulli beam bending that plane section remain plane. The stresses induced by thermal gradients can be larger than those induced by vehicle live loading (Hedegaard et al. 2013).

The American Association of State Highway and Transportation Officials Load and Resistance Factor Design (AASHTO LRFD) Bridge Design Specifications service limit state load combinations include the force effects due to thermal gradients (AASHTO 2017). The design thermal gradients suggested by AASHTO (2017) were based on numerical equations that model the heat flow problem in bridge structures. Design gradients describe the most extreme temperature variation in the bridge predicted by solving the heat flow equations with the solar radiation, ambient temperature, and wind speed of a region recorded over the course of a year to a typical bridge cross section (White et al. 2017).

The heat flow problem for bridge structures in the United States was considered by Potgieter and Gamble (1983), who expanded on previous works by Priestley (1978) and others. Potgieter and Gamble constructed a finite difference heat flow model and complemented their numerical study with field measurements from the Kishwaukee River Bridge, a segmental five-span continuous box girder bridge with blacktop covering located near Rockford, Illinois. The measurements revealed that the shape, but not the top surface magnitude, of the New Zealand Code gradient matched the measured thermal gradients.

The design gradient from the New Zealand Code (New Zealand Transport Agency 2018) is a fifth-order curve adopted from Priestley (1978), which decreases from a maximum gradient temperature at the top of the deck to zero at a depth of 47.2 in. (1200 mm). The fifth-order curve is applied to the section above the webs, through the depth of the webs, and to portions of the deck above unenclosed air. For portions of deck above enclosed air cells in box girders, a linear gradient is prescribed with temperature decreasing at a rate of 1°F per 0.44 in. (1°C per 20 mm). The bottom gradient tail temperature is specified as 2.7°F (1.5°C), decreasing linearly to zero over a height of 7.9 in. (200 mm) measured from the bottom of the section. The design negative thermal gradient is specified with a top surface temperature equal to -0.4 times the top surface temperature of the positive design thermal gradient, and linearly decreases to zero over a height of 11.8 in. (300 mm) measured from the top of the section.

The work of Potgieter and Gamble was advanced by Imbsen et al. (1985), in which climatic data from 26 representative locations throughout the United States were input into the heat flow equations to compute the maximum temperature differences of a 6.56 ft (2 m) deep concrete bridge structure at each geographic location. The computed temperature differences were superimposed on solar radiation contours of the United States for the month of July in order to obtain four broad solar radiation zones that best fit the regions with similar gradients. The shape of the positive thermal gradient for each zone proposed by Imbsen et al. (1985) was simplified from Priestley's (1978) fifth-order curve to a gradient constructed from three straight line segments. A modified version of the thermal gradient proposed by Imbsen et al. (1985) was incorporated into the first edition of the AASHTO LRFD Bridge Design Specifications (AASHTO 1994). The thermal gradient adapted into AASHTO LRFD considered two straight line segments that extended only 16 in (0.41 m) into the superstructure, a depth which was significantly reduced from previous researchers' proposed gradients. The solar radiation zones proposed by Imbsen et al. (1985) were adopted without alteration by AASHTO LRFD. Minneapolis is in solar radiation Zone 2. The positive thermal gradient recommendations in AASHTO LRFD have not been updated since 1994 (White et al. 2017). The design negative gradient for structures with plain concrete decks and no asphalt overlay is found by multiplying the AASHTO LRFD (2017) design positive gradient by -0.3.

A graphical comparison of the AASHTO LRFD (2017) and New Zealand Code (2018) positive design gradients, both scaled to the same top surface temperature, is presented in Figure 5.1. The New Zealand Code positive design gradient is also referred to as the Priestley curve in this report. Included in Figure 5.1 is the Priestley Linear gradient, which is prescribed by the New Zealand Code for decks above enclosed air cells in box girders. Even when the maximum gradient temperature values are equal, the area under the Priestley gradient curve is considerably larger than that under the AASHTO LRFD gradient.

A number of investigations regarding the effect of thermal gradients on concrete bridges have been conducted to verify that the code recommended thermal gradients are appropriate. Shushkewich (1998) investigated the measured thermal gradients of the North Halawa Valley Viaduct, a cast-in-place concrete box girder bridge in Hawaii. Positive and negative thermal gradients were found to correspond well with the AASHTO (1998) gradient proposals, which were identical to the thermal gradient provisions in AASHTO LRFD (2017). Thompson et al. (1998) considered the "Ramp P" structure, a curved precast segmental concrete box girder bridge on highway US 183 in Austin, Texas. Gradients were measured both with and without 2-in. (51-mm) blacktop covering. Measured gradients were typically lower than those specified in AASHTO LRFD (1994), which had an identical positive design gradient to AASHTO LRFD (2017) but used a multiplier of -0.5 instead of -0.3 for defining the negative gradient. However, it was stated that more data was needed to construct a sound statistical comparison. Roberts-Wollman et al. (2002) investigated thermal gradients in precast segmental concrete box girders in the San Antonio "Y" Project. They concluded that typical positive gradients could be approximated by a fifth-order curve similar to that presented in Priestley (1978). They also stated that the AASHTO LRFD (1994) positive and negative design gradient magnitudes were conservative for the San Antonio region. Rodriguez et al. (2013) measured thermal gradients of a cast-in-place, posttensioned, box-girder bridge in California over a one-year period. The authors found the shape and depth of the maximum measured positive and negative gradients to be similar to the AASHTO LRFD (2010) recommendations and the temperatures recommended by AASHTO to be conservative for positive and negative gradients. The temperature data from the I-35W Saint Anthony Falls Bridge was analyzed after three years of data collection and the AASHTO LRFD (2010) recommended gradient was found to be unconservative, while the Priestley fifth order curve more closely approximated measured data (French et al. 2012; Hedegaard et al. 2013). Overall, the applicability of the AASHTO LRFD thermal gradients has varied by location; however, limited data has prevented researchers from making general conclusions about the regional appropriateness of the current AASHTO LRFD guidelines.

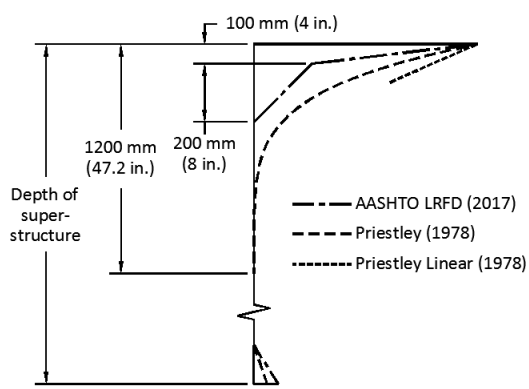

Figure 5.1: Comparison of AASHTO LRFD (2017) and New Zealand (Priestly 1978) positive design gradients (French et al. 2012). AASHTO LRFD (2017) design gradients are the same as those specified in AASHTO LRFD (2010).

5.2 COMPARISON OF MEASURED AND DESIGN THERMAL GRADIENTS

Measured thermal gradients of the I-35W Saint Anthony Falls Bridge superstructure were compared to AASHTO LRFD (2017) and New Zealand Code (2018) design gradients. AASHTO LRFD Eighth Edition (2017) design gradients were unchanged from the design gradients specified in AASHTO LRFD Fifth Edition (2010), the edition from which initial comparisons were made in French et al. (2012).

One segment of the southbound structure near the midspan of the river span (Location 7) was heavily instrumented with thermistors to explore the temperature distribution throughout the cross section. Characteristic sectional dimensions and the thermistor layout used for the investigation of thermal gradients at this section, including thermistors integral with the vibrating wire strain gages, are presented in Figure 5.2. Insufficient instrumentation prevented detailed investigation of thermal gradients at other locations within the northbound and southbound structures.

The positive and negative design thermal gradients used for comparison to the measured data are shown in Figure 5.3. The AASHTO LRFD positive and negative design gradients represent those applied to the I-35W Saint Anthony Falls Bridge in design (solar radiation Zone 2 for structures with plain concrete decks and no asphalt overlay). The New Zealand Code positive design gradient was the Priestley fifth-order gradient scaled to the same top surface gradient temperature as AASHTO LRFD solar radiation Zone 2 (henceforth referred to as the Priestley-Z2 gradient), as well as the Priestley Linear gradient for decks above the enclosed air cells. The New Zealand Code design negative thermal gradient with top surface temperature scaled to -0.4 times the AASHTO LRFD solar radiation Zone 2 positive gradient top surface temperature of 46°F (25.6°C) was referred to as the NZ-Z2 gradient.

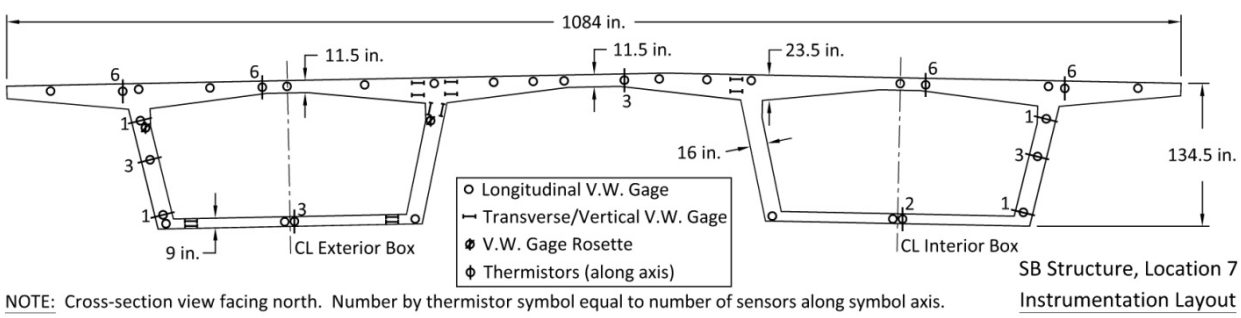

Figure 5.2: Characteristic section dimensions and instrumentation layout in southbound structure Location 7 (French et al. 2012).

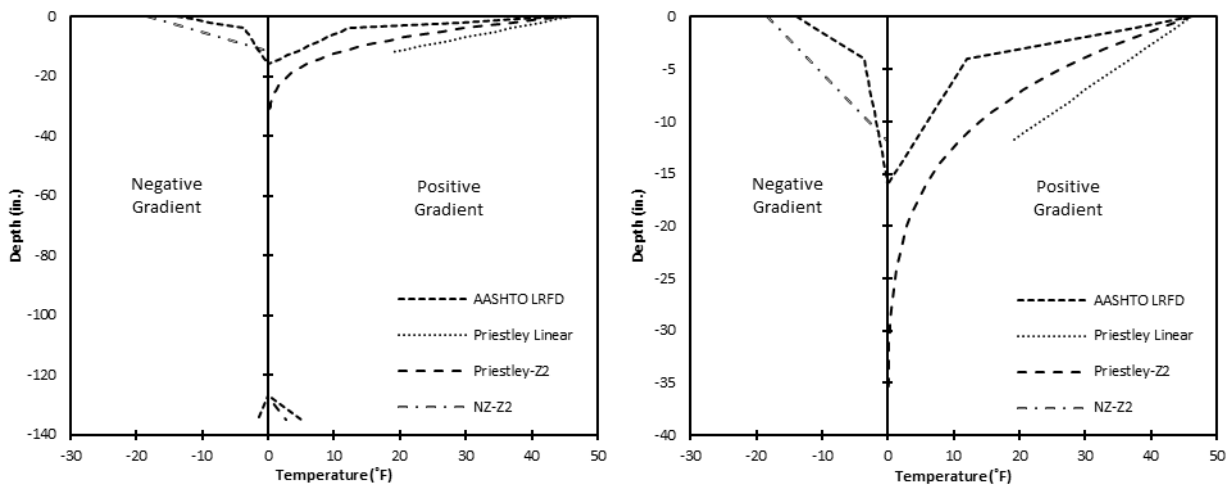

(a) Full depth of section (b) Zoomed

Figure 5.3: Postive and negative design gradients considered for comparison to measured thermal gradients at southbound Location 7 of the southbound structure. Priestley Linear only prescribed for decks above enclosed air cells in box girders.

5.2.1 Comparison of Gradient Magnitudes

The magnitude of the measured positive thermal gradients was taken as the difference between (1) the average of the operational topmost thermistors of all six-thermistor sets in the top flange and (2) the minimum measured temperature along the centerlines of the webs. Minimum temperatures were captured along the centerlines of the webs to minimize the influences of gradients through the thickness of the webs. The thermal gradients through the widths of the webs were typically not linear; often the temperature at the centerline of the web was lower than temperatures from both the outermost thermistor (with 2.25 in. (57 mm) of concrete cover) and the innermost thermistor (with 2.25 in. (57 mm) of concrete cover from the air inside the box). However, differences between any two web thermistors rarely exceeded 3.8°F (2°C) and thus were negligible compared with gradients through the depth of the box section.

Because top surface temperature measurements were not taken, comparisons made between measured and design gradient magnitudes required that the value of the design gradient at a depth of 2 in. (50 mm) below the top surface of the deck (where the topmost thermistor was located) be used. Consequently, the AASHTO LRFD positive gradient in Zone 2 (top surface gradient temperature equal to 46°F (25.6°C) prescribed for Minneapolis, MN) would have a magnitude of 29.0°F (16.1°C) at a depth of 2 in. (50 mm), and the Priestly fifth-order gradient scaled to the same top surface gradient temperature (Priestley-Z2 gradient) would have a magnitude of 37.1°F (20.6°C) at the same depth. These design gradient magnitudes at the depth of the thermistors are compared to the daily maximum measured positive gradient magnitudes from September 1, 2008 until October 6, 2018 in Figure 5.4a.

The measured positive gradients showed a strong seasonal trend. Temperature data collected prior to September 19, 2009 was sampled every six hours (midnight, 6:00 AM, noon, and 6:00 PM) and thus the maximum measured gradients appeared to be smaller during this time frame. Temperature data

collected after September 19, 2009 was sampled hourly. Figure 5.5a shows the number of days per month on which thermal gradient magnitudes exceeded the AASHTO LRFD design gradient magnitude at a depth of 2 in. (50 mm). The measured positive gradient magnitudes exceeded the AASHTO LRFD gradient magnitude on average 33 days per year[1] (standard deviation 5 days per year), usually in the late spring and early summer. The Priestley-Z2 positive gradient magnitude was only exceeded three times over the nine-year period in which data was sampled hourly.

It was observed that the daily maximum positive gradients often occurred between 2:00 PM and 4:00 PM. Figure 5.6 shows the daily maximum positive gradient magnitude as a function of time[1]. Each subplot represents the hour of the day on which the daily maximum positive gradient occurred. Within each plot, the histogram shows the number of days on which the daily maximum positive gradient magnitude was within a certain temperature range. The vertical dashed line represents the AASHTO LRFD (2017) positive gradient magnitude, which was most often exceeded on days with maximum positive gradient magnitudes occurring at 3:00 PM.

Negative gradient magnitudes were calculated in the same manner as positive gradients except taken as the difference between (1) the average of the operational topmost thermistors of all six-thermistor sets in the top flange and (2) the maximum measured temperature along the centerlines of the webs. AASHTO design negative gradients were considered by scaling the AASHTO LRFD positive gradient by -0.3 per AASHTO LRFD (2017) specifications. The New Zealand Code prescribes a linear negative gradient with a top surface temperature equal to -0.4 times the top surface temperature of the positive design thermal gradient (New Zealand Transport Agency 2018). Again, the design magnitudes were considered at a depth of 2 in. (50 mm) below the deck surface for comparison with measured negative gradients, as shown in Figure 5.4b. Figure 5.5b shows the number of days per month on which negative thermal gradient magnitudes exceeded the AASHTO LRFD design gradient magnitude at a depth of 2 in. (50 mm). The seasonal dependence of the negative gradient magnitudes was not as pronounced as that observed for the positive gradients, but the overall maximum negative gradients tended to occur during the winter months. The measured negative gradient magnitudes exceeded the AASHTO LRFD magnitudes on average 52 days per year[1] (standard deviation 10 days per year), whereas the NZ-Z2 design gradient magnitude was exceeded on average 2 days per year (standard deviation 1 day per year). Figure 5.7 shows that the daily maximum negative thermal gradients most often occurred between 5:00 AM and 8:00 AM.

[1] As determined from data that was sampled hourly (after September 19, 2009).

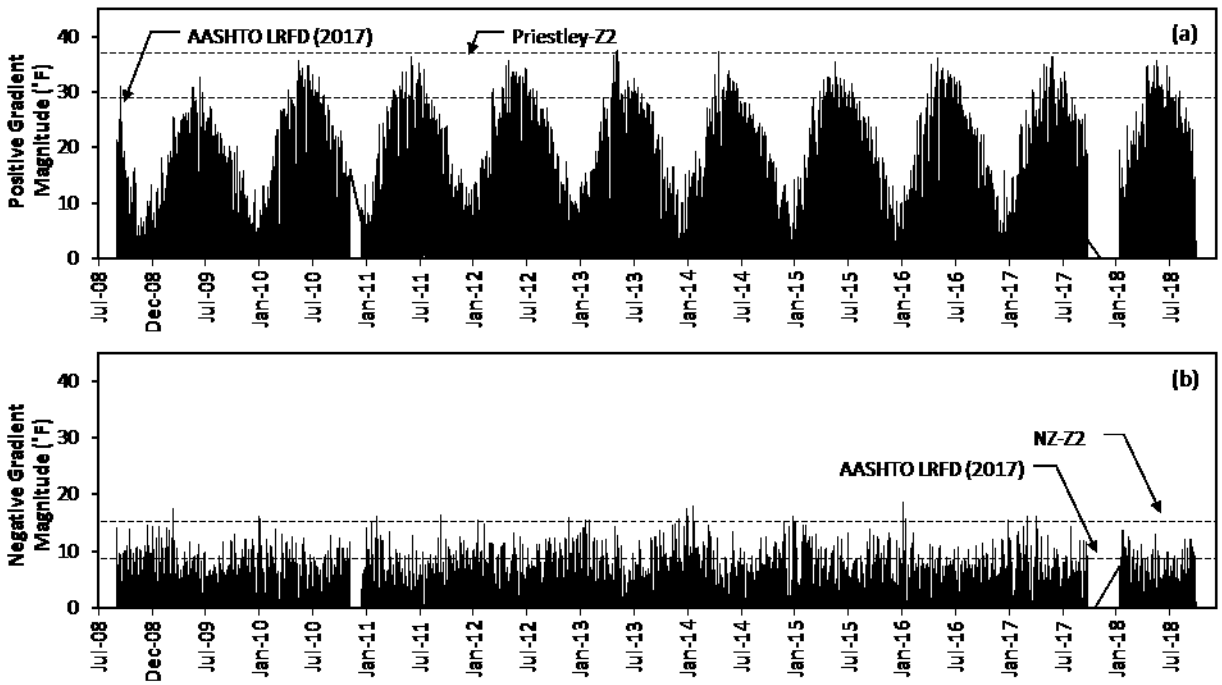

Figure 5.4: Measured (a) positive and (b) negative gradient magnitudes: design gradient magnitudes considered at a depth of 2 in. (50 mm) below the deck surface for comparison against measured gradients.

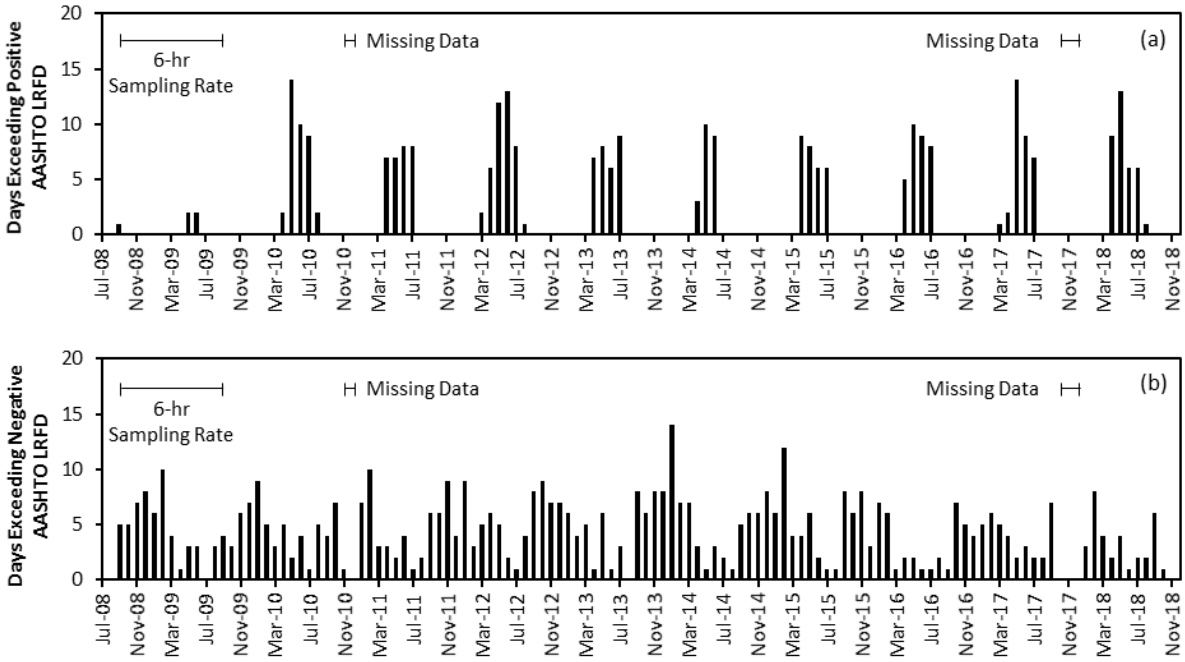

Figure 5.5: Number of days per month with measured (a) positive and (b) negative gradient magnitudes exceeding the AASHTO LRFD design gradient magnitude at a depth of 2 in. (50 mm) below the deck surface.

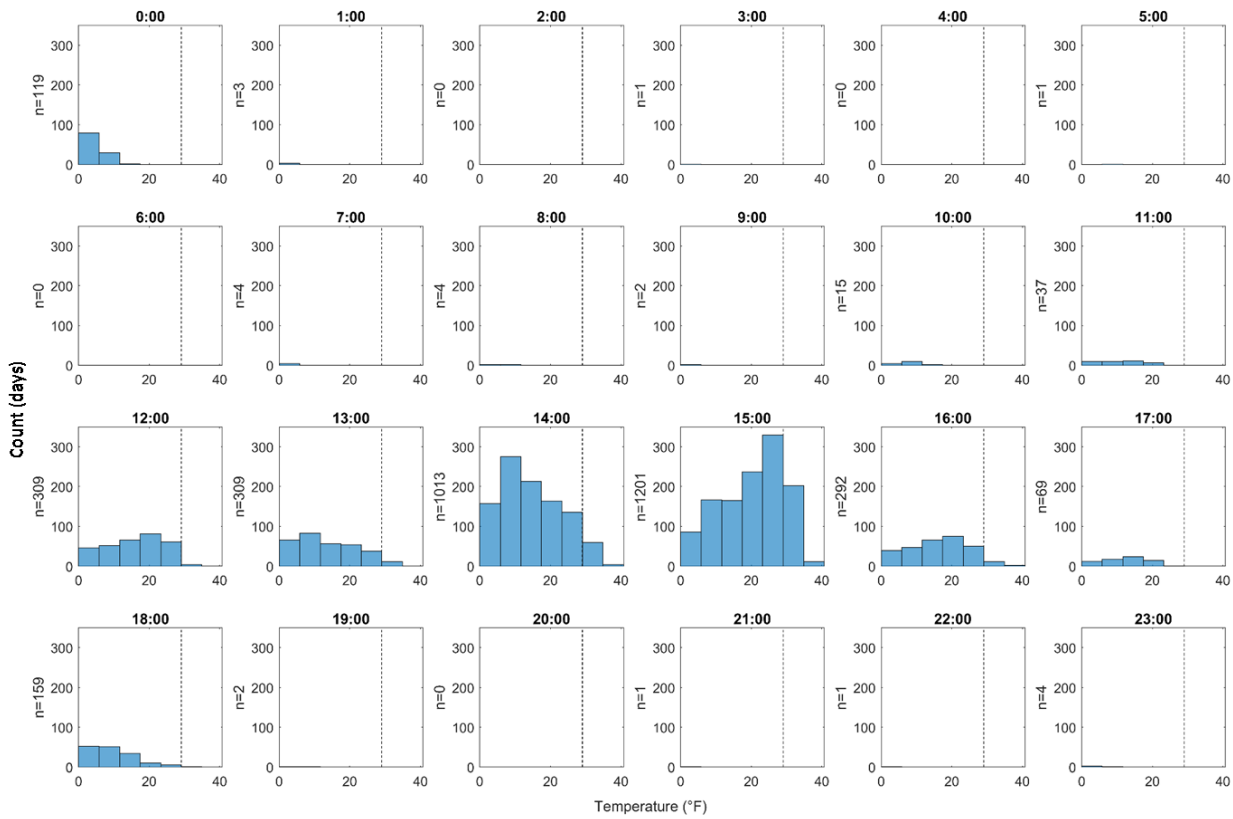

Figure 5.6: Daily maximum positive gradient magnitude as a function of time. Each subplot represents the hour of the day on which the daily maximum positive gradient occurred. Within each plot, the histogram shows the number of days (count) on which the daily maximum positive gradient magnitude was within a certain temperature range. The vertical dashed line represents the AASHTO LRFD (2017) positive gradient magnitude.

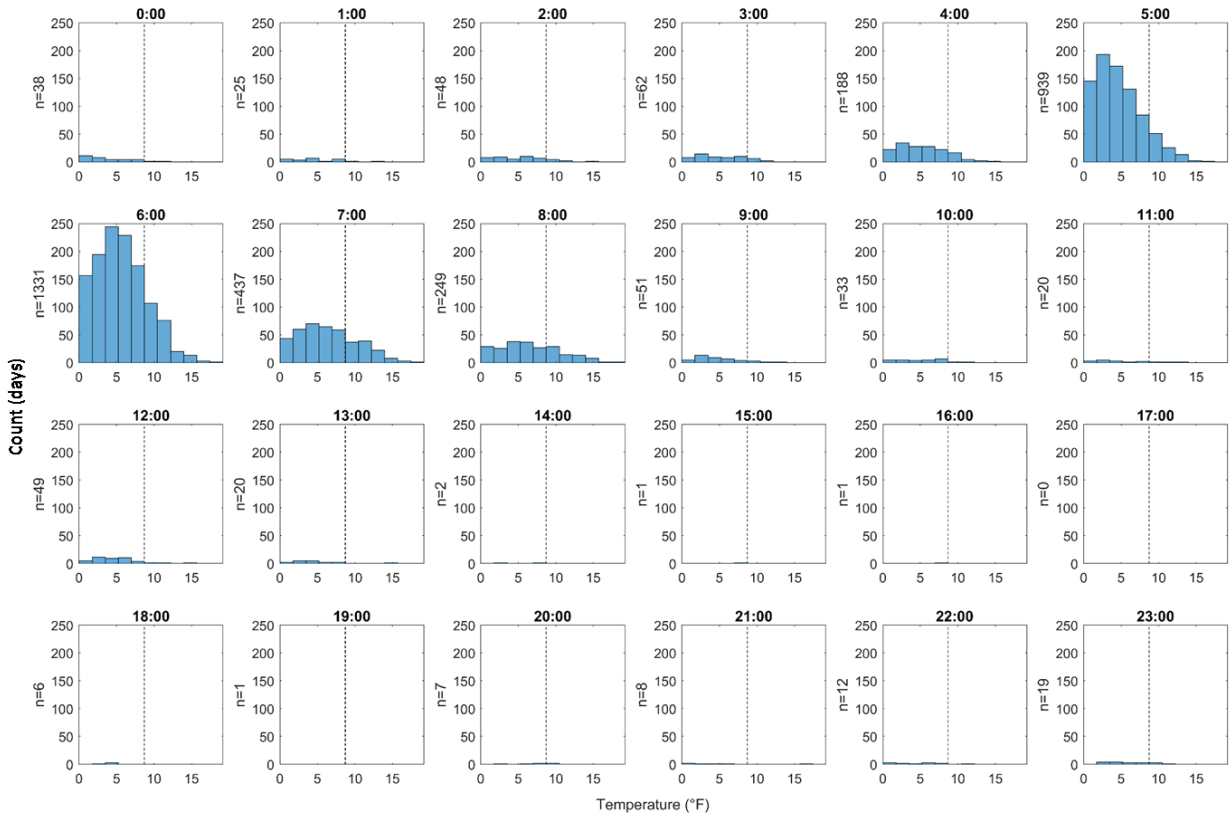

Figure 5.7: Daily maximum negative gradient magnitude as a function of time. Each subplot represents the hour of the day on which the daily maximum negative gradient occurred. Within each plot, the histogram shows the number of days (count) on which the daily maximum negative gradient magnitude was within a certain temperature range. The vertical dashed line represents the AASHTO LRFD (2017) negative gradient magnitude.

5.2.2 Comparison of Gradient Shapes

The five maximum measured positive gradients are plotted in Figure 5.8. Weather conditions taken from the Minneapolis-St. Paul Airport (approximately 7 miles (11 km) from the bridge) during the days of maximum measured positive gradients are presented in Table 5.1. The measured gradients were compared to the AASHTO LRFD design gradient for Zone 2, the Priestley-Z2 curve, and the Priestley linear gradient for decks above enclosed air cells assuming no blacktop and with top temperature scaled to the AASHTO LRFD Zone 2 top temperature magnitude. In all cases, the measured gradients were better approximated by the Priestley-Z2 curve than the AASHTO LRFD gradient. The Priestley linear gradient above the enclosed box was a poor fit at the centerline of the boxes. Gradients at the centerline of the boxes were not largely different from those measured along the webs. Gradient tails in the bottom flange ranged from 2.3 to 3.6°F (1.3 to 2.0°C).

The five maximum measured negative gradients are plotted in Figure 5.9 with corresponding weather conditions taken from the Minneapolis-St. Paul Airport presented in Table 5.2. The measured gradients were compared with the AASHTO LRFD Zone 2 design negative gradient assuming no blacktop and the NZ-Z2 design negative gradient. The measured negative gradients were much more diverse in shape

than the positive gradients and were not consistently matched in shape by the AASHTO LRFD design gradient or the NZ-Z2 design gradient, especially through the web of the cross section. The AASHTO LRFD negative design gradient consistently underestimated the measured temperature gradients, whereas the NZ-Z2 negative design gradient provided an upper bound to the measured negative gradients.

The measured temperature profile across the width of the cross section was observed to vary more in the morning (time of maximum negative gradient) than in the early afternoon (time of maximum positive gradients). Figure 5.10 shows the measured temperature profile at the time of the maximum measured positive gradient and the maximum measured negative gradient through the west web of the interior box and the east web of the interior box at southbound Location 7. At the time of the maximum measured negative thermal gradient, the topmost web thermistor in the west web of the exterior box measured 8.9°F (4.9°C) lower than the topmost web thermistor in the east web of the interior box. This temperature variation across the width of the section was typical for times of maximum negative gradients. However, the temperature profiles across the width of the cross section for times of maximum positive gradients were more uniform. An explanation for these observations may be that increased airflow around the west web of the exterior box, as compared to the east web of the interior box which is adjacent to the northbound structure, causes the exterior faces of the bridge to cool faster than the interior faces; whereas the concrete heating is less effected by convection than direct solar radiation.

Only Location 7 of the southbound structure was instrumented in a manner to investigate gradient shapes, but the consistency of thermal gradient magnitudes along the length of the structure was examined by considering the temperature difference between top and bottom flange vibrating wire strain gages at each instrumented section. Regardless of section geometry, the nominal locations of the top flange strain gages were consistently 5.5 in. (140 mm) below the deck top surface and bottom flange gages were 3.0 in. (76 mm) above the bottom fiber. Measured temperature in the top and bottom flanges along the length of the southbound superstructure on July 1, 2011 at 3:00 PM (corresponding to the maximum measured positive gradient within the first three years of monitoring) are presented in Figure 5.11. The top surface temperature was nearly uniform along the length of the bridge, but the bottom flange temperature dropped significantly near the piers. This drop was presumed to be caused by the large thermal mass of the pier diaphragms, the increase in thickness of the bottom flange, and possibly the additional shade and cover provided by the decorative fins at the tops of the piers. The top flange temperatures reinforce the idea of consistent thermal gradients along the length of the structure caused by solar radiation, whereas the bottom temperatures indicate the complexities of the heat transfer problem given varying geometry and thermal boundary conditions. Top and bottom flange temperature during other positive and negative gradients on both southbound and northbound structures showed similar trends (French et al., 2012).

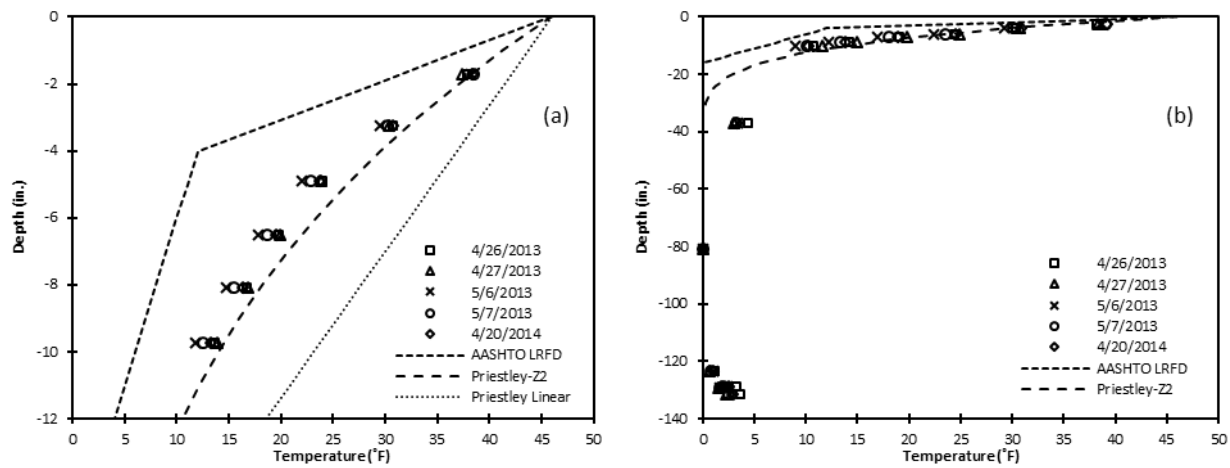

Figure 5.8: Maximum measured positive gradients at southbound Location 7 compared with design gradients through (a) centerline of exterior box, top flange only, and (b) along centerline of west web of exterior box.

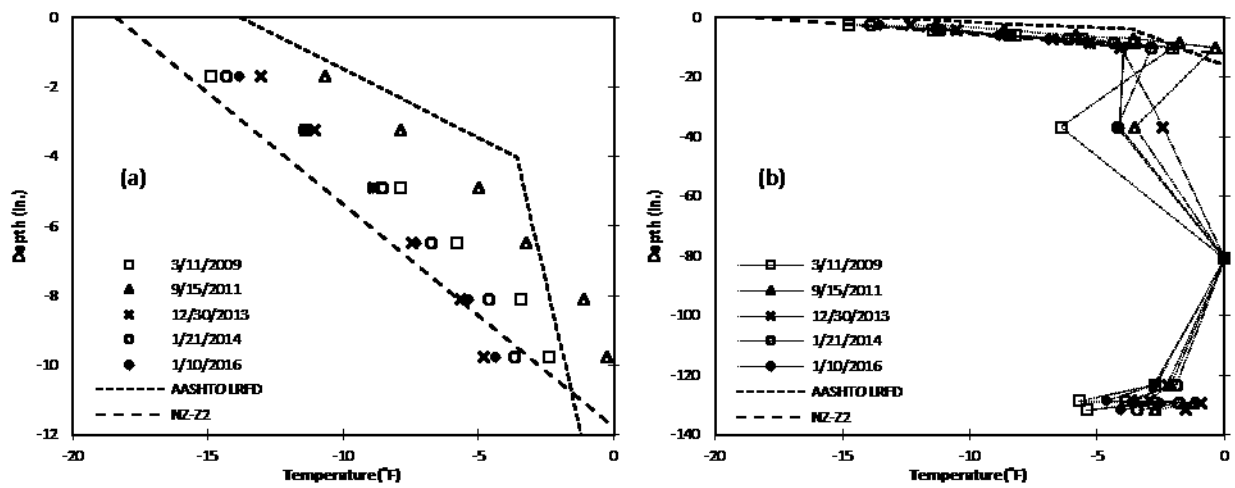

Figure 5.9: Maximum measured negative gradients at southbound Location 7 compared with design gradients through (a) centerline of exterior box, top flange only, and (b) along centerline of west web of exterior box.

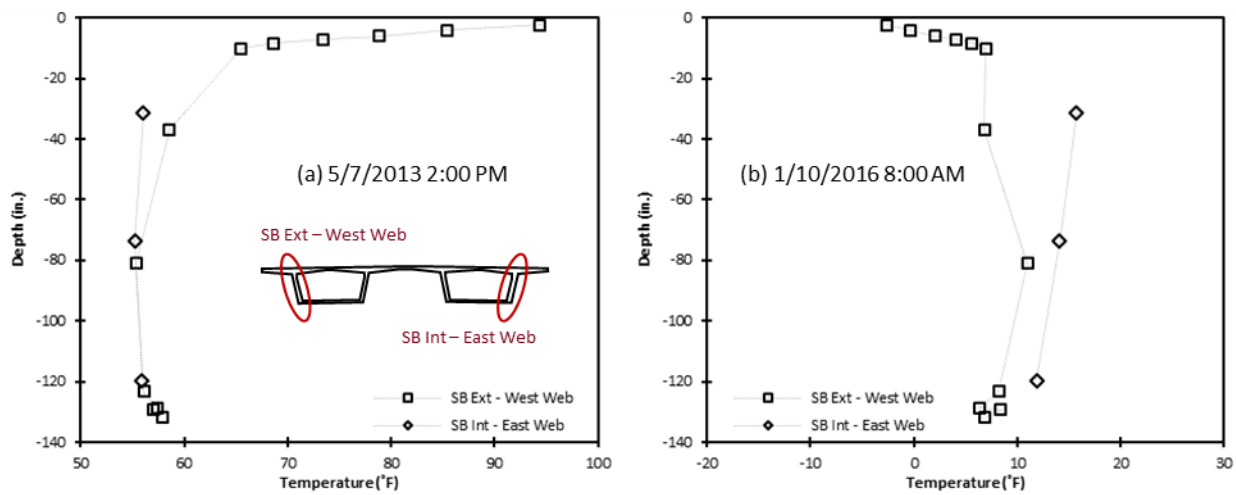

Figure 5.10: Measured temperature profiles at the time of (a) the maximum measured positive gradient (5/7/2013 2:00 PM) and (b) the maximum measured negative gradient (1/10/2016 8:00 AM) through the west web of the exterior box and the east web of the interior box at southbound Location 7.

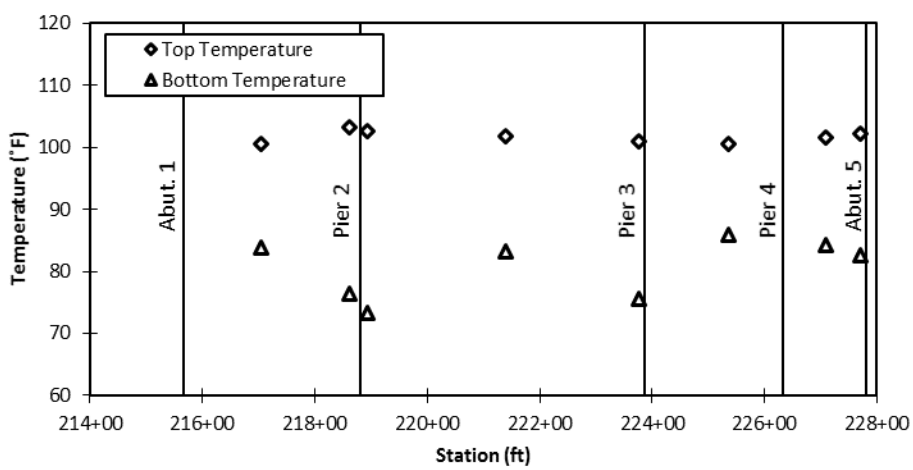

Figure 5.11: Measured temperature in top and bottom flanges along the length of the southbound superstructure on July 1, 2011 at 3:00 PM. Corresponds to maximum measured positive gradient over first three years of monitoring (French et al. 2012).

Table 5.1: Dates, times, and weather conditions for maximum measured positive thermal gradients during the first ten years of monitoring

Date	Maximum gradient time (CST; hrs.)	Daily maximum temperature (°F)	Daily minimum temperature (°F)	Daily mean wind speed (mph)	Daily precipitation (in.)	Weather Events
4/26/2013	1500	72	45	8.5	0.0	Clear
4/27/2013	1500	75	43	5.82	0.0	Clear morning, partly cloudy afternoon
5/6/2013	1400	76	46	2.46	0.0	Clear morning, partly cloudy afternoon
5/7/2013	1400	78	53	3.8	0.0	Mostly cloudy morning, partly cloudy in afternoon
4/20/2014	1500	74	45	4.25	0.1	Partly cloudy morning with light rain, clear afternoon

Table 5.2: Dates, times, and weather conditions for maximum measured negative thermal gradients during the first ten years of monitoring.

Date	Maximum gradient time (CST; hrs.)	Daily maximum temperature (°F)	Daily minimum temperature (°F)	Daily mean wind speed (mph)	Daily precipitation (in.)	Weather Events
3/11/2009	600	8	-3	16.11	0.0	Clear
9/15/2011	600	58	36	3.36	0.0	Clear early morning, mostly cloudy afternoon, overcast evening
12/30/2013	600	2	-11	3.8	0.1	Cloudy morning with light snow, cloudy afternoon
1/21/2014	700	6	-13	6.26	0.0	Mostly cloudy morning, cloudy afternoon
1/10/2016	800	-1	-10	8.28	0.0	Scattered clouds in morning and afternoon

5.3 MODELING OF DESIGN AND MEASURED THERMAL GRADIENTS

The two-dimensional (2D) finite element model constructed in French et al. (2012) was used to predict the structural response of the I-35W Saint Anthony Falls Bridge when subjected to thermal effects. The model was previously validated using the five maximum measured positive thermal gradients over the first three years of monitoring and was then applied to compute the structural response due to the investigated design gradients. The previous analysis found that the experimentally derived stresses and curvatures best matched, on average, the predictions using the Priestley-Z2 gradient scaled to match AASHTO LRFD Zone 2 top surface temperature. Furthermore, the deformations and stresses produced by the scaled Priestley gradient (and by extension, the measured values) were considerably larger than those from the AASHTO LRFD design positive gradient. For example, the predicted curvatures and bottom fiber tensile stresses at midspan of the river span caused by the Priestley-Z2 positive gradient

were nearly 80% larger than those using the AASHTO LRFD design thermal gradient. It was concluded that the AASHTO LRFD (2010) design positive gradient was not necessarily conservative for this structure (French et al. 2012).

To further consider thermal gradient effects on design, several additional thermal gradients based on the updated thermal data were applied to the finite element model. Also, the effect of measured vs. nominal material properties was considered.

5.3.1 FEM Material Properties

Two different paradigms for assigning material properties to the finite element model were examined: measured material properties and nominal material properties. For the "measured" case, the modulus of elasticity and coefficient of thermal expansion of the materials were selected based on laboratory measurements taken as documented in French et al. (2012). This was intended to model the bridge using the best available knowledge of the in-situ material properties. For the "nominal" case, nominal or design material properties were assumed for all materials. This was intended to model the bridge as might be done in design when in-situ conditions are not known.

Material properties used for the "measured" case are provided in Table 5.3. The modulus of elasticity for the superstructure concrete was computed for a composite material (i.e., law of mixtures) consisting of a concrete matrix with steel reinforcement at a typical superstructure reinforcement ratio of 0.25%. The concrete modulus was estimated from Section 19.2.2.1(b) of ACI 318-14 using the mean measured 28-day strength of 7.45 ksi (51.4 MPa), and the steel reinforcement modulus was 29,000 ksi (200 GPa). The modulus of elasticity for the pier concrete was similarly calculated assuming a typical pier reinforcement ratio of 0.4%. However, because no measurements were given for the 28-day strength of the pier concrete, instead the mean 28-day strength was assumed to be 4.4 ksi (30.4 MPa), which was 10% higher than the nominal 28-day day strength of 4.0 ksi (27.6 MPa). Modulus values for post-tensioning steel and the elastomeric material, and Poisson's ratio for all materials, were taken as typical nominal values. Coefficient of thermal expansion values for the concrete materials were estimated from laboratory testing documented by French et al. (2012). Thermal expansion of the steel was assumed to be the typical nominal value, while the elastomeric material was assumed not to expand or contract with temperature.

Material properties used for the "nominal" case are provided in Table 5.4. Concrete modulus of elasticity was estimated per Section 5.4.2.4 in the AASHTO LRFD (2010) assuming the nominal 28-day strengths of 6.5 ksi (44.8 MPa) for the superstructure and 4.0 ksi (27.6 MPa) for the piers. The modeled modulus accounted for the composite material of a concrete matrix with steel reinforcement in the same manner as done for the "measured" case. The concrete coefficient of thermal expansion was assumed to be 6.0 $\mu\varepsilon/°F$ (10.8 $\mu\varepsilon/°C$) for both the superstructure and pier concrete, per recommended values in Section 5.4.2.2 in AASHTO LRFD (2010). Both modeling cases used equivalent properties for Poisson's ratio for all materials, and for all material properties for the post-tensioning steel and elastomeric bearings.

Table 5.3: Modeled material properties – measured case.

Material Description	Modulus of Elasticity (ksi) [GPa]	Coefficient of Thermal Expansion (με/°F) [με/°C]	Poisson's Ratio
Concrete in superstructure Nominal 28-day design strength = 6.5 ksi (44.8 MPa)	5,000 [34.5]	5.56 [10.0]	0.2
Concrete in piers Nominal 28-day design strength = 4.0 ksi (27.6 MPa)	4,000 [27.6]	4.85 [8.73]	0.2
Post-tensioning steel (axial stiffness only)	28,500 [196.5]	6.78 [12.2]	0.3
Elastomeric bearing (effectively incompressible)	10 [0.07]	0	0.4999

Table 5.4: Modeled material properties – nominal case.

Material Description	Modulus of Elasticity (ksi) [GPa]	Coefficient of Thermal Expansion (με/°F) [με/°C]	Poisson's Ratio
Concrete in superstructure Nominal 28-day design strength = 6.5 ksi (44.8 MPa)	4,730 [34.5]	6.00 [10.8]	0.2
Concrete in piers Nominal 28-day design strength = 4.0 ksi (27.6 MPa)	3,860 [27.6]	6.00 [10.8]	0.2
Post-tensioning steel (axial stiffness only)	28,500 [196.5]	6.78 [12.2]	0.3
Elastomeric bearing (effectively incompressible)	10 [0.07]	0	0.4999

5.3.2 Applied Thermal Gradients

Eight thermal gradients were applied to the finite element model and the longitudinal stress and strain profile along the length of the structure were examined. Two positive gradients were applied, while six different negative gradients were investigated. The thermal gradients are summarized in Table 5.5.

The Priestley-Z2 Positive and AASHTO Positive gradients were the design gradients shown in Figure 5.3, both scaled to the same top surface temperature equal to 46°F (25.6°C). The gradient in the bottom 8 in. (0.20 m) of the cross section, also known as the tail, was neglected in both cases for simplicity.

Two negative design gradients were investigated. The Priestley-Z2 Negative (-0.4) used the same fifth-order gradient as Priestley-Z2 Positive, but with a top surface temperature equal to –18.4°F (–10.2°C), which represents a scale factor of –0.4 between the negative gradient and the positive gradient. AASHTO LRFD (2017) suggests that the applied negative gradient be scaled from the design positive gradient by a factor of –0.3. The investigations of the measured gradients on the I-35W St. Anthony Falls

Bridge (Section 5.2), however, indicated that a factor of –0.3 may not be conservative, while a factor of –0.4 provides an upper bound to the measured negative gradients. The NZ-Z2 Negative (-0.4) was the design negative gradient from the New Zealand Code, as referenced in Section 5.1.

Four thermal gradients shown in Figure 5.12, each representing a different simplification of the negative gradient temperature profile measured in the southbound bridge at 6:00 AM CST on March 11, 2009, were investigated. Within the deck, all four applied thermal gradients used the same temperature distribution given by a parabolic function determined by linear regression to be the best fit of the measured temperatures at Location 7:

$$T_g(y) = -19.552 + 2.2814y - 0.0551y^2,\ 0 \leq y \leq 12.11 \tag{5-1}$$

where *y* is the coordinate in inches measured down from the top of the deck.

Measured 1 Negative applied the parabolic fit of Equation (1) along the entire length of the bridge from the top surface down to a depth of 12.11 in. (308 mm) below the top surface, with zero thermal gradients elsewhere (see Figure 5.12a). Per the parabolic fit, the top surface temperature was equal to –19.6°F (–10.9°C), which was a slightly greater magnitude than that from the two design negative gradients.

Measured 2 Negative used the same deck gradient as that for Measured 1 Negative down to a depth of 10.16 in. (258 mm) below the top surface, which was the position of the lowest thermistor in the deck at Location 7. From depths of 10.16 in. (258 mm) to 36.92 in. (938 mm) below the top surface, the temperature varied linearly with depth from –2.06°F (–1.14°C) to –6.40°F (–3.56°C), which matched the measured temperature in thermistor T23 at depth of 36.92 in. (938 mm). Temperature then varied linearly from –6.40°F (–3.56°C) down to zero over depth from 36.92 in. (938 mm) to the position of thermistor T24 at 81.0 in. (2060 mm) below the top surface. This three-step gradient (see Figure 5.12b) through the deck and upper portion of the webs was applied along the entire length of the bridge.

Measured 3 Negative (Figure 5.12c) and Measured 4 Negative (Figure 5.12d) were identical to Measured 2 Negative except with an additional bottom flange gradient only near the piers. Application of this gradient was supported by the measurement in the bottom flange of Location 8, where the temperature was 14.5°F (8.05°C) less than the temperature measured 81 in. (2.0 m) below the top surface at Location 7. The shape of the gradient through the bottom flange was unknown, and so two different gradients were assumed. For Measured 3 Negative, the tail gradient was defined as a line beginning at a depth 241.2 in. (6.13 m) below the top surface and decrease at a rate of 0.310°F/in. (6.78°C/m). This tail gradient was applied only to sections where the section depth was greater than 241.2 in. (6.13 m), which was within approximately 65 ft (20 m) of the centerlines of the piers. For Measured 4 Negative (Figure 5.12d), the tail gradient was defined as a line beginning at a depth 81 in. (2.0 m) below the top surface and decrease at a rate of 0.0645°F/in. (1.41°C/m). This tail gradient affected all cross sections with depth greater than 81 in. (2.0 m), which was nearly all sections along the bridge except for a portion near midspan of Span 4.

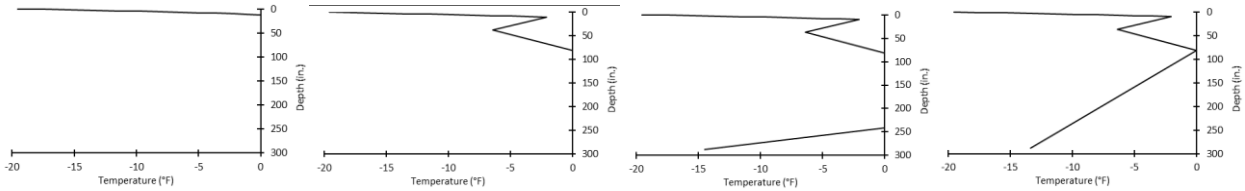

(a) Measured 1 Negative (b) Measured 2 Negative (c) Measured 3 Negative (d) Measured 4 Negative

Figure 5.12: Simplifications of negative measured thermal gradient.

Table 5.5: Thermal gradients applied to finite element model.

Gradient Name	Gradient Description
Priestley-Z2 Positive	Fifth-order curve, Ttop = 46°F (25.6°C)
AASHTO Positive	Bi-linear curve, Ttop = 46°F (25.6°C)
Priestley-Z2 Negative (-0.4)	Fifth-order curve, scaled as –0.4 of Prieslty-Z2
NZ-Z2 Negative (-0.4)	Linear function, Ttop = –18.4°F (–10.2°C)
Measured 1 Negative	Deck gradient, measured values fit to parabola
Measured 2 Negative	Deck gradient plus top of web variation
Measured 3 Negative	Deck gradient plus top of web variation plus bottom flanges near piers
Measured 4 Negative	Deck gradient plus top of web variation plus tail over entirety of bridge

5.3.3 Thermal Gradient Stress Results

Comparison of the Priestley-Z2 Positive and Priestley-Z2 Negative (-0.4) thermal gradient effects showed that the top and bottom fiber concrete stresses scaled with the applied thermal gradient. In other words, the Prestley-Z2 Negative concrete stresses were -0.4 times the stress levels computed from the Priestley-Z2 Positive design gradient. Because of this observation, the AASHTO Negative (-0.3) thermal gradient stress levels were approximated by scaling the AASHTO Positive results by a factor of -0.3 without running the finite element model again.

The top and bottom fiber concrete stresses computed for the AASHTO Positive, Priestley-Z2 Positive, AASHTO Negative, and NZ-Z2 Negative design thermal gradients are shown in Figure 5.13 and 5.14 for the finite element models with measured and nominal material properties, respectively. The FEM stress results for models using the measured and nominal material properties were similar; the maximum difference between the stress profiles computed for the two material properties cases was 26 psi (170 kPa).

Similar to the conclusions drawn in French et al. (2012) which considered thermal stresses at Location 7, the stress profiles in Figure 5.13 show that the chosen design gradient has a significant effect on the resulting stress demands that would need to be accounted for in design. The New Zealand Code gradient shapes (Priestley-Z2 Positive and NZ-Z2 Negative) consistently produced larger stress demands than the AASHTO LRFD (2017) design thermal gradients.

Only one segment of the southbound structure (Location 7) was instrumented such that the temperature distribution throughout the cross section could be analyzed. As such, the thermal gradient

shapes near the piers, especially the bottom tail, was relatively unknown. The implications of not truly knowing the distribution along the length of the structure could be observed by analyzing the stress effects of the four measured negative thermal gradients shown in Figure 5.12. Figure 5.15 shows the top and bottom fiber stresses resulting from the thermal gradients shown in Figure 5.12. The analysis was run on the FEM model with measured material properties. The bottom tail of the negative gradient (present in Measured 3 Negative and Measured 4 Negative gradients) had a significant effect on the resulting stresses.

It should be reiterated that only one segment of the southbound structure (Location 7) was instrumented such that the temperature distribution throughout the cross section could be analyzed. As such, thermal gradients applied in the 2D model varied only with depth. Thus, despite changing sectional properties along the length, and especially the great increase in thermal mass at the diaphragms, the gradient shape was assumed constant along the length of the structure. Such an assumption would typically be used for design purposes, but it is possible that the maximum gradient shape changes along the length of the structure. For future monitoring projects where thermal gradient shapes are of interest, it is recommended that sections with considerably different sectional properties be instrumented to capture the gradient shape along the length of the structure.

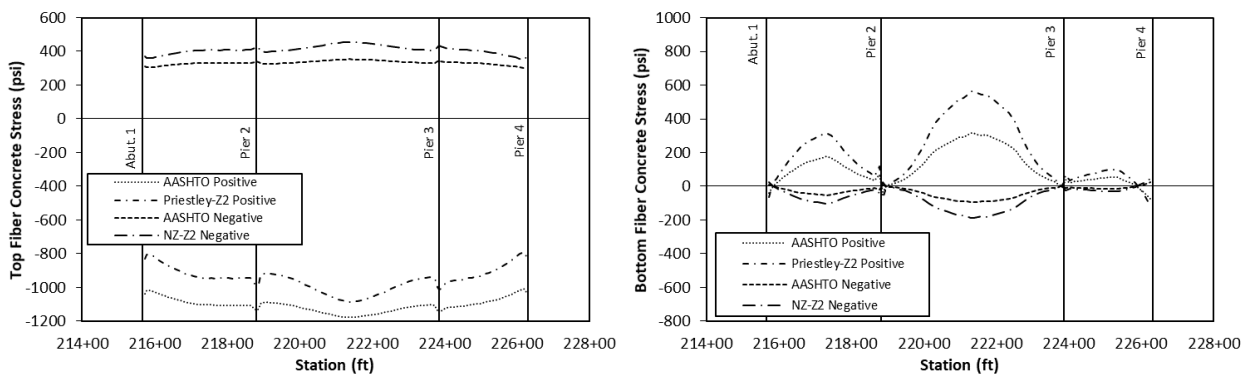

(a) Top Fiber Concrete Stress (b) Bottom Fiber Concrete Stress

Figure 5.13: Design thermal gradient stresses for FEM model with measured material properties.

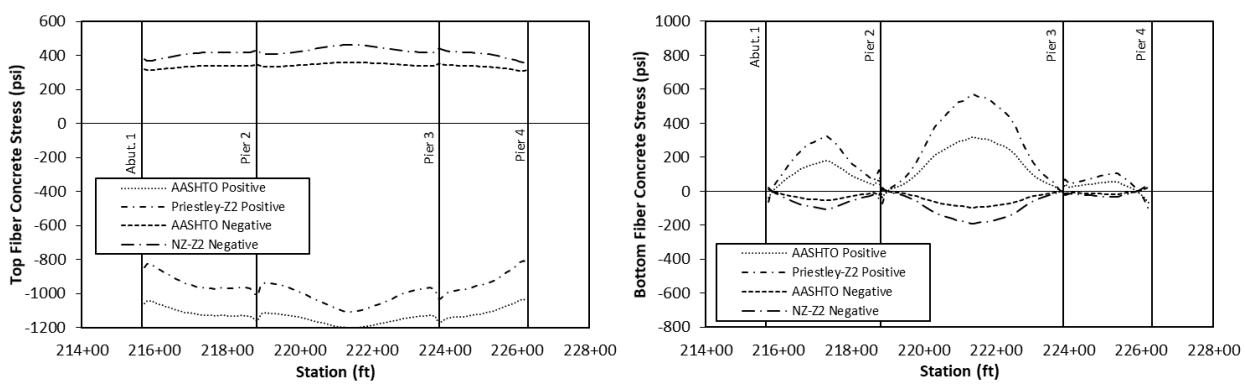

(a) Top Fiber Concrete Stress (b) Bottom Fiber Concrete Stress

Figure 5.14: Design thermal gradient stresses for FEM model with nominal material properties.

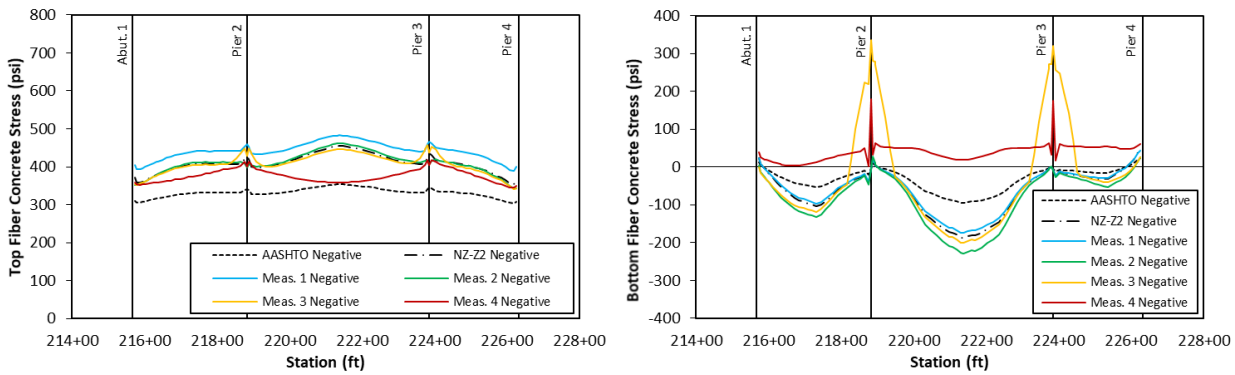

(a) Top Fiber Concrete Stress

(b) Bottom Fiber Concrete Stress

Figure 5.15: Negative thermal gradients stresses using FEM model with measured material properties.

5.4 THERMAL GRADIENT CONCLUSIONS

Thermal gradients were extracted from the temperature data measured along the southbound bridge. The midspan (Location 7) was heavily instrumented, which allowed for comparison of the shapes along the depth to the design gradients. The additional seven years of data emphasized that the Priestley and New Zealand design gradients scaled to AASHTO Zone 2 most effectively capture the temperature behavior. The maximum positive and negative gradients regularly exceed the AASHTO design specifications. Additionally, the impact of the gradients on temperature design stresses showed that the New Zealand design gradients produced larger stress demands along the length. Several variations of measured negative thermal gradients, which could be a concern for serviceability of the deck were considered in the stress analysis; the bottom tail of the negative gradient may have a significant effect on the resulting thermal stresses.

CHAPTER 6: LONG-TERM TIME-DEPENDENT BEHAVIOR OF AS-BUILT STRUCTURE

The long-term, time-dependent displacements and strains of the I-35W St. Anthony Falls Bridge were compared with those predicted using existing creep and shrinkage models. The linear potentiometer, thermistor, and vibrating wire strain gage data was used to extend the time-dependent displacement analysis completed in French et al. (2014) and provide updated documentation of the time-dependent behavior of the bridge. The as-built time-dependent response was compared to predicted behavior based on several time-dependent models applied to the finite element model (FEM) of the bridge.

The time-dependent behavior of the bridge was extracted from measured data containing both time- and temperature-related deformations using the methodology presented by French et al. (2014). Linear regression was performed on the measured data, y, using fitting functions based on temperature readings, T, at midspan of Span 2 (Location 7 in Figure 3.1) and an approximation of the long-term predicted behavior of the structure, θ_{TD}, in order to remove the temperature dependence from the data. The total response for the linear regression is approximated as:

$$y = \alpha_1 \frac{\int TdA}{T_{ref}A} + \alpha_2 \frac{\int T^2\, dA}{T_{ref}^2 A} + \alpha_3 \frac{\int zTdA}{T_{ref} I_x / L_{ref}} + \alpha_4 \theta_{TD} + \alpha_5 + \delta \tag{6-1}$$

where A is the cross-sectional area at midspan of Span 2, α are the regression coefficients, δ is the residual error, and the reference temperature, T_{ref}, is 68 °F. FEM predictions based on the 1990 CEB/FIP Model Code were used in the linear regression as the assumed form of the time-dependent behavior function. After determining the fitting coefficients on the temperature terms in the regression, the measured time-dependent behavior was determined by subtracting the temperature-dependent terms of the linear regression from the measured data, ideally leaving only the time-dependent component of the measurements (the last three terms in Eq. 6-1).

Figure 6.1 shows the average bridge temperature used to determine the time-dependent behavior in the long-term measured data. The average bridge temperature was calculated as the area weighted average of all operational thermistors at Location 7, as described in French et al. (2014). Large daily and seasonal average temperature variations were observed. The maximum and minimum measured average temperature was 100°F (37.9°C) and -16.0°F (-26.7°C), respectively.

French et al. (2014) observed that, despite removing the temperature-dependent behavior using linear regression, the time-dependent data still showed seasonal trends. Time-dependent displacements and strains slowed during the winters and sped up during the summers, indicating that concrete aging, creep, and shrinkage processes are functions of both time and temperature. To account for the temperature dependent rates of these concrete processes, the timescale of the extracted time-dependent data was adjusted using the Arrhenius equation to result in an equivalent time series at a constant reference temperature of 68°F. This adjustment effectively contracted time when the

temperature was below 68°F and expanded time when the temperature was above 68°F. The Arrhenius adjusted age was based on the average bridge temperature history measured at Location 7 of the southbound structure. Adjusted age equal to zero corresponded to when the midspan closure pour was placed on July 25, 2008. This time-adjustment procedure allowed for the comparison of the time-dependent predictions from constant-temperature FEM analysis with the readings from the in-situ monitoring system.

Six different time-dependent models were applied to the FEM model for comparison to the readings from the in-situ monitoring system. The resulting behavior of the time-dependent models, which incorporated the full construction sequence, could be divided into three categories: (1) the AASHTO and ACI 209 models, which quickly approached low asymptotic values; (2) the CEB/FIP 1978 and 1990 Model Code models, which asymptotically approached moderate ultimate values; and (3) the B3 and GL2000 models, which followed a logarithmic form and returned the highest deformations (French et al. 2014).

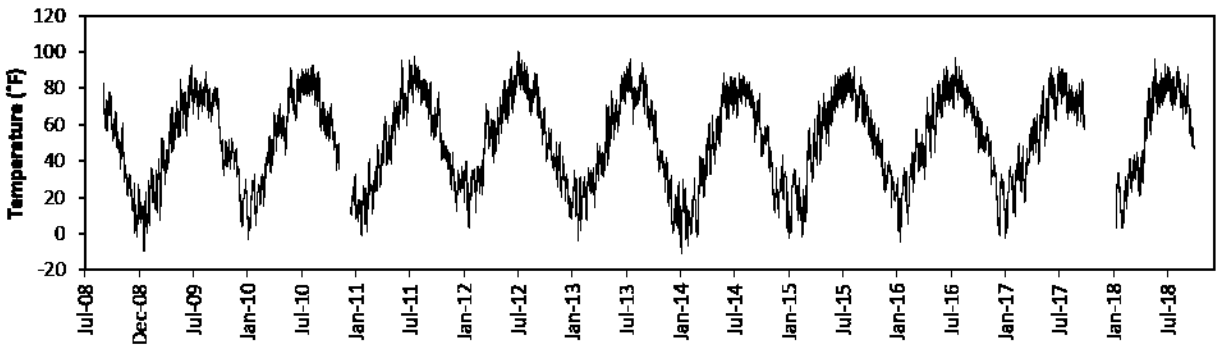

Figure 6.1: Average bridge temperature determined by an area-weighted average of thermistor data at the midspan of southbound Span 2 (Location 7).

6.1 TIME-DEPENDENT DISPLACEMENTS

Linear potentiometers (LPs) were located inside the boxes of the superstructure to monitor the longitudinal movement of the bridge at the expansion joints (see Figure 3.4). The LPs measured bridge movement with respect to the Abutment 1 (Span 1) or Pier 4 (Span 3 and 4); larger positive displacements corresponded to bridge shortening. Two LPs, one in the interior box and one in the exterior box, recorded data at each location (e.g., southbound structure Span 1, northbound structure Span 3, etc.). Unless otherwise noted, the relative movements measured by the two linear potentiometers at each location were averaged together for the purpose of regression analysis and data presentation. Regression analysis was not conducted for the LPs attached to Span 4 at Pier 4 because the pinned connection between the pier and Span 4 superstructure at this location meant that these sensors could not capture temperature- and time-dependent behavior.

Extraction of the time-dependent component of the LP data was performed using the 1990 CEB/FIP Model Code time-dependent curve. This time-dependent curve was chosen because prior analysis in

French et al. (2014) established that this curve best fit measured data during the first few years of the bridge service life. Regardless of the chosen time-dependent equation for the linear regression, however, the resulting time-dependent component of the data remained largely unchanged for southbound Span 3, northbound Span 1, and northbound Span 3 LP data. The estimated time-dependent deflections from each LP location are given in Figure 6.2, plotted with respect to unadjusted time. As mentioned previously, despite removing the temperature-dependent behavior to arrive at the time-dependent behavior, the data showed seasonal trends that are particularly pronounced during the first two years after bridge opening. This seasonal time-dependent behavior highlights the importance of using the Arrhenius adjusted age.

The southbound Span 1 LP data required the use of Heaviside functions in the linear regression procedure because of presumed data jumps after sensor replacement. Sensor replacements at other locations did not warrant the use of Heaviside functions because of the relatively short interruption in readings for these replacements. Heaviside fitting functions were applied to the southbound Span 1 data with jumps occurring on April 8, 2013, July 25, 2013, August 6, 2013, and January 18, 2018 (equivalently 1232, 1356, 1371, and 2530 adjusted age days). As a result, the time-dependent displacement approximation of the southbound Span 1 LP data was dependent on the chosen time-dependent model. The introduction of the Heaviside function forced the extracted time-dependent behavior to follow the time-dependent predictions. Figure 6.3 shows the time-dependent displacement approximations for the southbound Span 1 LP data for several time-dependent models. The time-dependent model most closely matching the measured bridge behavior was assumed to provide the best time-dependent displacement approximation. Measured data consistently fell between the 1990 CEB/FIP Model Code and ACI 209 FEM model predictions. As a result, the 1990 CEB/FIP Model Code time-dependent model was chosen for the final regression analysis because it provided a conservative estimate of the time-dependent component of the southbound Span 1 LP data. Furthermore, the 1990 CEB/FIP Model Code provides a theoretically more realistic time-dependent curve compared to ACI 209. The ACI 209 model does not properly scale up to large structures such as the St. Anthony Falls Bridge because the ratio of the volume to exposed surface area is not effectively considered.

The linear potentiometer readings measuring displacements with respect to Abutment 1 and Pier 4 were combined to observe the total bridge elongation/contraction behavior. LP measurements from Span 1 and Span 3 were added for the northbound and southbound structures, and the linear regression analysis was performed on the combined data to extract the time-dependent displacements. The Span 1 and Span 3 LP data contained different periods of data outages; readings for the combined case were considered only if both Span 1 and Span 3 measurements were available. The time-dependent displacements for the combination of Span 1 and Span 3 LP measurements are shown in Figure 6.4. Generally, the combined time-dependent displacements were similar for both the northbound and southbound structures.

Results from the time-dependent finite element model of the St. Anthony Falls Bridge (French et al. 2014) were compared to measured data from the installed linear potentiometers. For results from the LPs attached to Span 1 at Abutment 1, changes in displacement predicted by the model were assumed to correspond directly with displacements measured by the sensors; it was assumed that Abutment 1

did not move with time. On the other hand, the FEM deflections from Span 3 could not be directly compared to the data from LP sensors attached to Span 3. The modeled results captured only the time-dependent shortening of the continuous three-span structure. In contrast, the sensors attached to Span 3 measured the relative deflection between the top of Pier 4 and the Span 3 superstructure. Because Span 4 was pinned to the top of Pier 4 and integral with Abutment 5, time-dependent deflections of Span 4 and Abutment 5 caused corresponding movement in the attached boundaries. Given that Pier 4 was flexible compared to the integral Abutment 5, the total time-dependent shortening of Span 4 was assumed to translate as an equivalent horizontal deflection of Pier 4 and Abutment 5 was assumed as a fixed condition. Under these assumptions, the time-dependent effects extracted from the Span 3 LPs included the total shortening of Span 4 plus a portion of the shortening of the continuous Spans 1 through 3. Span 4 was not explicitly modeled in the finite element model, and so as an alternative, the time-dependent axial deformation of Span 4 of the southbound bridge was estimated by hand using each considered time-dependent model (French et al. 2014). The estimated deflections at the Span 3 expansion joint due to shortening of Spans 1 through 3 (FEM) combined with the shortening of Span 4 (hand calculation) was representative of the deflections that were measured by the Span 3 linear potentiometers.

The longitudinal deflections at Span 1 from the FEM results are compared to the southbound Span 1 sensor data from October 31, 2008 until April 18, 2019 in Figure 6.5 and northbound Span 1 sensor data in Figure 6.8. The computed longitudinal deflections summed from the finite element model at Span 3 and the hand calculations from Span 4 are compared to the southbound Span 3 sensor data from September 28, 2009 until April 18, 2019 in Figure 6.6 and Figure 6.9 for the northbound case. In Figure 6.7, the combination of the predicted longitudinal deflections at Span 1 and Span 3 are compared to the summed southbound Span 1 and Span 3 LP data from October 5, 2009 until April 18, 2019. The combination of the predicted longitudinal deflections at Span 1 and Span 3 are compared to the summed northbound Span 1 and Span 3 LP data from October 5, 2009 until April 18, 2019 in Figure 6.10. The computed deflections were set equal to the measured results at 10:00 AM CST on May 16, 2010 (adjusted age equal to 405 days) for the purposes of comparison. For these plots, only relative deflections were meaningful, as the total movement at the expansion joints since bridge completion was unknown. Gaps in the data were due to either sensor or data acquisition system failures.

For Figures 6.5 through 6.7, four subplots are presented. These subplots represent identical data, but parts (a) and (c) represent the time frame for the FEM results out to an adjusted age of 150 years and 80 years, respectively, while parts (b) and (d) zoom in to show the time frames with measured data (10.5 years). Parts (a) and (b) are plotted with respect to log adjusted time, while parts (c) and (d) are plotted with respect to linear adjusted time. Given that 1 year of real time was approximately equal to 0.75 years in Arrhenius adjusted time for the measured temperature history of the St. Anthony Falls Bridge, the 150-year adjusted age analysis corresponded to nearly 200 years in real time.

The measured time-dependent longitudinal deflections were nearly linear with respect to log time. From inspection of the Span 1 LP data in Figure 6.5, the AASHTO and ACI 209 model results appeared to provide accurate relative deflections from 100 adjusted age days until approximately 400 adjusted age days after the closure pour (October 31, 2008 until May 16, 2010, which approximately coincided with

the first 1.5 year of bridge operation). After this point, however, the AASHTO and ACI 209 models began to systemically underestimate the measured deflections, indicating that these models approached their asymptotic bounds more quickly than indicated by the measured data. The AASHTO and ACI 209 models had reached their asymptotic limits within 3 to 5 years after construction, while the extracted time-dependent results for the first 10 years showed only slight signs of asymptotic behavior.

The B3, 1978 CEB/FIP Model Code, 1990 CEB/FIP Model Code, and GL2000 models overestimated the measured time-dependent deflections extracted from the linear potentiometer data, while the AASHTO and ACI 209 models underestimated the measured time-dependent deflections. Over the course of the 10.5 years of measurement at the Span 1 expansion joint, measured time-dependent deflections amounted to 1.25 in. (32 mm). The 1990 CEB/FIP Model Code model provided better estimates than the B3, GL2000, and 1978 CEB/FIP Model Code, but still overestimated the measured deflections by 0.60 in. (15 mm) over the 10.5 years of measurement. The ACI 209 model provided the closest prediction over the 10.5-year period, for which the estimated Span 1 expansion joint longitudinal deflection was 0.36 in. (9 mm) less than the measured time-dependent deflection. The Span 3 LP data, as well as with the combined Span 1 and Span 3 LP data, are also bounded by ACI 209 and the 1990 CEB/FIP Model code finite element results; however, they are closer to the estimates from 1990 CEB/FIP model than ACI 209.

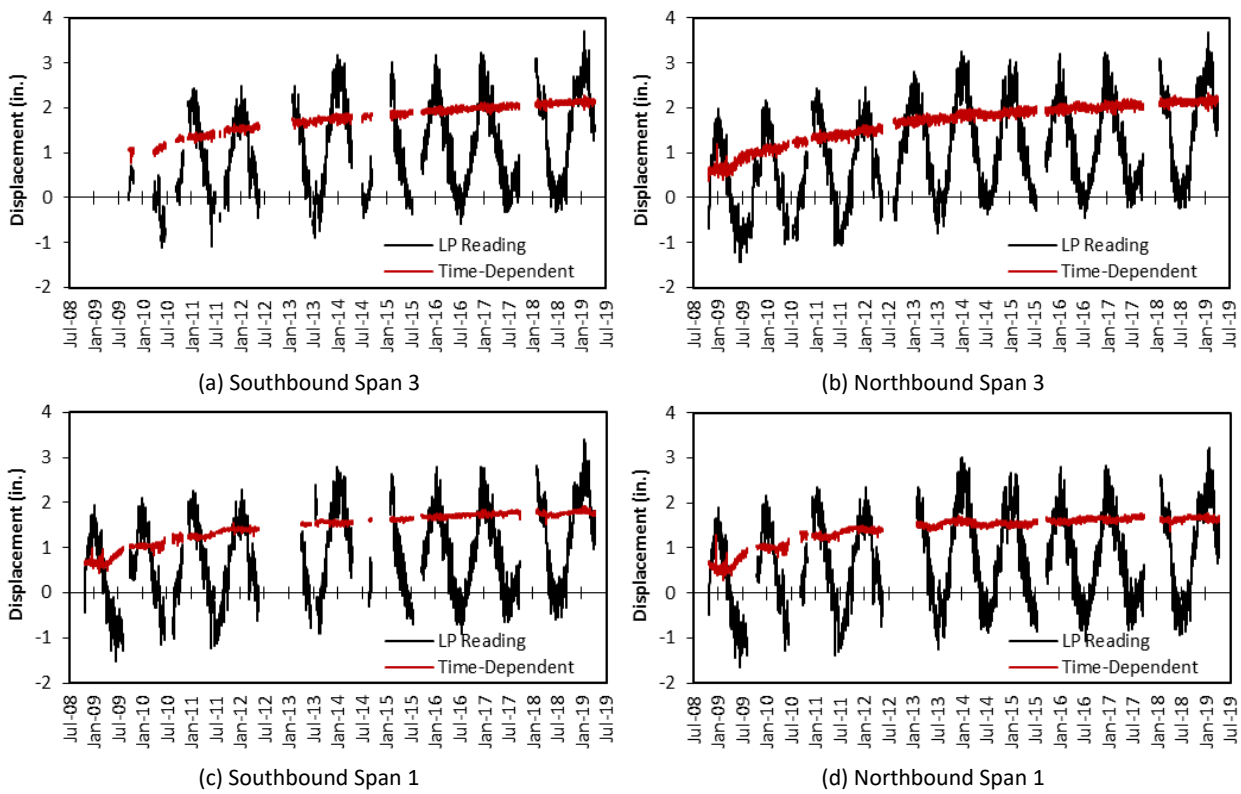

Figure 6.2: Measured and time-dependent LP displacements plotted with respect to unadjusted time.

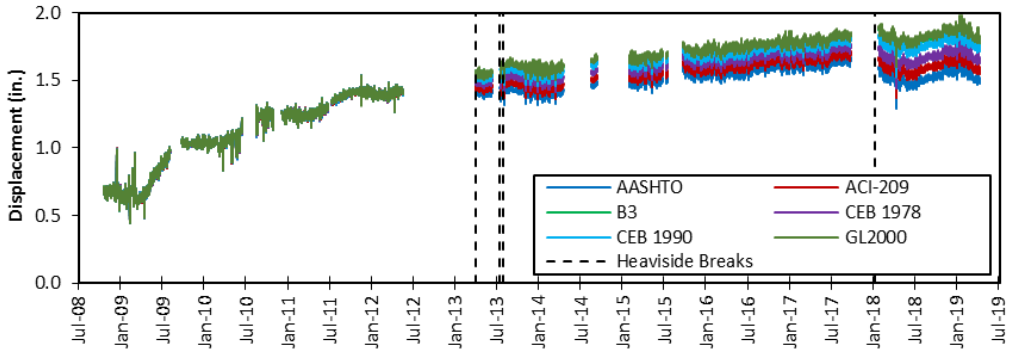

Figure 6.3: Southbound Span 1 time-dependent LP displacements for various assumed time-dependent models plotted with respect to unadjusted time.

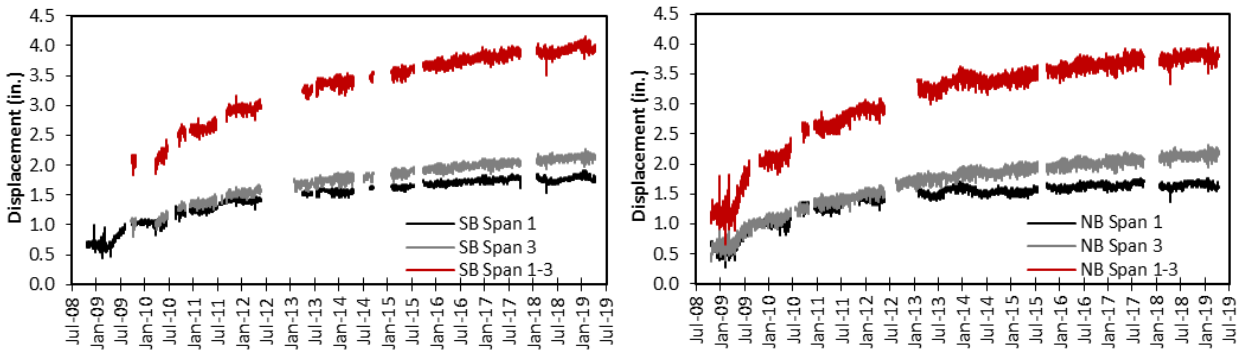

(a) Southbound Span 1 and Span 3

(b) Northbound Span 1 and Span 3

Figure 6.4: Time-dependent LP displacements plotted with respect to unadjusted time.

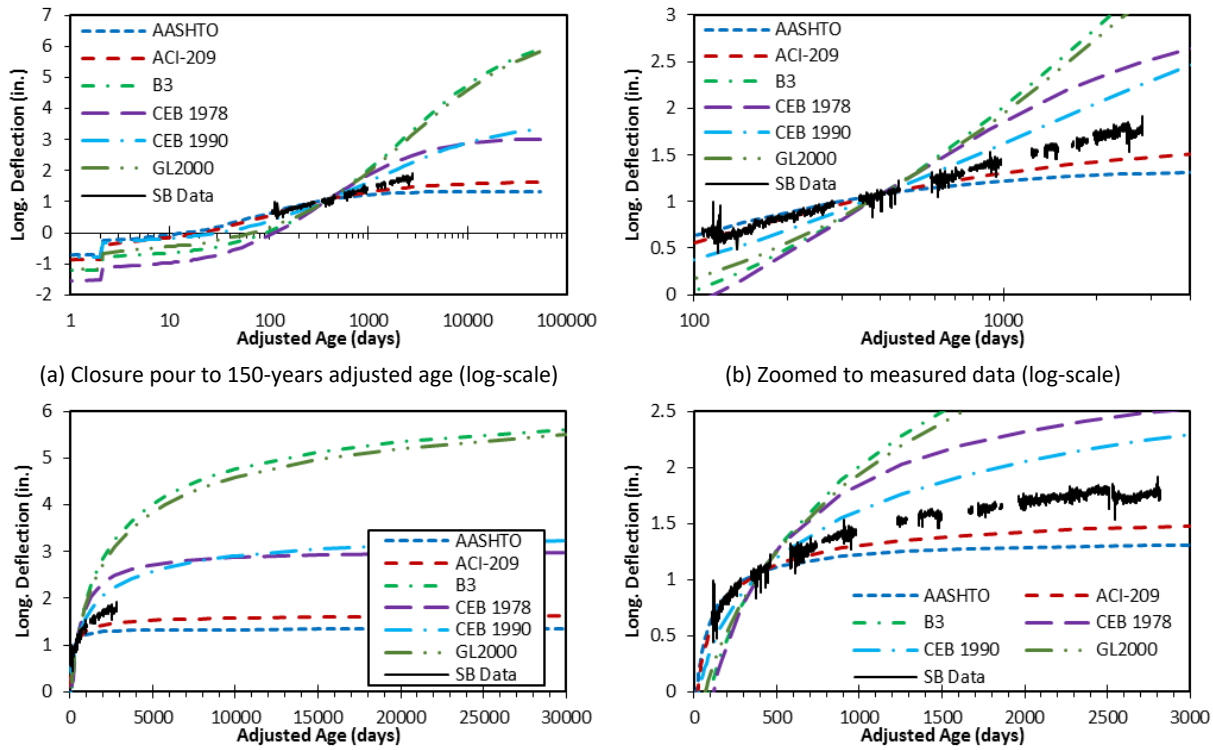

(a) Closure pour to 150-years adjusted age (log-scale)

(b) Zoomed to measured data (log-scale)

(c) Closure pour to 80-years adjusted age (linear scale)

(d) Zoomed to measured data (linear scale)

Figure 6.5: Comparison of estimated time-dependent longitudinal deflections with linear potentiometer data from southbound bridge Span 1.

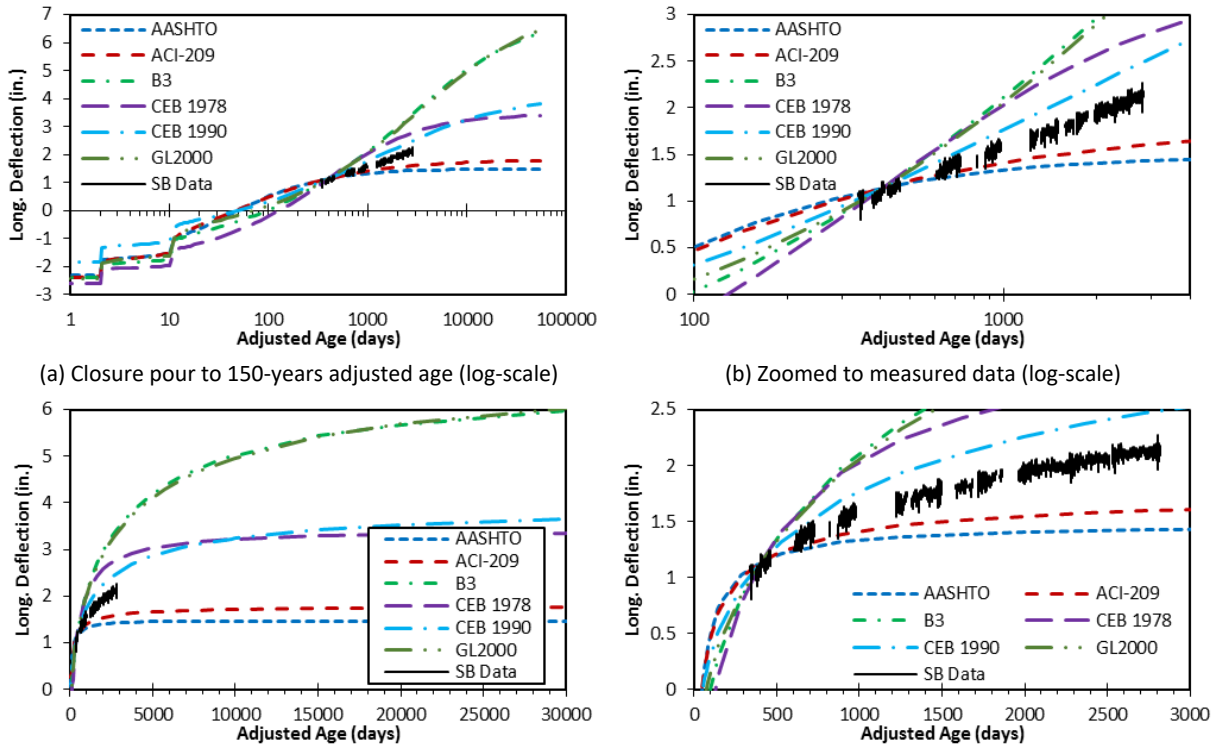

(a) Closure pour to 150-years adjusted age (log-scale)

(b) Zoomed to measured data (log-scale)

(c) Closure pour to 80-years adjusted age (linear scale)

(d) Zoomed to measured data (linear scale)

Figure 6.6: Comparison of estimated time-dependent longitudinal deflections with linear potentiometer data from southbound bridge Span 3.

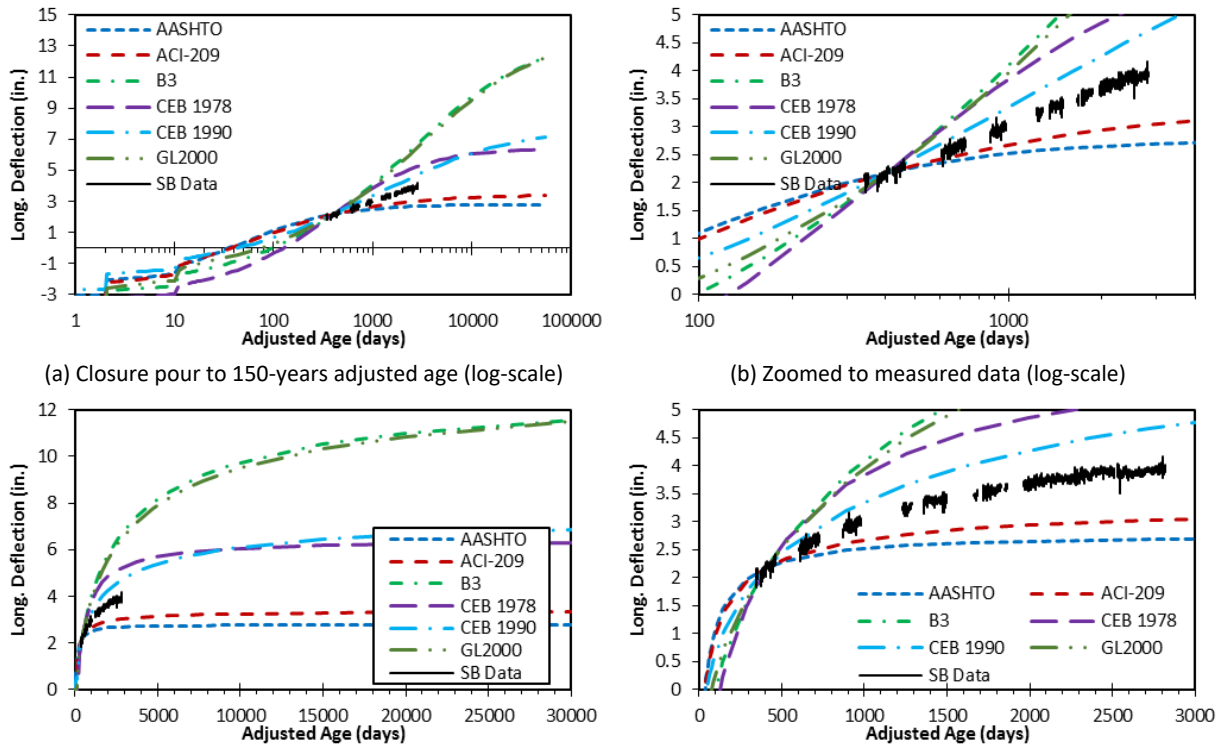

(a) Closure pour to 150-years adjusted age (log-scale)

(b) Zoomed to measured data (log-scale)

(c) Closure pour to 80-years adjusted age (linear scale)

(d) Zoomed to measured data (linear scale)

Figure 6.7: Comparison of estimated time-dependent longitudinal deflections with linear potentiometer data from southbound bridge combined Span 1 and Span 3.

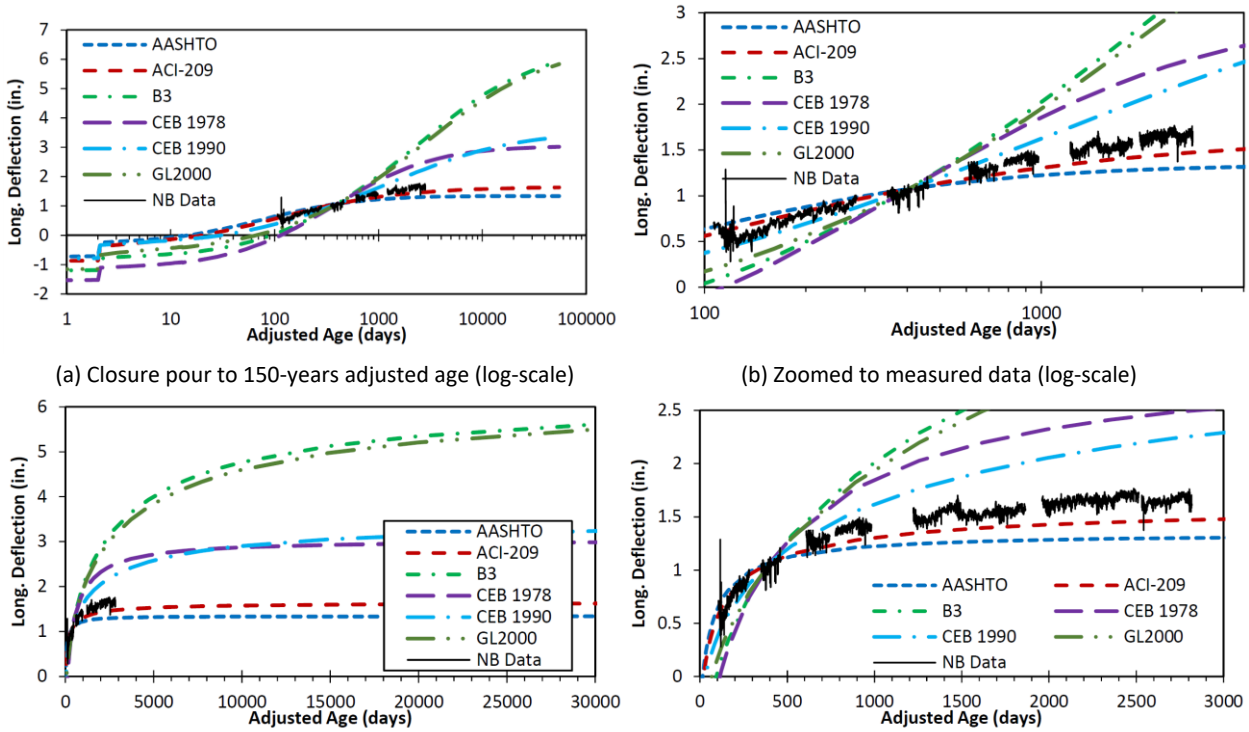

(a) Closure pour to 150-years adjusted age (log-scale)

(b) Zoomed to measured data (log-scale)

(c) Closure pour to 80-years adjusted age (linear scale)

(d) Zoomed to measured data (linear scale)

Figure 6.8: Comparison of estimated time-dependent longitudinal deflections with linear potentiometer data from northbound bridge Span 1.

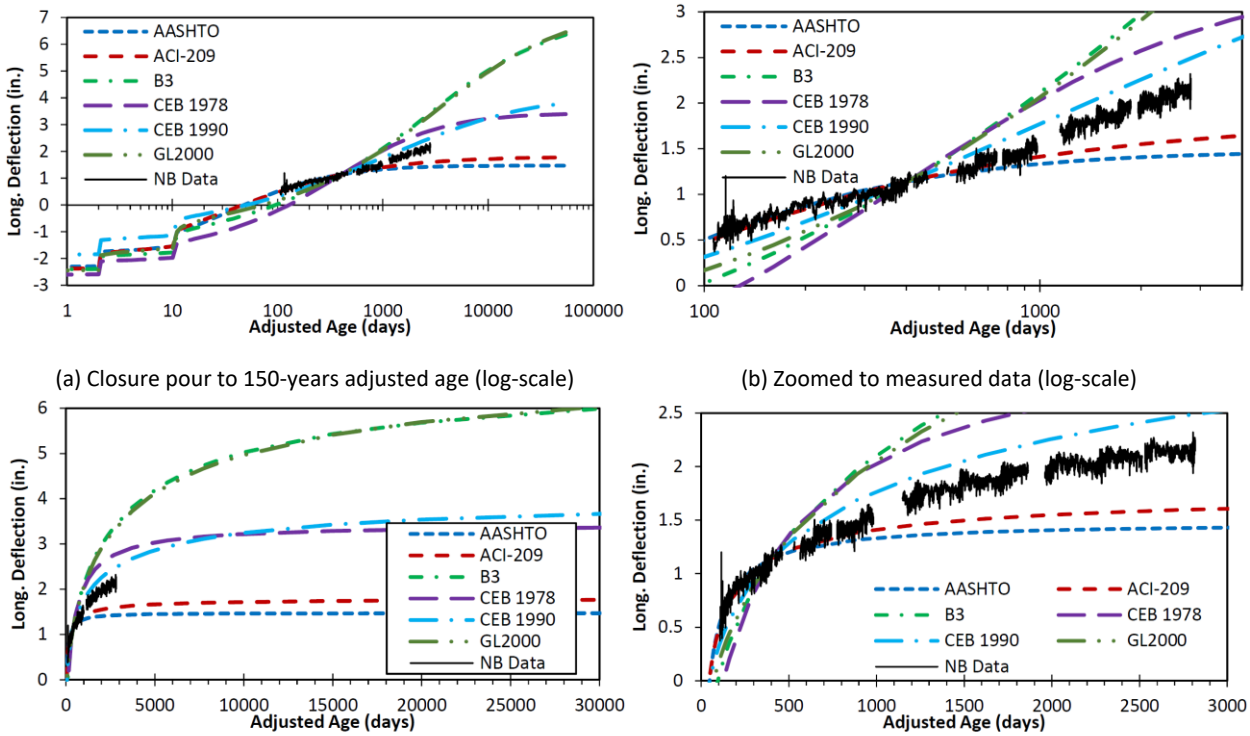

(a) Closure pour to 150-years adjusted age (log-scale)

(b) Zoomed to measured data (log-scale)

(c) Closure pour to 80-years adjusted age (linear scale)

(d) Zoomed to measured data (linear scale)

Figure 6.9: Comparison of estimated time-dependent longitudinal deflections with linear potentiometer data from northbound bridge Span 3.

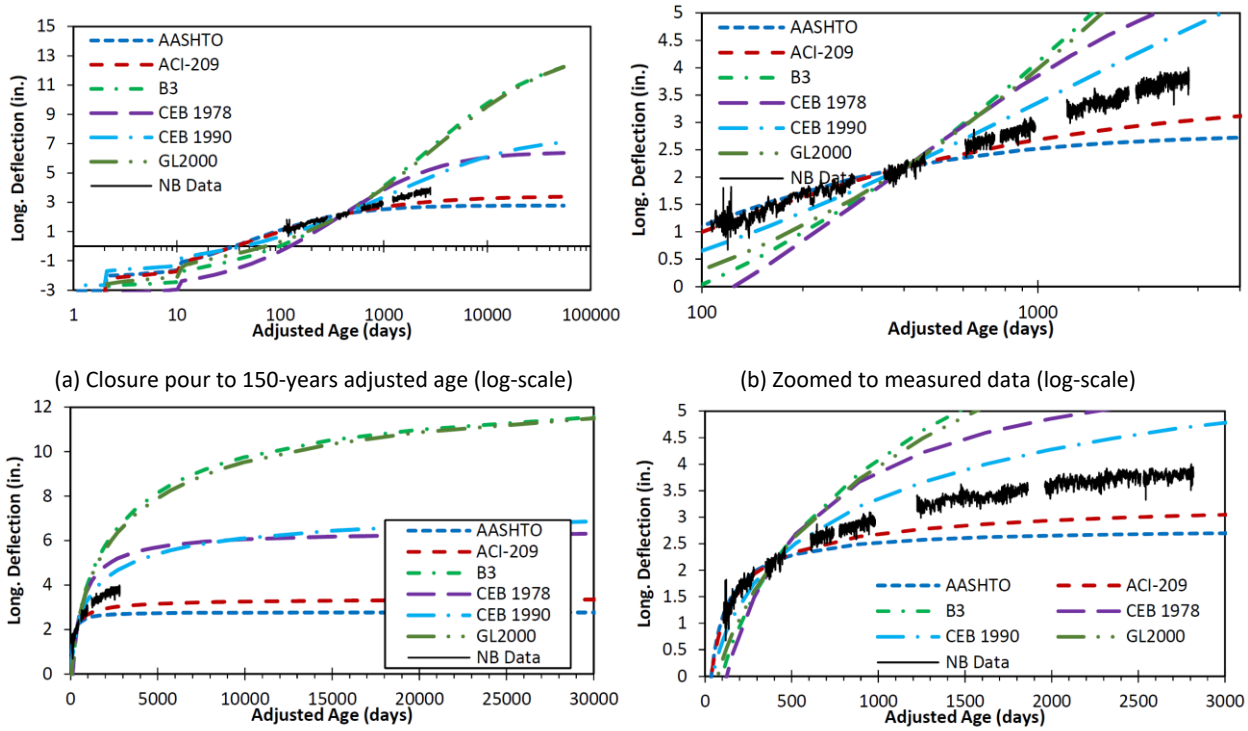

(a) Closure pour to 150-years adjusted age (log-scale)

(b) Zoomed to measured data (log-scale)

(c) Closure pour to 80-years adjusted age (linear scale)

(d) Zoomed to measured data (linear scale)

Figure 6.10: Comparison of estimated time-dependent longitudinal deflections with linear potentiometer data from northbound bridge combined Span 1 and Span 3.

6.2 TIME-DEPENDENT STRAINS

The linear regression procedure presented in French et al. (2014) was also used to extract time-dependent strains from the data collected by the vibrating wire strain gages (VWSGs). The time-dependent function in the linear regression was assumed to be the 1990 CEB/FIP Model Code FEM model prediction at the location nearest the sensor of interest. The linear regression was performed on the change in total strain readings for the period September 1, 2008 until October 6, 2018. The use of Heaviside functions in the regression was not necessary for the plotted VWSG data, as sensors were never reset or replaced. The resulting time-dependent strains from a selection of longitudinal gages in the southbound bridge are plotted with respect to the unadjusted time in Figure 6.11.

With the exception of the bottom flange strain gage installed at Location 5, all time-dependent strain estimates appeared to follow seasonal trends much like the linear potentiometer data. With respect to the data from the bottom flange of Location 5 located near Pier 2, it was likely that the aggregated temperature values taken exclusively from Location 7 in the southbound bridge did not accurately capture the behavior at this cross section. This may have been caused by the vastly different cross-sectional shape at Location 5 compared to Location 7, or was possibly due to the proximity of the gage to the boundary condition imposed by the bearing assemblies. The bottom flange strains from Locations

4, 6 and 8 (not plotted) showed similar limitations. For the strain gage data that was well-captured by the temperature at Location 7 of the southbound bridge and the linear regression procedure, the seasonal dependence of the time-dependent strain rates was clear.

With more than 5 additional years of data since time-dependent strains were analyzed in French et al. (2014), the coefficients for the linear regression performed on data through October 6, 2018 were different from the coefficients computed using regression only on data through July 19, 2013. Thus, the time-dependent strain results for data prior to July 19, 2013 differed slightly when performing the linear regression on the two different sized data sets. The effect of data set size on the time-dependent strain results are shown in Figure 6.12 for two VWSG positions at Location 7 of the southbound bridge. Time-dependent strain approximations using data through October 6, 2018 tended to contain larger daily strain variations than the time-dependent strain approximations resulting from the regression analysis performed on VWSG data up through July 19, 2013. Similar trends were observed for most gages at other locations as well. The temperature measurements used in the regression, taken exclusively from Location 7 in the southbound structure as representative of the average temperature in the entire bridge, likely introduced additional errors in the data processing given that the vibrating wire strain gages are primarily sensitive to local behavior. This sensitivity to local behavior is in contrast to the LPs, which are primarily sensitive to global bridge motion. While the daily variation of the time-dependent strains seemed to be a function of the length of the data set used for regression, the overall trend of the time-dependent strains remained the same no matter the duration of data used.

The time-dependent strains extracted from longitudinal vibrating wire strain gages at Locations 3, 5, 7, 8, and 9 from the southbound bridge were compared to results from the finite element analysis (French et al. 2014) for each considered time-dependent model, as shown in Figures 6.13 through 6.17. Processed time-dependent strains for each plot were taken as the average of all available gages of the designated location description. For example, “Top Flange (Centerline of Box)” results represent the average of all available longitudinal gages located in the top flange at the center of each box, while “Bottom Flange (Below Webs)” represents the average computed using all available gages located in the bottom flange below any of the four webs. Finite element results at the webs represented the average taken from all four webs, and the results at the box centerlines were averaged between both boxes. All results were plotted with respect to Arrhenius adjusted age, computed using the average superstructure temperature from Location 7 to adjust the time-scale. The FEM computed strains were set equal to the measured results at 6:00 AM CST on March 22, 2009 (adjusted age equal to 124 days, roughly corresponding to the beginning of the second thermal cycle to which the bridge was exposed) for comparison. For these plots, only relative strains were meaningful as initial strain measurements were not recorded.

Three subplots are presented for each area of the cross section in Figures 6.13 through 6.17. These subplots represent identical data, but are plotted on different horizontal axes to highlight different aspects of the measurements and predictions. The left subplot shows the measured and predicted data out to an adjusted age of 150 years on a log time-scale, and illustrates the differences in predicted behavior for the various time-dependent models. The center plot is identical to the left plot, but zoomed to the measured data. The right plot shows the same data with respect to a linear timescale axis, and

more closely resembles how time-dependent behavior in a controlled environment would typically be visualized.

Depending on the location, the time-dependent strains extracted from the VWSG data were best approximated by the ACI 209 and 1990 CEB/FIP Model Code models. The ACI 209 model provided the closest predictions at Location 3, bottom flange of Location 5, and Location 9. The 1990 CEB/FIP Model Code predictions were closest to the measured data in the top flange of Location 5, Location 7, and Location 8. Measured time-dependent strains after 10 years were typically underestimated by the AASHTO and ACI 209 models, and overestimated by the B3, 1978 CEB/FIP Model Code, 1990 CEB/FIP Model Code, and GL2000 models.

Aside from the measured time-dependent strains in the top flange of Location 5 (Figure 6.14a) or the centerline of the bottom flange of Location 7 (Figure 6.15d), none of the models accurately captured the strains over the full timeframe of measured data. Measured time-dependent strains at Location 3 (Figure 6.13) and Location 9 (Figure 6.17) were captured by the AASHTO and ACI 209 provisions until approximately 4 years (1000 adjusted age days) after construction of the bridge. However, both these time-dependent models approached their asymptotic limits prior to 5 years after bridge completion and were inconsistent with the long-term trends of the time-dependent strains extracted from the VWSG data. Because the midspan, Location 7, has the best temperature approximation, these time-dependent strains likely offer the strongest indication of the best time-dependent model to capture the behavior of the bridge. At location 7, the 1990 CEB/FIP Model code predictions were closest to the measured data.

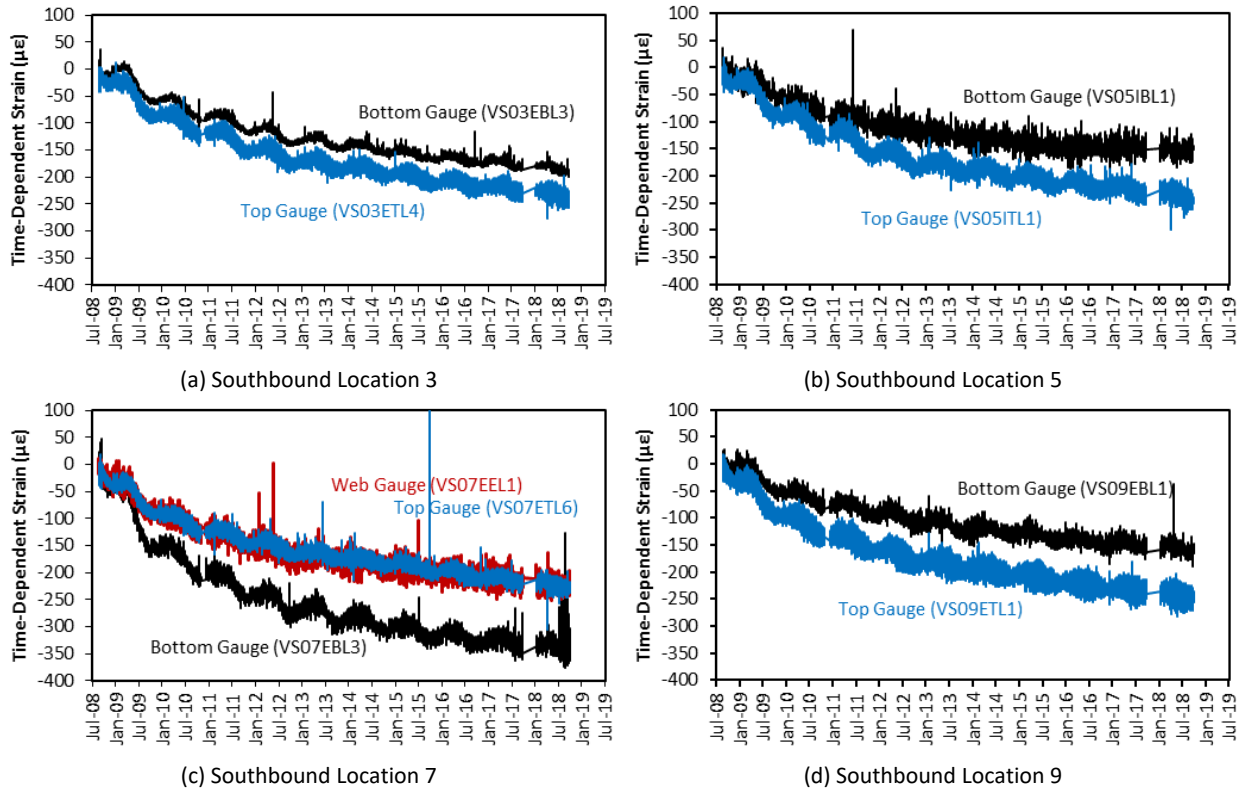

Figure 6.11: Time-dependent strains extracted from vibrating wire strain gage data by linear regression plotted with respect to unadjusted time.

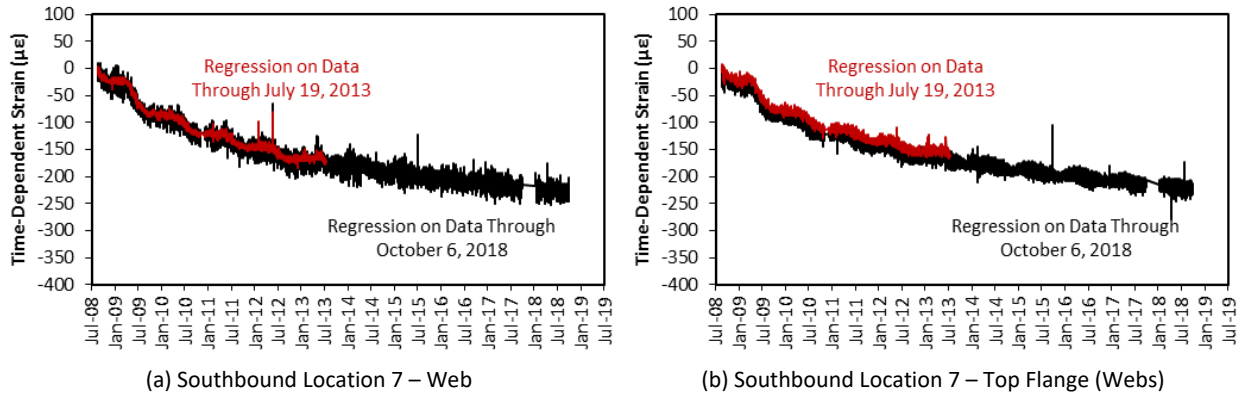

Figure 6.12: Time-dependent strains extracted from various size vibrating wire strain gage data sets plotted with respect to unadjusted time.

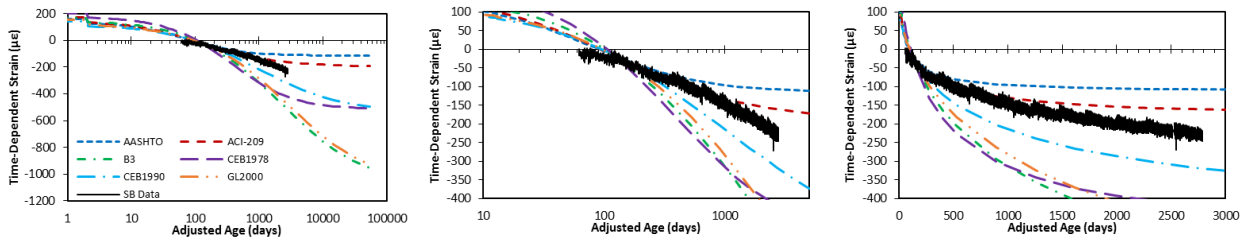

(a) Location 3 Top Flange (Above Webs):

Left - Closure to 150-years, Center - Zoomed to measured data, Right - Zoomed to measured data (linear scale)

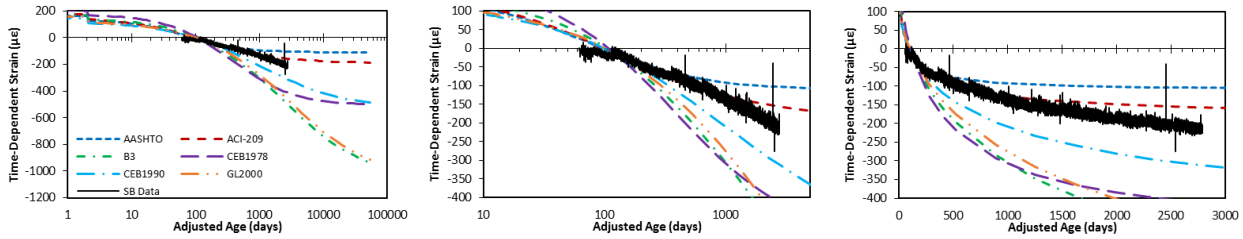

(b) Location 3 Top Flange (Centerline of Box):

Left - Closure to 150-years, Center - Zoomed to measured data, Right - Zoomed to measured data (linear scale)

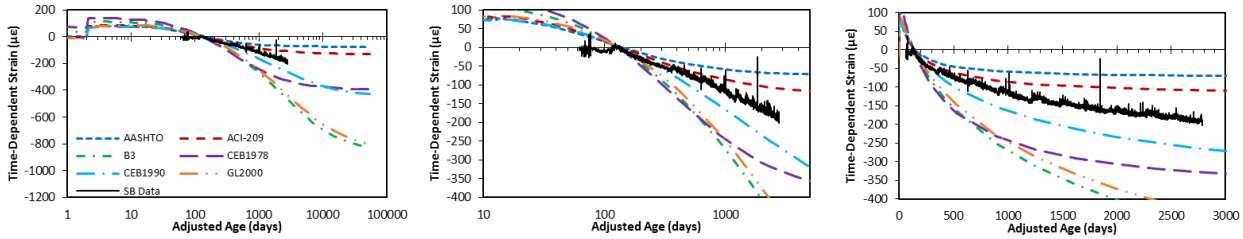

(c) Location 3 Bottom Flange (Above Webs):

Left - Closure to 150-years, Center - Zoomed to measured data, Right - Zoomed to measured data (linear scale)

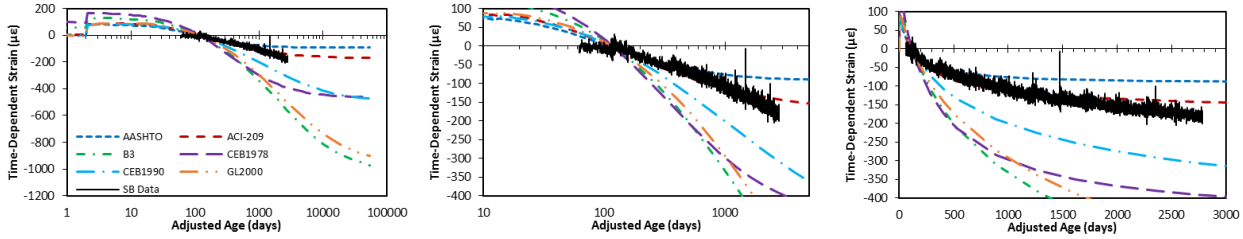

(d) Location 3 Bottom Flange (Centerline of Box):

Left - Closure to 150-years, Center - Zoomed to measured data, Right - Zoomed to measured data (linear scale)

Figure 6.13: Comparison of measured longitudinal time-dependent strains to those computed with FEM using all considered time-dependent models at Location 3 of southbound bridge.

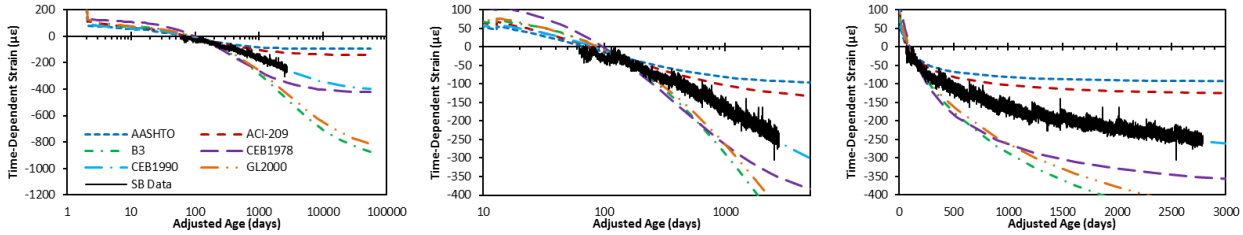

(a) Location 5 Top Flange (Centerline of Box):

Left - Closure to 150-years, Center - Zoomed to measured data, Right - Zoomed to measured data (linear scale)

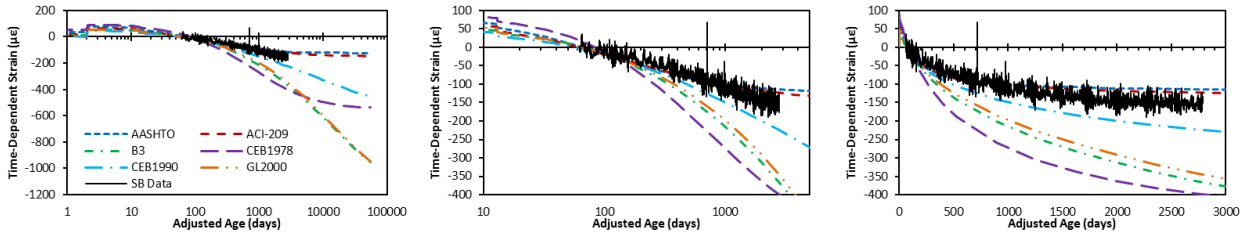

(b) Location 5 Bottom Flange (Centerline of Box):

Left - Closure to 150-years, Center - Zoomed to measured data, Right - Zoomed to measured data (linear scale)

Figure 6.14: Comparison of measured longitudinal time-dependent strains to those computed with FEM using all considered time-dependent models at Location 5 of southbound bridge.

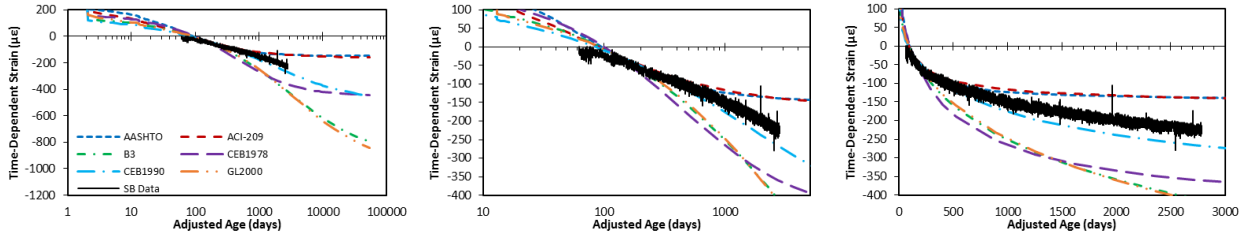

(a) Location 7 Top Flange (Above Webs):

Left - Closure to 150-years, Center - Zoomed to measured data, Right - Zoomed to measured data (linear scale)

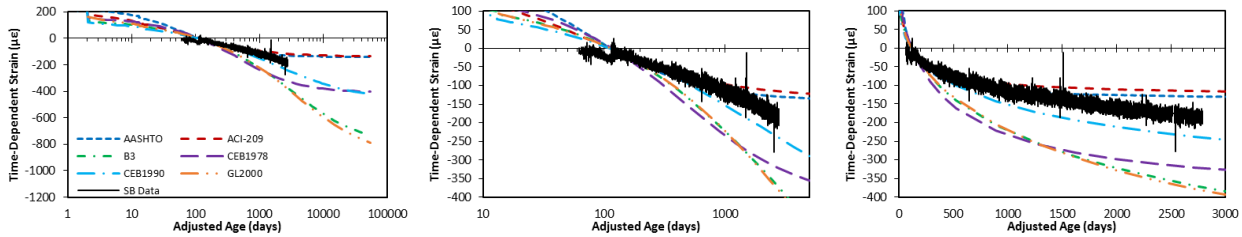

(b) Location 7 Top Flange (Centerline of Box):

Left - Closure to 150-years, Center - Zoomed to measured data, Right - Zoomed to measured data (linear scale)

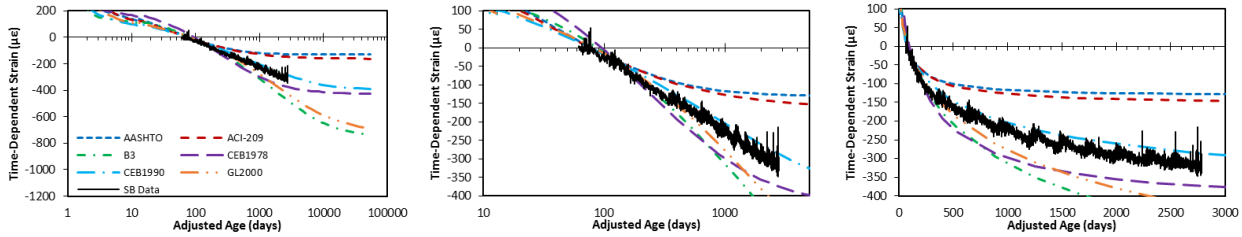

(c) Location 7 Bottom Flange (Above Webs):

Left - Closure to 150-years, Center - Zoomed to measured data, Right - Zoomed to measured data (linear scale)

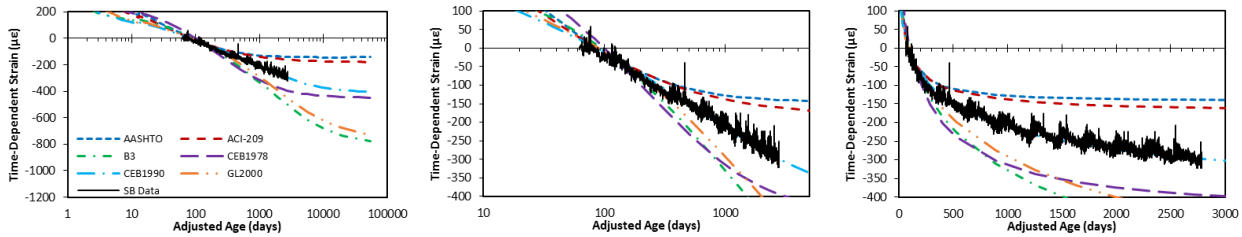

(d) Location 7 Bottom Flange (Centerline of Box):

Left - Closure to 150-years, Center - Zoomed to measured data, Right - Zoomed to measured data (linear scale)

Figure 6.15: Comparison of measured longitudinal time-dependent strains to those computed with FEM using all considered time-dependent models at Location 7 of southbound bridge.

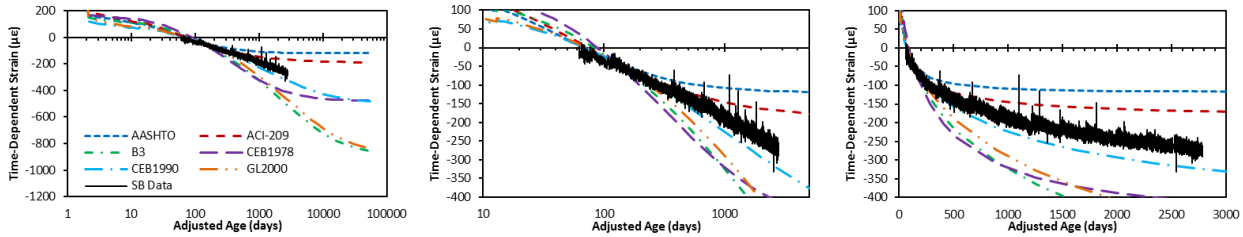

(a) Location 8 Top Flange (Centerline of Box):

Left - Closure to 150-years, Center - Zoomed to measured data, Right - Zoomed to measured data (linear scale)

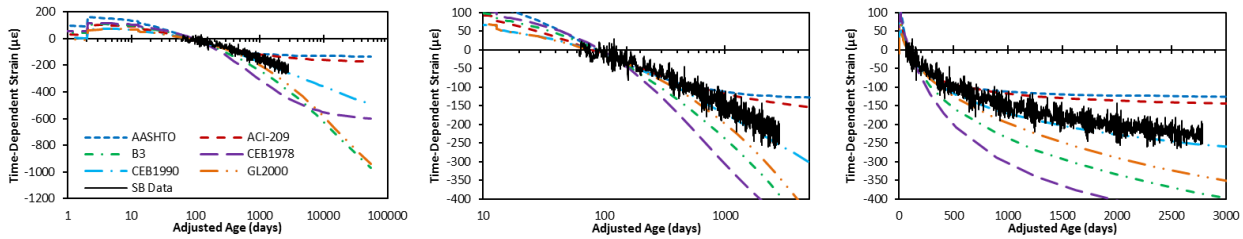

(b) Location 8 Bottom Flange (Centerline of Box):

Left - Closure to 150-years, Center - Zoomed to measured data, Right - Zoomed to measured data (linear scale)

Figure 6.16: Comparison of measured longitudinal time-dependent strains to those computed with FEM using all considered time-dependent models at Location 8 of southbound bridge.

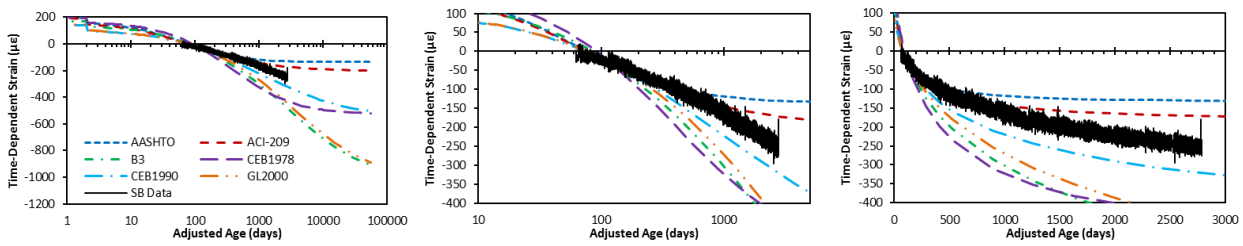

(a) Location 9 Top Flange (Centerline of Box):

Left - Closure to 150-years, Center - Zoomed to measured data, Right - Zoomed to measured data (linear scale)

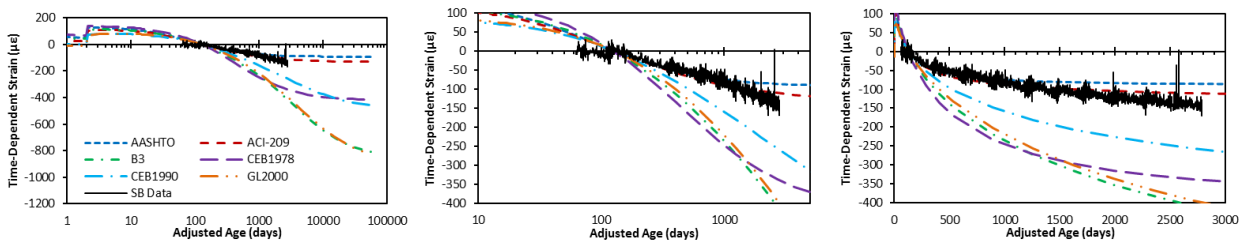

(b) Location 9 Bottom Flange (Centerline of Box):

Left - Closure to 150-years, Center - Zoomed to measured data, Right - Zoomed to measured data (linear scale)

Figure 6.17: Comparison of measured longitudinal time-dependent strains to those computed with FEM using all considered time-dependent models at Location 9 of southbound bridge.

6.3 CONCLUSION

The time-dependent behavior of the I-35W Saint Anthony Falls Bridge was extracted from measured linear potentiometer and vibrating wire strain gage data, which contain both time- and temperature-related deformations. Similar time-dependent longitudinal displacements were measured on the northbound and southbound structures. The time-dependent response of the southbound structure was compared to predicted behavior based on several time-dependent models applied to the finite element model of the bridge. Depending on the location, the measured time-dependent behavior extracted from the linear potentiometers and vibrating wire strain gages was best approximated by the ACI 209 and 1990 CEB/FIP Model Code models. The ACI 209 model typically underestimated and the 1990 CEB/FIP Model Code typically overestimated the time-dependent behavior.

CHAPTER 7: SERVICE LOAD STRESSES

In addition to strength design considerations, service load combinations are utilized to prevent performance issues such as cracking. Cracks on concrete bridges can allow water and salt to reach the reinforcement, possibly leading to steel corrosion. Over a long period of time, these serviceability issues can affect the lifespan, maintenance requirements, and safety of the bridge.

Due to the large magnitude of the observed temperature gradients, the maximum service load stresses on the bridge could be impacted. The modeled thermal gradient stresses (Chapter 5) are considered in combination with time-dependent stress losses (Chapter 6), and applied load stresses to evaluate the potential for cracking.

7.1 SERVICE LOADS

Temperature effects are considered in AASHTO LRFD Bridge Design Specifications (2017) load combinations as uniform temperature force effects (TU) and temperature gradients force effects (TG). As temperature effects are not considered for strength, the load combinations of interest are Service I and Service III.

$$Service\ I: DL + PS + CR + SH + LL + TU + \gamma_{TG} * TG \tag{7-1}$$

$$Service\ III: DL + PS + CR + SH + 0.8 * LL + TU + \gamma_{TG} * TG \tag{7-2}$$

AASHTO LRFD (2017) article 3.4.1 states that the load factor for temperature gradient, γ_{TG}, should be determined based on the type of structure and the limit state being investigated on a project-specific basis. When project-specific information is unavailable, AASHTO LRFD (2017) allows γ_{TG} to be taken as:

- 0.0 at the strength and extreme event limit states
- 0.5 at the service limit state when live load is considered
- 1.0 at the service limit state when live load is not considered

Therefore, from (7-1) and (7-2), three equations are obtained using the different load factors for temperature gradients. Equation (7-5) is the case of no live load and full temperature gradient, henceforth referred to as Service I or III.

$$Service\ I: DL + PS + CR + SH + LL + TU + 0.5 * TG \tag{7-3}$$

$$Service\ III: DL + PS + CR + SH + 0.8 * LL + TU + 0.5 * TG \tag{7-4}$$

$$Service\ I\ or\ III: DL + PS + CR + SH + TU + 1 * TG \tag{7-5}$$

The main concern for service is cracking of the concrete by reaching the tensile stress limit. It was determined that at the midspan of the river span, Service I would control tension in the bottom flange due to the positive temperature gradient effects, and Service I or III would control tension in the top flange due to the negative temperature gradient effects. The service load stresses addressed in this chapter were only calculated at the midspan of the river span of the bridge; however, cracking could be

a concern at other locations, particularly in the deck over the piers. Due to limited knowledge of the thermal stress distributions in the pier regions, the controlling service load cases were not determined.

7.2 STRESS RESULTS

In this section, the design service load stresses are compared with the service load stresses that are likely occurring or are possible at the midspan of the river span. The service load stresses at the midspan of the river span of the bridge (location 7 in Figure 3.1) were found for each combination of applied temperature gradient (Chapter 5) and time-dependent model (Chapter 6). Focus was placed on the midspan of the river span because the large number of thermistors at that location allowed for greater confidence in the measured gradients.

Within Service I, the load cases of interest for tension in the bottom flange due to the positive thermal gradient at the midspan of the bridge are plotted in **Error! Reference source not found.** and enumerated in Table 7.1. In **Error! Reference source not found.**, each cluster reflects a different design gradient and time-dependent model stress combination. The two thermal gradients explored were AASHTO LRFD (2017) and Priestly-Z2, and the three time-dependent models were AASHTO LRFD (2017), CEB 1978, and CEB 1990. The AASHTO thermal gradient in **Error! Reference source not found.** represents the design gradient, while the Priestly-Z2 represents the maximum measured gradient (see 5.3.2). As stresses due to the time-dependent model change with time, the stresses were determined at end of service life, which would represent the worst case.

In Figure 7.1, the gradient is identified to the right of the cluster, while the time-dependent model is identified to the left of the cluster. Within each cluster, the stress contribution from each component of the service load combination is plotted with the patterned bars and the total stress is indicated by the uppermost solid bar. The top three clusters represent different possible designs using the AASHTO LRFD (2017) positive temperature gradient; of those, the second cluster represents the bridge design stresses. As the positive gradient was shown to closely follow the Preistley-Z2 curve and the time-dependent behavior was best approximated by 1990 CEB/FIP, the last cluster represents the service stresses that the bridge will likely see.

In the case of the I-35W Saint Anthony Falls Bridge, the bottom flange for precast sections (located at the midspan) was designed for zero tension. For this bridge, the stresses that will likely occur and the stresses that it was designed for are very similar. However, if the bridge had been designed with the AASHTO LRFD (2017) time dependent model the bridge stresses would have been quite a bit higher than the stresses assumed in design. In a case where a bridge was designed right up to the tensile limit with the AASHTO LRFD (2017) temperature gradient, it is quite possible that the realized stresses could cause cracking.

When considering tension in the top flange, combinations of stresses due to the numerous measured and design negative temperature gradients (Section 5.3) and due to the different time-dependent models (Chapter 6) were explored. As shown in Section 5.2.2, the measured negative thermal gradients did not match the design gradients shape; therefore, four measured negative gradients were

considered. Each represents a different simplification of the negative gradient temperature profile measured in the structure. The load cases of interest for the tension in the top flange due to the negative thermal gradients at the midspan of the river span for service load combination I or III are shown in Figure 7.2 and enumerated in Table 7.2. The figure shows the effects of using the different temperature gradients (AASHTO LRFD (2017), Measured 1 Negative, and NZ-Z2) in combination with the AASHTO LRFD (2017), CEB 1978, and CEB 1990 time-dependent models on the service load stresses. AASHTO LRFD (2017) and NZ-Z2 were used as the design gradients. Of the measured negative temperature profiles, Measured 1 Negative was chosen as a case of interest as it produced the largest amount of tensile stress (Section 5.3.3). Measured 1 was a simplification of the negative temperature profile measured in the southbound bridge at 6:00 AM CST on March 11, 2009. When calculating the gradient thermal stresses due to the Measured 1 Negative temperature profile, the parabolic fit of Equation 5-1 was applied along the entire length of the bridge from the top surface down to a depth of 12.11 in. below the top surface, with zero thermal gradients elsewhere.

In Figure 7.2, the first two, fourth, and last cluster represent the various design options; the second cluster represents the case for which the bridge was designed. The fifth cluster represents what is likely to occur on the bridge based on current trends. The I-35W Saint Anthony Falls Bridge was designed to a top flange tensile limit of -250 psi. This limit is to avoid cracking on the deck of the bridge. Based on the load case stress results shown in Figure 7.2, the stresses that are most likely to occur on the bridge are just lower than the stress limit used in designed. This means that the design cases are not truly reflecting the stresses likely occurring on the bridge at the end of its service life.

An important aspect of the negative gradient controlling load combination, Service I or III, is that the maximum negative thermal gradient occurs between 5:00 AM and 8:00 AM. During this time there is likely live loading from truck traffic across the bridge. This means that while the bridge is experiencing maximum stresses due to temperature, it could also be experiencing large stresses due to live load. It is possible that the stress due to live load could put the design further beyond the tensile limit. This is concerning, because it is more likely that cracking will occur in the deck, which can lead to serviceability issues.

Under negative thermal gradients and live loading, service load stresses in the deck over the piers could be of particular concern. However, the four applied measured negative gradients considered in Section 5.3.3 resulted in significantly different stresses in the pier region. Because the thermal gradient shapes near the piers, especially the bottom tail, was relatively unknown, service stress values likely to occur in these regions were not calculated.

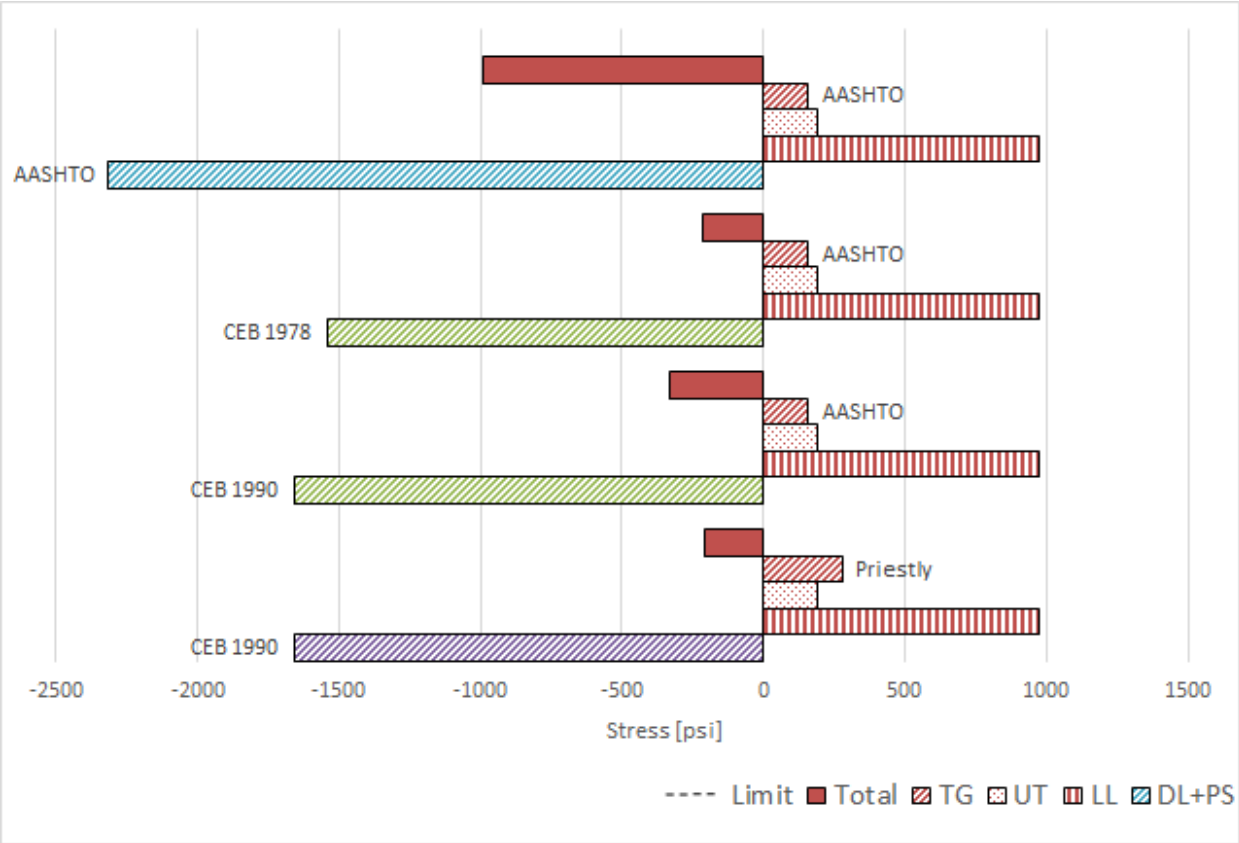

Figure 7.1: Tensile stress in the bottom flange at midspan due to positive thermal gradient, service load combination I

Table 7.1: Tensile stress in bottom flange at midspan due to positive thermal gradient, service load combination I

Creep Model	DL+PS	LL	UT	Temp Gradient	TG	Total	Tensile Limit	
CEB 1990	-1657	973	194	**Priestly**	282	-208	0	Possible
				AASHTO	158	-332		Design
CEB 1978	-1539	973	194	**AASHTO**	158	-215	0	Design
AASHTO	-2314	973	194	**AASHTO**	158	-990	0	Design

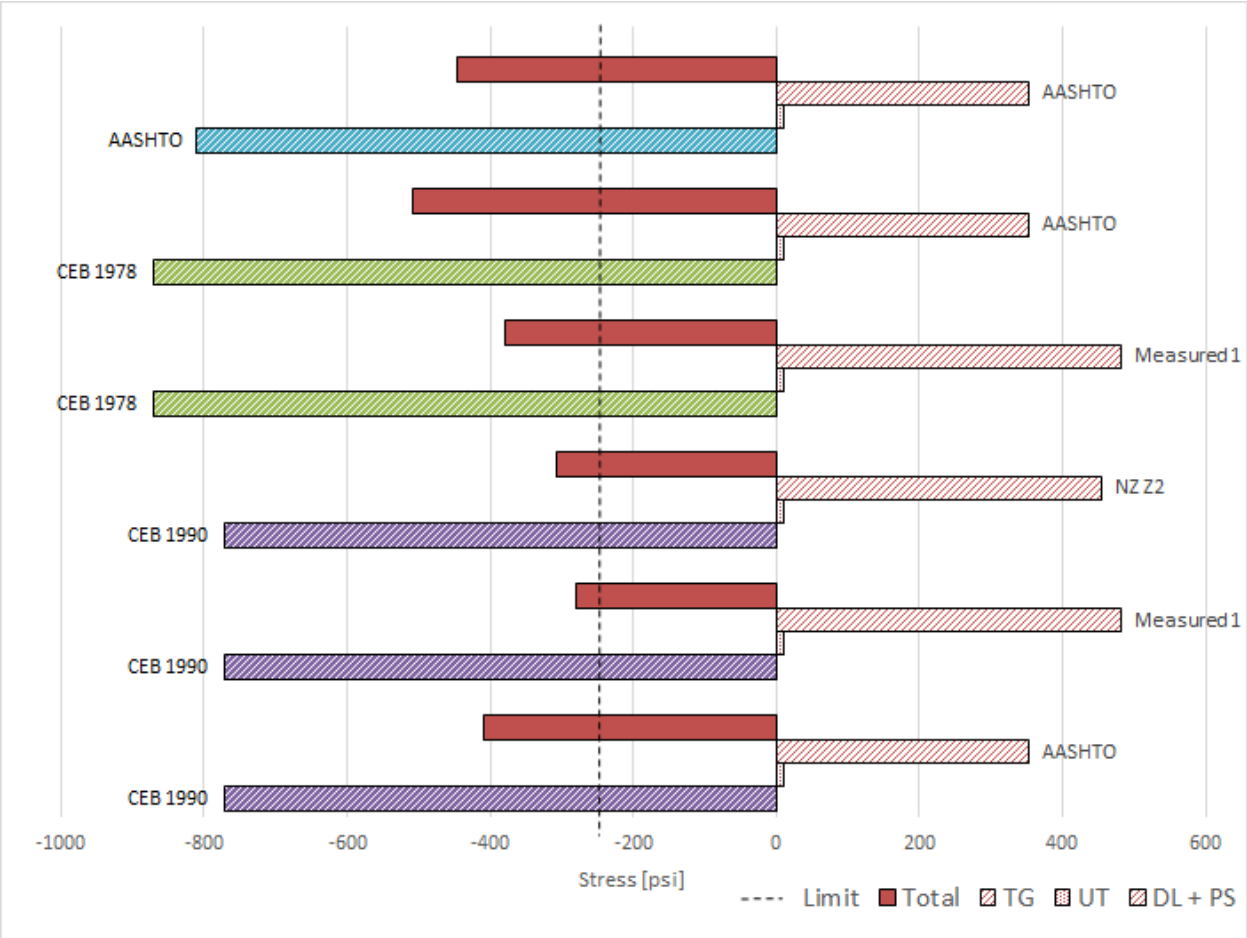

Figure 7.2: Tensile stress in the top flange at midspan due to negative thermal gradient, service load combination I or III

Table 7.2: Tensile stress in top flange at midspan due to negative thermal gradient, service load combination I or III

Creep Model	DL+PS	LL	UT	Temp Gradient	TG	Total	Tensile Limit	
CEB 1990	-772	0	10	**AASHTO**	353	-409	-250	Design
				Measured 1	483	-279		Possible
				NZ Z2	455	-308		Possible
CEB 1978	-870	0	10	**Measured 1**	483	-378	-250	Possible
				AASHTO	353	-508		Design
AASHTO	-810	0	10	**AASHTO**	353	-447	-250	Design

7.3 SERVICE LOAD STRESS CONCLUSIONS

For future designs in Minnesota, it is recommended that the Priestley fifth order curve scaled to AASHTO LRFD (2017) Zone 2 top temperature be used in combination with the CEB/FIP 1990 model to better represent the positive thermal stress effects. For the negative thermal design, it is recommended

to use the NZ-Z2 gradient with the CEB/1990 in order to achieve a more accurate representation of the stresses in the deck given the limited knowledge of the negative gradient profile along the bridge length.

To achieve a more accurate and complete representation of the stresses that are likely to occur at all locations in the bridge, more research is recommended in several areas. First, more research needs to be done on the shape of the negative temperature gradient in Minnesota. This would provide more information on the stresses likely to occur on the bridge. Another area that needs more research, is the temperature gradient above the piers. Additional temperature instrumentation above the piers would allow stress levels for cracking alone the entire length of the bridge to be considered rather than just at the midspan of the river span.

CHAPTER 8: CONCLUSIONS AND RECOMMENDATIONS

8.1 SUMMARY AND CONCLUSIONS

The I-35W St. Anthony Falls Bridge was instrumented with more than 500 sensors to capture structural behavior and evaluate the effectiveness of different monitoring strategies. The sensor performance over the ten-year period was investigated and the associated successes and challenges were outlined. In particular, the effectiveness of different strain measurement techniques and sensor distribution were addressed. Previous investigations of temperature-dependent and time-dependent behavior were expanded with the larger data set to better understand the behavior of post-tensioned concrete box girder structures with the potential to impact future designs.

The instrumentation deployed on the bridge to investigate the structural behavior included vibrating wire strain gages (VWSGs), thermistors, fiber optic sensors (SOFO), resistance strain gages, linear potentiometers, accelerometers, and corrosion monitoring sensors. These sensors were grouped into four measurement systems based on the acquisition approach for analysis: static system, dynamic system, fiber optic (SOFO), and corrosion monitoring system. Overall, the instrumentation survival rate of approximately 90% over the ten years was significant given the deployment duration, embedment of gages, and variety of sensor systems.

The measurement systems were leveraged in different ways throughout the monitoring process. The static, dynamic, and SOFO instrumentation systems have helped calibrate the FEM model used for behavior comparisons and to validate assumptions. For long-term monitoring, the temperatures measured on the static system and LP displacements on the dynamic system have provided the most valuable information regarding time-dependent effects and expected behavior. The corrosion monitoring system was never fully operational and interpretation of the data proved impossible.

Strain measurements captured by both the vibrating wire strain gages and SOFO fiber optic strain gages were compared over the ten-year period with a focus on gage sensitivity to temperature and time-dependent strains. The relative mechanical strains plus creep and shrinkage strains at the top and bottom flange were considered for each location along the length of the bridge. Compared to the vibrating wire strain gage mechanical strains, the SOFO mechanical strains contained higher error. This error was due to uncertainty in the concrete thermal expansion correction, which required the use of temperatures that were not measured directly at the SOFO gages. These temperatures may not have accurately reflected the concrete temperature at the location of the SOFO gage, and thus provided incorrect correction for the thermal strains.

Thermal gradients were extracted from the temperature data measured along the southbound structure. The heavily instrumented midspan location allowed for comparison of the gradient shapes along the depth of the section. The additional seven years of data emphasized that the New Zealand design gradients scaled to AASHTO Zone 2 most effectively captured the temperature behavior in both gradient shape and magnitude. The thermal gradients, both measured and design, were applied to the previously developed 2D FEM model to quantify the corresponding temperature stress demands along

the length. The large thermal stresses could be significant for serviceability considerations, particularly cracking of the deck in negative moment areas.

The time-dependent behavior of the I-35W Bridge was extracted from the measured linear potentiometer and vibrating wire strain gage data, which contained both time- and temperature-related deformations. The time-dependent response of the southbound structure was compared to predicted behavior based on several time-dependent models applied to the finite element model of the bridge. Depending on the location, the measured time-dependent behavior extracted from the linear potentiometers and vibrating wire strain gages was best approximated by the ACI 209 and 1990 CEB/FIP code models. The measured data were conservative with respect to the 1978 CEB/FIP Model code used in the bridge design.

8.2 EVALUATION AND RECOMMENDATIONS FOR INSTRUMENTATION

The measurements collected over the ten years of monitoring, with the aid of material tests, truck tests, and finite element modeling, provided insight regarding the relative strengths of the instrumentation systems and potential considerations for future deployments. When establishing the sampling rate of the measurements, there was a tradeoff between granularity and data quantity. For capturing thermal gradients, sampling the static system hourly provided adequate insight to the magnitude and variation of the thermal behavior. The sampling rate of the dynamic system balanced improved filtering performance, frequency resolution, and data quantity.

The temperature loading and response of the structure was determined to be essential to understanding structural behavior; as a result, the thermistors, vibrating wire strain gages, and bearing displacements were considered the most important for long-term monitoring of these stiff concrete structures. However, leveraging one heavily instrumented cross-section to capture the temperature distribution throughout the structure limited the ability to interpret structural behavior near the piers, where the cross section varied significantly. Additional cross sections with temperature measurements would have provided a more accurate representation of the temperature distribution throughout the structure. In addition, the density of temperature measurements through the cross-section, while helpful, was not required for capturing the temperature gradient effects for long-term monitoring. Therefore, fewer temperature sensors could be distributed at additional cross-sections. This could be essential as the temperature-dependent behavior starts to dominate the system's response over initial creep and shrinkage.

The currently deployed long-term monitoring system compares the measured time-dependent deformations with predicted behavior as part of both short term and long-term behavior checks. As the time-dependent effects slow down, the temperature-dependent behavior will start to dominate the behavior. The correction for the temperature behavior will be important for an effective and reliable monitoring system.

In addition, for future implementation of SOFO gages, it is recommended that, at a minimum, a temperature gage be installed directly below the concrete surface at the center of each SOFO gage. This

will minimize error in the calculation of the concrete thermal expansion correction of the measured total strains. Depending on the longitudinal temperature variation in the cross section over the length of the SOFO gage, more embedded temperature gages may be necessary to accurately capture the internal concrete temperature.

While the SOFO measurements compliment the VWSGs for estimation of creep and shrinkage strains and curvature calculations, the additional measurement type and longer gage length may not compensate for the higher deployment cost. The SOFO and thermistor systems use different acquisition systems, which makes merging the data challenging. Mechanical strains cannot be computed unless data is available from both the static and SOFO systems.

In future monitoring system deployments, several considerations during design and installation will improve performance and the evaluative power of the data. The electrical grounding and ease of power cycling should be carefully considered in the system design to limit outages and associated downtime due to electrical storms. Having researchers on site during sensor installation will limit errors due to location uncertainty and labeling. In addition, researchers should be on site for initial measurements to ensure that complete data is captured, which would then allow for absolute strains to be determined, instead of just changes in strain.

8.3 EVALUATION AND RECOMMENDATIONS FOR DESIGN

The seasonal and daily temperature variations have a significant impact on the bridge's behavior. The longitudinal strains along the length of the bridge highlighted the daily strain variations, which were significant, particularly along the top flange; for example, the daily variation at midspan was on the order of 100 $\mu\varepsilon$. Furthermore, the temperature-dependent behavior was clearly evident in the long-term longitudinal deflections of the bridge and required a compensation approach to extract the time-dependent behavior.

The maximum positive and negative gradients regularly exceed the AASHTO design specifications and are most effectively captured by the Priestley and New Zealand design gradients scaled to the Zone 2 temperature region. These New Zealand design gradients produce larger temperature stress demands than the AASHTO design gradients along the length of the bridge. Of particular interest is the negative thermal gradients, which could be a concern for serviceability of the deck. The shape of the negative gradient, particularly the bottom tail, could have a significant effect on the resulting thermal stresses. As the maximum gradients occur during rush hour traffic, the effect of the thermal stresses may be of concern for potential cracking. While the design assumptions for the I-35W Bridge appear to limit the potential for cracking of the deck under negative gradients, the large thermal stresses could be significant for serviceability considerations in other bridge structures.

Assessment of the time-dependent behavior through the ten-year deployment showed that the 1990 CEB/FIP Model Code and ACI-209 models best predicted the in-situ creep and shrinkage behavior. Typically, the ACI 209 model underestimated and the 1990 CEB/FIP Model Code overestimated the time-dependent behavior. Because the midspan, Location 7, had the best measured temperature

information, these time-dependent strains likely offered the strongest indication of the best time-dependent model to capture the behavior of the bridge. At location 7, the 1990 CEB/FIP Model code predictions were closest to the measured data. There were no long-term concerns with excessive deflections.

REFERENCES

American Association of State Highway and Transportation Officials. (1994). *AASHTO LRFD Bridge Design Specifications* (First Edition). Washington, D.C.: AASHTO.

American Association of State Highway and Transportation Officials. (1998). *Guide Specifications for Design and Construction of Segmental Concrete Bridges* (Proposed Second Edition). Washington, D.C.: AASHTO.

American Association of State Highway and Transportation Officials. (2010). *AASHTO LRFD Bridge Design Specifications* (Fifth Edition). Washington, D.C.: AASHTO.

American Association of State Highway and Transportation Officials. (2017). *AASHTO LRFD Bridge Design Specifications* (Eighth Edition). Washington, D.C.: AASHTO.

Brown, R., Gaebler, K., Shield, C., & Linderman, L. (2019). *Displacement Monitoring of I-35W Bridge with Current Vibration-Based System* (Report MN/RC 2019-05). St. Paul, MN: Minnesota Department of Transportation.

Collins, J., Mullins, G., Lewis, C., & Winters, D. (2014). *State of the Practice and Art of Structural Health Monitoring of Bridge Substructures* (No. FHWA-HRT-09-040). Washington, D.C.: Federal Highway Administration, Office of Infrastructure Research and Development.

French, C. E. W., Shield, C. K., & Hedegaard, B. D. (2014). *Modeling and Monitoring the Long-Term Behavior of Post-Tensioned Concrete Bridges* (Report MN/RC 2014-39). St. Paul, MN: Minnesota Department of Transportation.

French, C. E. W., Shield, C. K., Stolarski, H. K., Hedegaard, B. D., & Jilk, B. J. (2012). *Instrumentation, Monitoring, and Modeling of the I-35W Bridge* (MN/RC 2012-24). St. Paul, MN: Minnesota Department of Transportation.

Hedegaard, B. D., French, C. E. W., & Shield, C. K. (2013). Investigation of Thermal Gradient Effects in the I-35W St. Anthony Falls Bridge. *Journal of Bridge Engineering*, *18*(9), 890–900.

Imbsen, R. A., Vancershaf, D. E., Schamber, R. A., & Nutt, R. V. (1985). *Thermal Effects In Concrete Bridge Superstructures* (National Cooperative Highway Research Program Report 276). Washington, D.C.: National Cooperative Highway Research Program.

New Zealand Transport Agency. (2018). *New Zealand Bridge Manual*. Wellington, NZ: New Zealand Transport Agency.

Potgieter, I. C., & Gamble, W. L. (1983). *Response of Highway Bridges to Nonlinear Temperature Distributions* (FHWA/IL/UI-201). Springfield, VA: Transportation Research Board.

Priestley, M. J. N. (1978). Design of Concrete Bridges for Temperature Gradients. *ACI Journal Proceedings*, *75*(5), 209–217.

Roberts-Wollman, C. L., Breen, J. E., & Cawrse, J. (2002). Measurements of Thermal Gradients and their Effects on Segmental Concrete Bridge. *Journal of Bridge Engineering*, *7*(3), 166–174.

Roctest. (2006). *Instruction Manual: Embedded Strain Gage Model EM-5*. Saint-Lambert, Quebec: Roctest Ltd.

Rodriguez, L. E., Barr, P. J., & Halling, M. W. (2013). Temperature Effects on a Box-Girder Integral-Abutment Bridge. *Journal of Performance of Constructed Facilities*, *28*(3), 583–591.

Shushkewich, K. W. (1998). Design of Segmental Bridges for Thermal Gradient. *PCI Journal*, *43*(4), 120–137.

Thompson, M. K., Davis, R. T., Breen, J. E., & Kreger, M. E. (1998). *Measured Behavior of a Curved Precast Segmental Concrete Bridge Erected by Balanced Cantilevering* (FHWA/TX-98/1404-2). FHWA: Washington, D.C.

Webb, G. T., Vardanega, P. J., & Middleton, C. R. (2014). Categories of SHM Deployments: Technologies and Capabilities. *Journal of Bridge Engineering*, *20*(11), 04014118.

White, L., Ryan, K. L., & Buckle, I. G. (2017). *Thermal Gradients in Southwestern United States and the Effect on Bridge Bearing Loads (224-14-803)*. Carson City, NV: Nevada Department of Transportation.

APPENDIX A
MONITORING SYSTEM OUTAGES AND MAINTENANCE

This Appendix contains a list of I-35W Saint Anthony Falls Bridge monitoring system operation and maintenance issues as well as the steps taken to address those issues. This list is in no way complete but is intended to serve as an additional reference for future troubleshooting scenarios and data analysis.

Approximate periods of data loss are given for each subsystem in Table A1. If available, detailed information on each outage is provided. Undocumented outages in the data files are reported for periods lasting longer than one day. All static system outages have been documented. Missing dynamic system data with undocumented causes are reported over the period 4/1/2010 – 6/30/2018. SOFO data missing from "C:\UMN Data Monitoring\SOFO2.csv" with undocumented causes are reported over the period 10/27/2010 – 6/8/2018.

Table A1: Monitoring system data outages.

Subsystem	Missing Data	Portion Effected	Cause
Static System	11/8/2010 – 12/15/2010	SB datalogger	A/D Power Converter Malfunction
	8/6/2016 – 10/18/2016	NB datalogger	Bad Battery
	10/2/2017 – 1/17/2018	SB datalogger	Faulty Media Converter
	10/6/2019 – 12/22/2019	SB datalogger	Server Troubles
	10/6/2019 – 12/22/2019	GK datalogger	Server Troubles
	10/6/2019 – 10/13/2019	NB datalogger	Server Troubles
Dynamic System	8/15/2009 – 9/28/2009	Nodes 1-8	Lightning
	Winter 2009 – 2010	Node 8 LPs	LP Braces Contacting Vermin Guard
	5/22/2010 – 5/26/2010	Nodes 1-8	Undocumented
	6/25/2010 – 9/19/2010	Nodes 1-8	Lightning
	10/11/2010	Nodes 1-8	Undocumented
	11/12/2010	Node 5	Undocumented
	5/1/2011	Node 5	Undocumented
	6/25/2011 – 9/13/2011	Nodes 1-8	Poor Synchronization Signal
	12/29/2011	Node 8	Undocumented
	5/19/2012	Nodes 3-8	Undocumented
	5/27/2012 – 2/5/2013	Nodes 1-8	Lightning
	2/15/2013	Nodes 7-8	Undocumented
	6/21/2013 – 8/6/2013	Nodes 4-8	Lightning
	9/5/2013	Nodes 1-8	Undocumented
	9/20/2013 – 9/23/2013	Nodes 1-8	Undocumented
	4/27/2014 – 7/11/2014	Nodes 4-8	Communication Loss
	8/21/2014 – 8/28/2014	Nodes 4-8	Lightning
	9/20/2014 – 2/9/2015	Nodes 4-8	Lightning
	1/19/2015 – 1/21/2015	Nodes 1-3	Server Issues
	6/20/2015 – 6/22/2015	Nodes 4-8	Lightning
	7/6/2015 – 7/20/2015	Nodes 4-8	Lightning
	8/7/2015 – 8/18/2015	Nodes 4-8	Communication Loss
	9/6/2015 – 9/9/2015	Nodes 4-8	Lightning
	12/20/2015 – 1/6/2016	Nodes 1-8	Server Issues
	9/6/2016 – 9/8/2016	Nodes 4-8	Communication Loss
	9/21/2016 – 9/22/2016	Nodes 3-8	Communication Loss
	11/29/2016	Nodes 1-8	Undocumented

	10/2/2017 – 1/20/2018	Nodes 4-8	Lightning
	5/28/2018 – 5/30/2018	Nodes 1-8	Lightning
SOFO System	10/27/2010 – 10/29/2010	All gages	Software, Firmware Out of Date
	2/24/2011 – 3/2/2011	All gages	Undocumented
	5/18/2011 – 5/23/2011	All gages	Undocumented
	2/7/2012 – 2/22/2012	All gages	Database File Size Limit
	6/7/2012 – 6/8/2012	All gages	Undocumented
	8/23/2012 – 8/27/2012	All gages	Undocumented
	11/23/2012 – 11/25/2012	All gages	Undocumented
	1/8/2013 – 1/13/2013	All gages	Undocumented
	9/14/2013 – 9/15/2013	All gages	Undocumented
	10/14/2013 – 11/1/2013	All gages	Undocumented
	2/1/2014 – 2/3/2014	All gages	Undocumented
	8/27/2014 – 8/28/2014	All gages	Undocumented
	9/10/2014 – 9/23/2014	All gages	Presumed Connectivity Issue
	5/11/2015 – 5/27/2015	All gages	Presumed Connectivity Issue
	7/25/2015 – 7/30/2015	All gages	Undocumented
	9/22/2015 – 10/21/2015	All gages	Undocumented
	1/4/2016 – 1/5/2016	All gages	Undocumented
	4/15/2016 – 4/29/2016	All gages	Database File Size Limit
	9/1/2016 – 9/6/2016	All gages	Undocumented
	1/6/2017 – 1/9/2017	All gages	Undocumented
	4/28/2017 – 5/1/2017	All gages	Undocumented
	9/17/2017 – 9/22/2017	All gages	Database File Size Limit
Corrosion Monitoring System	Bridge Opening – present	All gages	Data Not Understood No data collected after 5/27/2012

Corrosion Monitoring System Difficulties: Bridge Opening – present

The CorSenSys corrosion monitoring system has never been fully operational since the system was installed. No user's manual has been provided by the suppliers, and the collected data has never been fully analyzed or understood. Prior to April 14, 2011 none of the dataloggers provided data usable for any sort of monitoring. On April 14, 2011, two of the dataloggers were replaced (503 was replaced by 402, and 504 was replaced by 401). These dataloggers appear to provide data that might be usable for monitoring, but because no user's manual has been provided, interpretation of the data has proven impossible. The two remaining dataloggers were replaced on September 13, 2011 (505 was replaced by 403, 506 was replaced by 404). Again, the new dataloggers appear to provide data that might be usable, but without a user's manual interpretation has been impossible.

Linear Potentiometer Outage: Bridge Opening – 9/28/2009

The four LPs attached to the southbound bridge at Pier 4 were not collecting data at bridge opening. It was found that the LPs were operational but were not powered properly. This issue was resolved on September 28, 2009, and approximately one full year of data was lost since bridge opening.

LP Data Loss:

SB SP3 Ext:	bridge opening – 9/28/2009
SB SP3 Int:	bridge opening – 9/28/2009
SB SP4 Ext:	bridge opening – 9/28/2009
SB SP4 Int:	bridge opening – 9/28/2009

SOFO System Problems: 10/30/2008 – 1/9/2010

From October 30, 2008 until January 9, 2010, the data collection from the static system was often erratic. The system would randomly miss data readings. Although the system was scheduled to read every hour, it would occasionally skip sensors. Occasionally, these skips would be chronic, and one sensor would appear to be down for several days at a time, and these chronic problems were not necessarily unique to any particular sensor. When the system did manage to read the sensors, the strain values appeared to be reasonable. This issue was resolved by Smartec (the system supplier) on January 9, 2010 with an update to the data collection software and data-logger firmware.

SOFO Data Loss (Erratic):

Various gages:	10/30/2008 – 1/9/2010

Dynamic System Outage: 8/15/2009 – 9/28/2009

The entire dynamic system was shut down on August 15, 2008. The timing for the outage appeared to coincide with electrical storms in the area. System repairs involved replacement of the data-logger boards or repeater nodes (which connect data-logger nodes together).

Accelerometer and LP Data Loss:

Nodes 1-8:	8/15/2009 – 9/28/2009

Linear Potentiometer Erroneous Readings: Winter 2009-2010

It was discovered that the LP braces extending down to the top of Pier 3 from the interior box of southbound bridge Span 3 were colliding with the vermin guard across the expansion joint. This caused erroneous LP readings during the winter of 2009-2010. On June 18, 2010, the vermin guard was sufficiently trimmed back for all LP braces extending down to Pier 3.

Dynamic System Outage: 6/25/2010 – 9/19/2010

The entire dynamic system was shut down on June 25, 2010. The timing for the outage appeared to coincide with electrical storms in the area. Approximately half of the system (Nodes 1 through 5) was brought online on August 28, 2010. Nodes 6, 7, and 8 were brought online on September 19, 2010. System repairs involved replacement of the data-logger boards or repeater nodes.

It was found that four of the linear potentiometers had failed during the outage. The two LPs attached to the northbound bridge at Abutment 1 were replaced September 21, 2010, and the two LPs attached to Span 4 of the southbound bridge at Pier 4 were replaced September 30, 2010. For these replacements, the new LPs were mounted on the same concrete embedded bolts as were used to mount the replaced LPs.

Accelerometer and LP Data Loss:

Nodes 1-5*:	6/25/2010 – 8/28/2010
* NB SP1 Ext (LP):	6/25/2010 – 9/21/2010
* NB SP1 Int (LP):	6/25/2010 – 9/21/2010
* SB SP4 Ext (LP):	6/25/2010 – 9/30/2010
* SB SP4 Int (LP):	6/25/2010 – 9/30/2010
Nodes 6-8:	6/25/2010 – 9/19/2010

Static System Outage: 11/8/2010 – 12/15/2010

On October 28, 2010, the power supply that converted AC power to 12V DC for the fiber optic converters inside the control shed failed. This failure cut off connection between the server and dataloggers located inside the bridge. The dataloggers continued to run and collect data without continuous connection to the server. The power-supply was replaced on January 4, 2011. It was found that the northbound bridge datalogger did not lose any data; the onboard hard disk had enough storage space such that none of the data collected during the outage was overwritten. The datalogger in the southbound bridge, which collected data from more sensors but had the same size of hard disk as the northbound datalogger, overwrote data from November 8, 2010 to December 15, 2010. This data was not recoverable.

Vibrating Wire Strain Gage and Thermistor Data Loss:

Northbound Structure:	no data loss
Southbound Structure:	11/8/2010 – 12/15/2010

Dynamic System Outage: 6/25/2011 – 9/13/2011

On June 25, 2011, difficulties were encountered when attempting to collect data from Nodes 5-8 simultaneously with Nodes 1-4. Collecting Nodes 5-8 without Nodes 1-4 worked, as did collecting Nodes 1-4 without 5-8, but collecting both sets at the same time was not possible. The problem was discovered to be a poor synchronization signal between Nodes 4 and 5. On September 13, 2011, Node 5 was replaced and the issue was resolved.

Accelerometer and LP Data Loss:

Nodes 1-4:	6/25/2011, 7/6/2011 – 7/21/2011, 8/10/2011 – 8/11/2011
Nodes 5-8:	6/25/2011- 8/9/2011, 8/12/2011 – 9/13/2011

Comments:

1. During the repairs performed on September 13, 2011, an additional wire was tied from a point near the accelerometer channels of Node 5 to ground. Josh Sebasky from Minnesota Measurements stated that this was to "augment" the ground. It was noted that Ken Spikowski from Dataq found manifestations of a weak ground in the Node 5 accelerometer data (the accelerometers would occasionally and temporarily lose their 1g stable point). Josh Sebasky mentioned that the grounds used for all the Dataq nodes were tied into the lighting system, for which the electrical work was supplied by Polyphase. He believed that the ground had been weak for Node 5 ever since installation, but it would not be possible to rectify this situation short of tying to a new ground outside the lighting system. It was not clear if the weak ground at Node 5, or the grounding scheme in general, had any implications regarding the cause of the aforementioned failures, nor was it clear whether the annual summer system failures would continue in the future.

SOFO System Outage: 2/7/2012 – 2/22/2012

On February 7, 2017, an error caused no data to be collected from the SOFO sensors. A dialog box appeared that stated: *"Run-time error '3219': Operation is not allowed in this context''.* The system supplier (Smartec) was contacted and a representative created a new database file from the old one that was starting to become too large. On February 22, 2012, the new database file was online and the system began collecting data as usual.

Comments:

1. The old database file was saved as "South_Bound_exterior_Copy_2012_02_22.sdb". Some of the data on this file has never been processed to compute average hourly strains. As a result, the "C:\UMN Data Monitoring\SOFO2.csv" comma-delimited file that contains average hourly strains has data missing from 10/8/2011 to 2/22/2012.

SOFO Data Loss:

All gages:	2/7/2012 – 2/22/2012

Dynamic System Outage: 5/27/2012 – 2/5/2013

The entire dynamic system was shut down on May 7, 2012. The timing for the outage appeared to coincide with electrical storms in the area. System repairs involved replacement of the data-logger boards or repeater nodes (which connect data-logger nodes together) on January 9, 2013. Eight of the linear potentiometers were not collecting data after the system was brought back online, including NB SP1 Int, NB SP1 Ext, NB SP4 Int, SB SP 1 Ext, SB SP1 Int, SB SP3 Ext, SB SP3 Int, and SB SP4 Int. Each of these was replaced on February 5, 2013.

It was discovered that some of the multiplexer channels to which the LPs were originally connected were no longer functioning. Therefore, the LPs connected to Nodes 1, 3, and 4 were moved to new channels. The channel swap required that the Node 1 LPs be moved from collection channels 1 through 4 to channels 3 through 6. All other LPs kept the same collection channels as before. In the process of changing channels, the data from Node 4 (Southbound Span 1) were significantly altered; the data jumped substantially with respect to the previous readings on May 27, 2012. Because no evidence of substantial bridge movement was seen in any other data, it was believed that this jump was nonphysical. Channel switches on Nodes 1 and 3 did not appear to cause any notable jumps. On April 8, 2013 the LP connection at Node 4 were moved which mostly reversed the jump in readings. Following this channel swap, LP readings from Node 4 were only approximately 0.2 in. (5 mm) off from expected values from the previous year. Therefore, it was concluded that this jump in data was caused by damaged signal board channels. The channel swaps performed due to this outage are outlined in detail in (French et. al., 2014)

Accelerometer and LP Data Loss:

Node 1-2*:	5/27/2012 – 8/23/2012
* NB SP4 Int (LP):	5/27/2012 – 2/5/2013
Nodes 3-8*:	5/27/2012 – 1/9/2013
* NB SP1 Int (LP):	5/27/2012 – 2/5/2013
* NB SP1 Ext (LP):	5/27/2012 – 2/5/2013
* SB SP1 Int (LP):	5/27/2012 – 2/5/2013
* SB SP1 Ext (LP):	5/27/2012 – 2/5/2013
* SB SP3 Int (LP):	5/27/2012 – 2/5/2013
* SB SP3 Ext (LP):	5/27/2012 – 2/5/2013
* SB SP4 Int (LP):	5/27/2012 – 2/5/2013

Dynamic System Outage: 6/21/2013 – 8/6/2013

Following a lightning storm on June 21, 2013, only Nodes 1, 2, and 3 continued to collect. The remainder of the nodes were brought back online on July 8, 2013 without the replacement of any nodes. However, it was later discovered that while the Node 4 board was still operating, the data from that node was corrupt, thus indicating the need for replacement. Node 4 was replaced on August 6, 2013, resolving the issue. It was found that the linear potentiometer at Southbound Span 1 interior box was damaged; the sensor was replaced on July 25, 2013.

Accelerometer and LP Data Loss:

Nodes 1-3:	minimal data loss
Node 4*:	6/21/2013 – 8/6/2013
* SB SP1 Int (LP):	6/21/2013 – 7/25/2013
Nodes 5-8:	6/21/2013 – 7/8/2013

Dynamic System Outage: 4/27/2014 – 7/11/2014

Communication to Nodes 4 through 8 was lost on April 27, 2014, though Nodes 1, 2, and 3 still continued to collect data. On July 11, 2014, DI-720 boards were replaced at Node 3 and Node 6. Full communication to all eight nodes was regained. Upon regaining communication, Node 7 accelerometer readings were way out-of-bounds. Also, the LPs attached to Node 4 (southbound bridge Span 1) provided no signal.

Accelerometer and LP Data Loss:

Nodes 1-3:	minimal data loss
Nodes 4-8:	4/27/2014 – 7/11/2014

Dynamic System Outage: 8/21/2014 – 8/28/2014

On August 21, 2014, a presumed lightning strike silenced Nodes 4-8 of the dynamic system. Power was cycled at Node 4 on August 28, 2014 and the system was brought back online.

Accelerometer and LP Data Loss:

Nodes 1-3:	minimal data loss
Node 4-8:	8/21/2014 – 8/28/2014

SOFO System Outage: 9/10/2014 – 9/23/2014

The weekly email on September 15, 2014 pointed out that the SOFO Fiber Optic system was not responding. It was believed to be a connectivity issue. Repairs to bring the system back online included (1) making sure the COM cable was properly connected to the SOFO and (2) restarting the SOFO data logger (turn off and on the power button). Paul Reichstadt was able to get the system working on September 23, 2014.

SOFO Data Loss:

All gages:	9/10/2014 – 9/23/2014

Dynamic System Outage: 9/20/2014 – 2/9/2015

On September 20, 2014, electrical storms in the area caused Nodes 5-8 to stop communicating. Nodes 1-3 restarted recording automatically, but Nodes 4-8 could no longer be accessed. The September 20, 2014 files showed no sensor problems. On February 9, 2015, power was cycled on Node 4 and restored connection to the southbound nodes.

Accelerometer and LP Data Loss:

Nodes 1-3:	minimal data loss
Nodes 4-8:	9/20/2014 – 2/9/2015

Server Issues: 1/19/2015 – 1/21/2015

On January 19, Ken Spikowski (Dataq) noticed that the server was bogged down and was causing data acquisition problems. Paul Reichstadt was able to restart the server on January 21, 2015.

Accelerometer and LP Data Loss:

Nodes 1-3:	1/19/2015 – 1/21/2015

SOFO System Outage: 5/11/2015 – 5/27/2015

Weekly emails in pointed out that the SOFO Fiber Optic system was not responding. It was believed to be a connectivity issue, and repairs to bring the system back online included (1) making sure the COM cable was properly connected to the SOFO and (2) restarting the SOFO data logger (turn off and on the power button). The system was brought back online May 27, 2015.

SOFO Data Loss:

All gages:	5/11/2015 – 5/27/2015

Dynamic System Outage: 6/20/2015 – 6/22/2015

A presumed lightning strike caused dynamic system Nodes 4-8 to stop communicating on June 20, 2015. Cycling power on Node 4 (from inside the bridge) on June 22, 2015 allowed communications to be regained to all nodes.

Accelerometer and LP Data Loss:

Nodes 1-3:	minimal data loss
Nodes 4-8:	6/20/2015 – 6/22/2015

Dynamic System Outage: 7/6/2015 – 7/20/2015

A presumed lightning strike caused dynamic system Nodes 4-8 to stop communicating on June 20, 2015. On July 20, 2015, all nodes were found spontaneously to be responding. No other sensor problems were found.

Accelerometer and LP Data Loss:

Nodes 1-3:	minimal data loss
Nodes 4-8:	7/6/2015 – 7/20/2015

Dynamic System Outage: 8/7/2015 – 8/18/2015

In the morning of August 7, 2015, the southbound nodes (Nodes 4-8) quit communicating during the 5 minutes when acquisition was stopped during changeover of daily files. Power cycling Node 4 on August 18, 2015 allowed communication to be regained to all nodes.

Accelerometer and LP Data Loss:

Nodes 1-3: minimal data loss
Nodes 4-8: 8/7/2015 – 8/18/2015

Dynamic System Outage: 9/6/2015 – 9/9/2015

A presumed lightning strike caused dynamic system Nodes 4-8 to stop communicating on September 6, 2015. On September 9, 2015, cycling power to Node 4 allowed communication to be regained to all nodes.

Accelerometer and LP Data Loss:
Nodes 1-3: minimal data loss
Nodes 4-8: 9/6/2015 – 9/9/2015

Server Issues: 1/5/2016

Around January 5, 2016 the server crashed. Some of the dynamic system daily data files leading up to and immediately following the crash are of unusually short duration.

Unusual Accelerometer and LP Data Files:
All Nodes: 12/20/2015, 12/29/2015, 12/30/2015, 1/4/2016, 1/5/2016, 1/6/2016

SOFO System Outage: 4/15/2016 – 4/29/2016

The SOFO reading unit entered a continual reset mode upon launch for a week at the end of April 2016, due to the database file becoming too large. Paul Reichstadt was able to reset the SOFO unit.

SOFO Data Loss:
All gages: 4/15/2016 – 4/29/2016

Static System Outage: 8/6/2016 – 10/18/2016

Data was not collected from the northbound static system data logger starting August 6, 2016 because of a bad battery. The northbound data logger battery was replaced with a temporary battery on September 22, 2016. Data collection was restarted on October 18, 2016. The northbound and southbound static data logger batteries were replaced with new batteries on April 28, 2017.

Vibrating Wire Strain Gage and Thermistor Data Loss:
Northbound Structure: 8/6/2016 – 10/18/2016
Southbound Structure: no data loss

Comments:

1. Weekly emails now include static data logger battery voltages, which are taken from the most recent recordings in the static data files. Therefore, battery voltages

reported in the emails will not be current if data files are not current (i.e. due to connectivity issues that cause data loss, etc.).

Dynamic System Outage: 9/6/2016 – 9/8/2016

Nodes 4, 5, 6, 7, and 8 of the dynamic data collection system were not operational on September 6, 2016. As a result, the accelerometers and linear potentiometer data was not collected from the south bound structure. On September 8, 2016, power was cycled at Node 4 (someone had to enter the bridge and cycle power manually) and the system was operational again.

Accelerometer and LP Data Loss:

Nodes 1-3:	minimal data loss
Nodes 4-8:	9/6/2016 – 9/8/2016

Dynamic System Outage: 9/21/2016 – 9/22/2016

Nodes 3, 4, 5, 6, 7, and 8 of the data collection system were not operational on September 21, 2016. As a result, the accelerometers and linear potentiometer data was not collected from the southbound structure. On September 22, 2016, power was cycled for the entire structure and the nodes became operational again. Power cycling was achieved at ground level in an electrical box on the east side of the I-35W Northbound off ramp at University Avenue. Contact Paul Reichstadt for more information.

Accelerometer and LP Data Loss:

Nodes 1-2:	minimal data loss
Nodes 3-8:	9/21/2016 – 9/22/2016

SOFO System Outage: x 9/17/2017 – 9/22/2017

On September 17, 2017, an error caused no data to be collected from the SOFO sensors. The following error message was given in a pop-up window: *"Run-time error '-2147217887 (80040e21)': Cannot open database ''. It may not be a database that your application recognizes, or the file may be corrupt."* This error occurs when the SOFO database becomes too large and no more data can be added to the file. There is an automatic file backup that should prevent the error, but for some reason it had not been occurring. On September 22, 2017, the file was manually backed up by going to the "C:\Data\Smartec" directory and running the CloneSDB.bat executable, and normal data collection operation was restored.

SOFO Data Loss:

All gages:	9/17/2017 – 9/22/2017

Dynamic System Outage: 10/2/2017 – 1/20/2018

A dynamic system error was detected on October 2, 2017. The timing for the outage appeared to coincide with electrical storms in the area. The southbound Dataq collection Nodes 4, 5, 6, 7, and 8 would not respond to a communication PING. Power cycling did not fix the issue. Electrical circuit boards

(DI-720 A/D board) were replaced at Nodes 3, 4, 5, and 6 by October 31, 2017 and solved communication issues to all nodes. An Ethernet surge suppressor was replaced at Node 4. The following table lists the configurations of the hardware now installed:

Node	IP Address	MAC Address	Serial #
1	192.168.0.131	00:90:C2:DF:E2:7B	484D43DF
2	192.168.0.129	00:90:C2:E0:06:02	4C6D9A80
3	192.168.0.130	00:90:C2:E7:74:BA	50491C33
4	192.168.0.127	00:90:C2:D9:98:FD	4C6DA2A2
5	192.168.0.133	00:90:C2:DC:6E:DA	4AC23375
6	192.168.0.134	00:90:C2:E9:D7:45	4A8C6875
7	192.167.0.128	00:90:C2:CB:58:5A	4849A249
8	192.168.0.135	00:90:C2:E7:FB:27	4C5ADB8A

The linear potentiometer (LP) located in the exterior box of the southbound structure measuring motion relative to the south abutment (SB SP1 EXT) also began malfunctioning on October 2, 2017. It was sent to the manufacturer (UniMeasure) for repairs and re-installed in the bridge on January 18, 2018. Upon installation of the refurbished LP, it was detected that the channel in the filter board of Node 4 was malfunctioning. The SB SP1 EXT linear potentiometer was changed from filter board screw terminal 37 to screw terminal 34. This decision reordered the two LPs at Node 4 in the raw live collection file (NODE4.wdh). The change was reflected in the Dataq system with a proper name change and was addressed in the daily file (NODE4.WDH) to match the channel order from before the outage. No other changes to data monitoring software were necessary as all UMN data monitoring programs reference the daily file.

Accelerometer and LP Data Loss:

Nodes 1-3:	no data loss
Nodes 4-5*:	10/2/2017 – 10/12/2017
* SB SP1 EXT (LP):	10/2/2017 – 1/20/2018
Nodes 6-8:	10/2/2017 – 10/30/2017

Comments:

1. Two spare electrical circuit boards configured for Dataq Nodes are currently stored at the University of Minnesota (UMN). They are property of the Minnesota Department of Transportation. Configuration of the hardware stored at UMN:

Node	IP Address	MAC Address	Serial #
3	192.168.0.133	00:90:C2:E0:56:F2	4C59D834
4	192.168.0.134	00:90:C2:E9:D9:54	4AC3D2D0

Static System Outage: 10/2/2017 – 1/17/2018

Email warnings stated that no new data from the static system was being collected from the southbound data logger. After inspection, it was determined that the outage occurred on October 2, 2017 due to a communication issue between the server and southbound data logger caused by a faulty fiber optic to Ethernet media converter located in the bridge. The conclusion that the media converter was at fault was a difficult one to come to, as communications from the server shed through the faulty converter to a laptop could be achieved but the server could not PING the data logger through the converter. A laptop could directly connect to the data logger and it could be seen that the logger was

functioning properly, therefore the media converter was presumed to be malfunctioning. The faulty converter was replaced on February 6, 2018 and communication to the southbound data logger was regained. The southbound bridge datalogger overwrote data from October 2, 2010 to January 17, 2010. This data was not recoverable.

Vibrating Wire Strain Gage and Thermistor Data Loss:

Northbound Structure: no data loss

Southbound Structure: 10/2/2017 – 1/17/2018

Comments:

1. The southbound data logger can store approximately two weeks worth of data before being overwritten.

Dynamic System Outage: 5/28/2018 – 5/30/2018

Ken Spikowski (Dataq) noticed that the dynamic system went down May 28, 2018. The timing for the outage appeared to coincide with electrical storms in the area. Power cycling the dynamic system at the breaker box caused all of the nodes to come back online on May 28, 2018.

Accelerometer and LP Data Loss:

Nodes 1-8: 5/28/2018 – 5/30/2018

Static System Error: 7/9/2018

Email warnings on July 9, 2018 stated that no new static system data was being collected from the northbound or southbound data loggers. After inspection at the server shed, Paul Reichstadt noticed that the power supply connection for the media converters was unreliable. He reconnected the connection and solved the connectivity issues on July 9, 2018. The lack of temperature readings from the static system outage also caused a partial dynamic system failure flag in the weekly I-35W Server email. The dynamic system error was triggered by a failure in the MATLAB daily processing routine when trying to combine the available dynamic system linear potentiometer readings with unavailable static system temperature readings. Because of the available memory on the static system data loggers, no static system data was lost.

Monitoring System Code Error: 7/16/2018

On July 16, 2018, no status emails were sent from the bridge server. The cause was due to data processing using MATLAB and was not a data collection error. No data was lost. When conducting the linear potentiometer monitoring system checks, the system wanted to report a 'red' flag for the long-term slope check for the SB Span 1 linear potentiometer data. However, a bug in the code cause an error before the reporting emails could be sent. The file "C:\UMN Data Monitoring\UM_Driver.m" was edited on 8/3/2018 to fix the cause of the error. The previous version of the file was saved to "C:\UMN Data Monitoring\UM_Driver – Copy_2018.8.3.m".

Linear Potentiometer Monitoring System Red Flag: 8/3/2018 – 12/22/2019

The linear potentiometer (LP) monitoring system returned a red flag for the southbound Span 1 long-term slope status beginning 8/3/2018. A review of the current state of the monitoring system checks is given in Appendix B.

Dynamic System Prototype Amplifier Board: 10/16/2018

A 16-channel prototype filter board was installed on acquisition channels 17-32 of dynamic junction box "Node 6" on October 16, 2018. The prototype filter board was intended to increase resolution of the acceleration measurements by applying a 1 volt offset and 10x gain to the sensor signal prior to being read by the data acquisition system. The prototype filter board is shown in Figure A.1. The offset and gain was selectable by jumpers on the filter board, meaning that the offset and gain could be applied or not applied to individual channels. Figure A.2 shows the circuit board design. The offset and gain was applied to channels recording accelerometers that measured vertical accelerations, as the baseline reading of the DC accelerometers was -1g. The prototype filter board was a plug and play with the existing system, and no changes to the sensor channel order were made. If the offset and gain were bypassed for a specific channel, the filter had the same specifications as the previous filter board. The original filter board still functions and, as of 5/31/2019, is stored at the University of Minnesota.

Prototype Filter Board Specifications:

10x gain, 159Hz -3dB roll-off, with a 1V selectable offset, and bypass

Static System Outage: 10/06/2019 – 12/22/2019

The dynamic system got stuck on a file it was unable to open, so while the program was not running the static data was unable to be stored past two weeks. This caused the data between the beginning of October and two weeks before it was fixed to be lost. This data is unrecoverable.

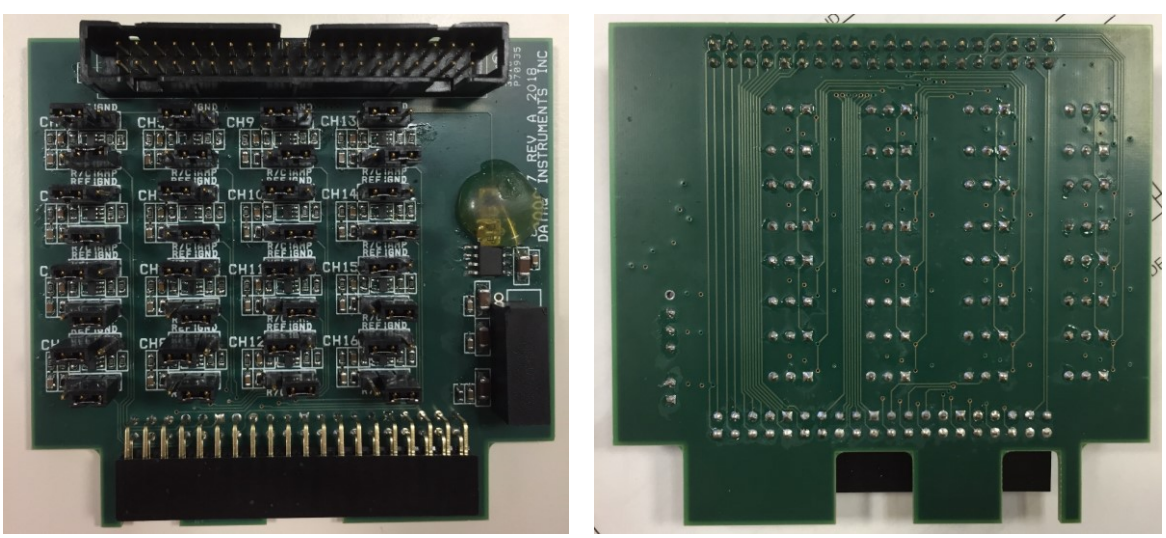

Figure A.1: Prototype filter board installed on acquisition channels 17-32 of dynamic system Node 6.

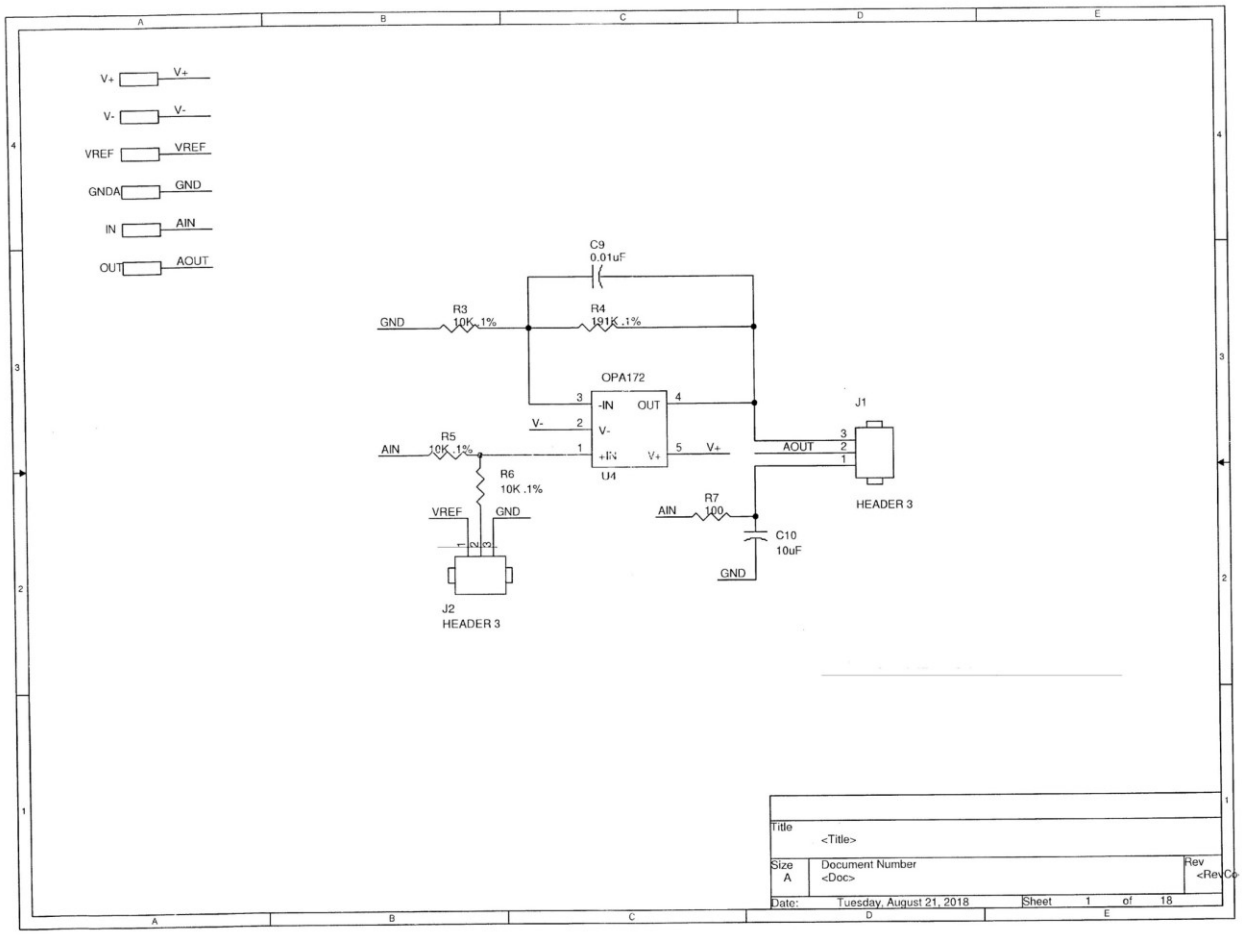

Figure A.2: Circuit board design supplied by Dataq.

APPENDIX B
LINEAR POTENTIOMETER MONITORING SYSTEM CHECKS THROUGH APRIL 18, 2019

The monitoring framework developed in French et al. (2014) is used to detect short-term and long-term anomalies in the linear potentiometer (LP) data. The short-term check was intended to detect anomalies related to immediate deviations from expected time-dependent behavior, or anomalies developing over a time frame less than one month. Such anomalies might be caused by bearing lockup or monitoring system failure. The long-term check was constructed to characterize trends over several years to ensure that the structure was behaving as expected. Thresholds for flagging anomalies were set sufficiently high to minimize false positives from the measured data while aiming to maximize the system responsiveness to true positives. Warning flags were issued in status emails if a certain number of readings were outside of the expected bounds. The developed methodology was intended only as a baseline level of structural monitoring, in that the framework could identify the presence of data anomalies but not determine the exact causes.

The figures provided in this Appendix contain measurements from the beginning of data collection through April 18, 2019. Short-term and long-term check calculations incorporate time using the Arrhenius adjusted age of the structure; however, for easy interpretation, the data presented in this Appendix is often plotted with respected to unadjusted time.

The limits for the short-term check were based on Bayesian regression, which was used to combine the uncertainty in the time-dependent models with the uncertain measurements to arrive at rational bounds for defining anomalous results in the LP time-dependent displacements. The bounds for the short-term check on the LP data from southbound Span 1, southbound Span 3, northbound Span 1, and northbound Span 3 are shown in Figure B.1. The time-dependent behavior of the northbound and southbound bridges was similar. A comparison of the northbound and southbound bridge time-dependent LP measurements and short-term checks are shown in Figure B.2. No anomalies were flagged by the short-term monitoring system over the period 7/1/2018 – 4/18/2019.

The long-term check tracked the rate of time-dependent deflections with respect to the Arrhenius adjusted age. Time-dependent rates were computed by fitting the log-power curve to data windows with duration equal to 500 adjusted age days (approximately two unadjusted years), and then computing the derivative of the fit. Weighted linear regression using the power curve was used to extrapolate the expected rates of time-dependent behavior, with bounds chosen to minimize false positive flags. The slopes of the time-dependent displacements plotted in Figure B.1 are shown in Figure B.3. The time-dependent rates are plotted at the beginning of the 500 adjusted age day calculation window. The Span 1 and Span 3 time-dependent rates for each structure are plotted together in Figure 4 to compare the behavior of the northbound and southbound bridges. Because of the similarity of the time-dependent behavior of the northbound and southbound bridges, the time-dependent rates of the two structures were also similar.

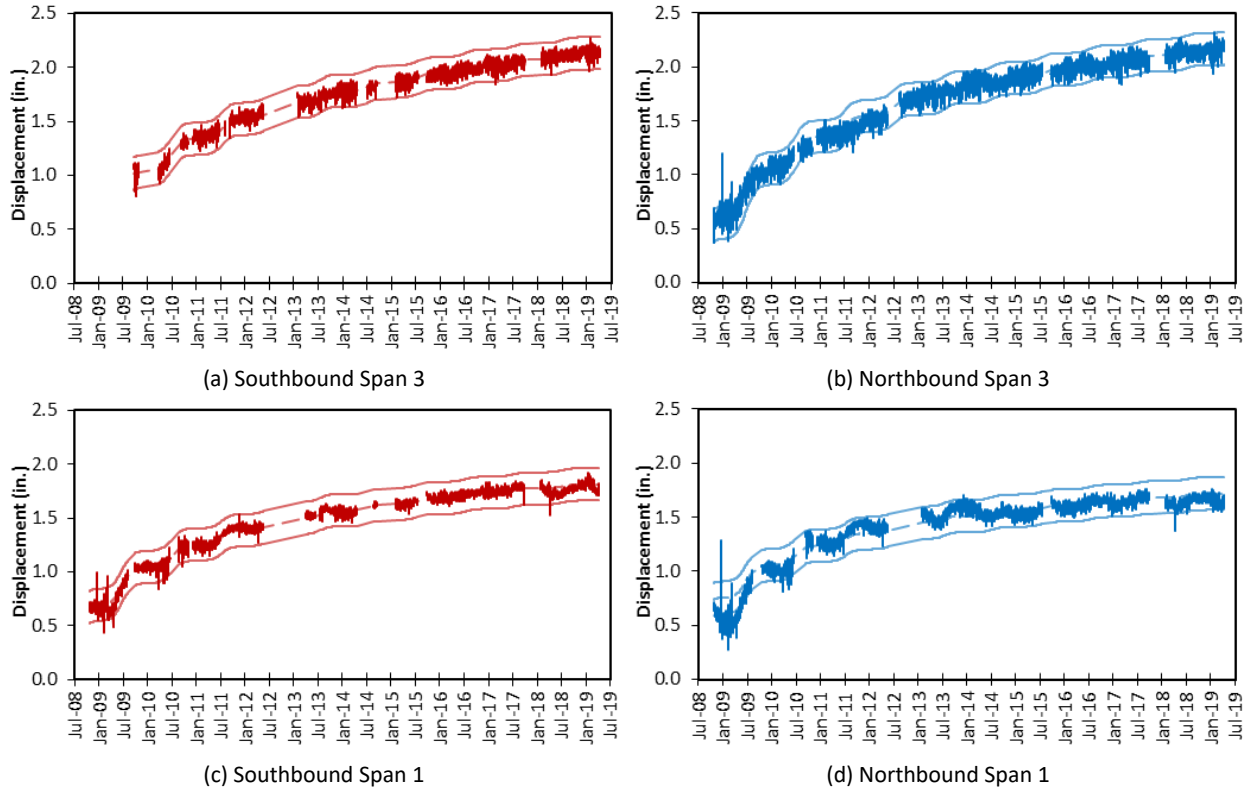

(a) Southbound Span 3

(b) Northbound Span 3

(c) Southbound Span 1

(d) Northbound Span 1

Figure B.1: Time-dependent linear potentiometer data with short-term check. Mean (dashed line) and bounds (solid line) computed using Bayesian regression with 1990 CEB/FIP Model Code model.

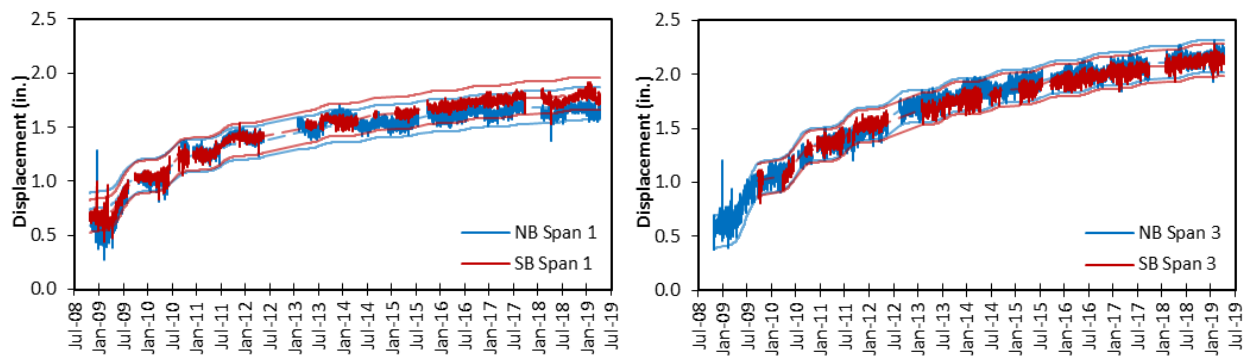

(a) Span 1

(b) Span 3

Figure B.2: Time-dependent linear potentiometer data with short-term check comparison of northbound and southbound structures. Mean (dashed line) and bounds (solid line) computed using Bayesian regression with 1990 CEB/FIP Model Code model.

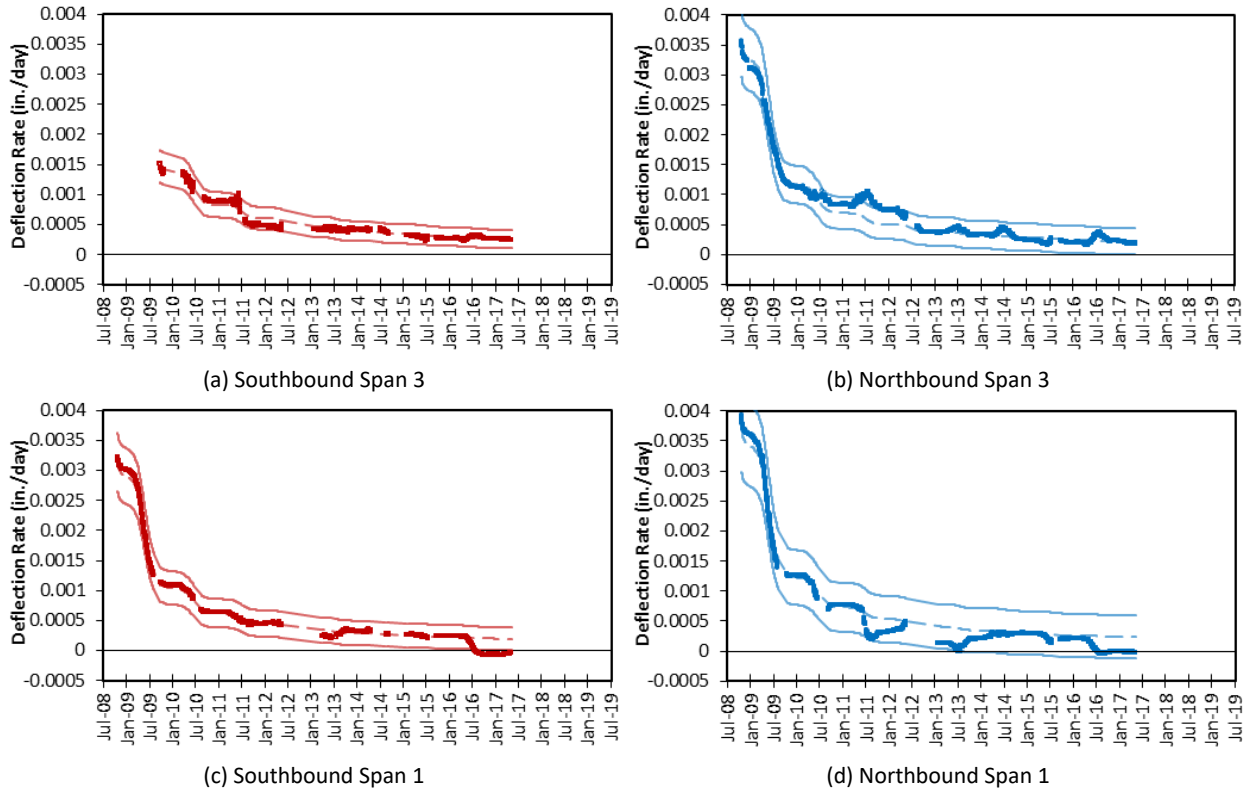

(a) Southbound Span 3

(b) Northbound Span 3

(c) Southbound Span 1

(d) Northbound Span 1

Figure B.3: Time-dependent linear potentiometer data with long-term check. Mean (dashed line) computed using weighted linear regression and bounds (solid line) chosen by inspection to minimize false positives on the measured data.

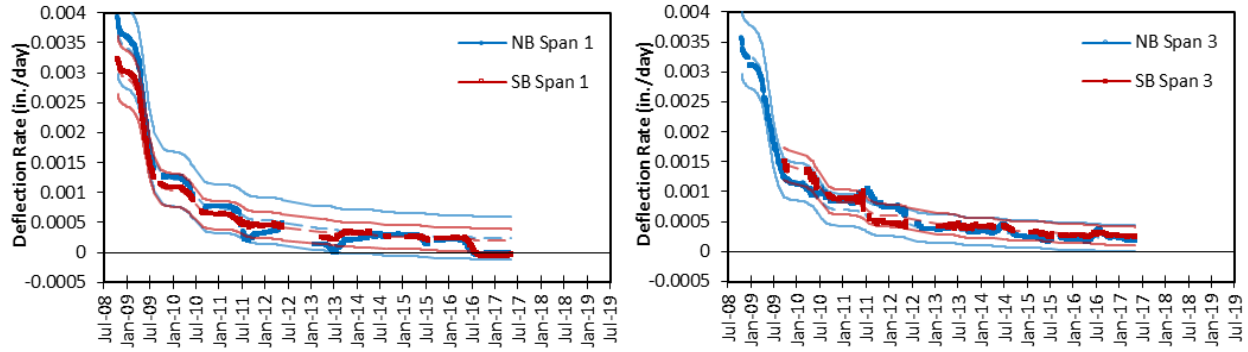

(a) Span 1

(b) Span 3

Figure B.4: Time-dependent linear potentiometer data with long-term check comparison of northbound and southbound structures. Mean (dashed line) computed using weighted linear regression and bounds (solid line) chosen by inspection to minimize false positives on the measured data.

SOUTHBOUND SPAN 1 LONG-TERM SLOPE STATUS: RED FLAG

The monitoring system returned a red flag for the southbound Span 1 long-term slope status beginning August 3, 2018 until December 22, 2019. The short- and long-term checks for both the southbound Span 1 and northbound Span 1 linear potentiometer data, zoomed to recent data causing the red flag, are shown in Figure B.5. The downward trend of the deflection rate beginning around May 2016 (Figure B.5b) was due to the abnormal cyclic time-dependent displacement data (Figure B.5a) observed after the data outage from 10/2/2017 to 2/3/2018. Both northbound Span 1 and southbound Span 1 time-dependent displacements exhibited similar behavior following 2/3/2018, and therefore the deflection rate for the two bridges was also similar.

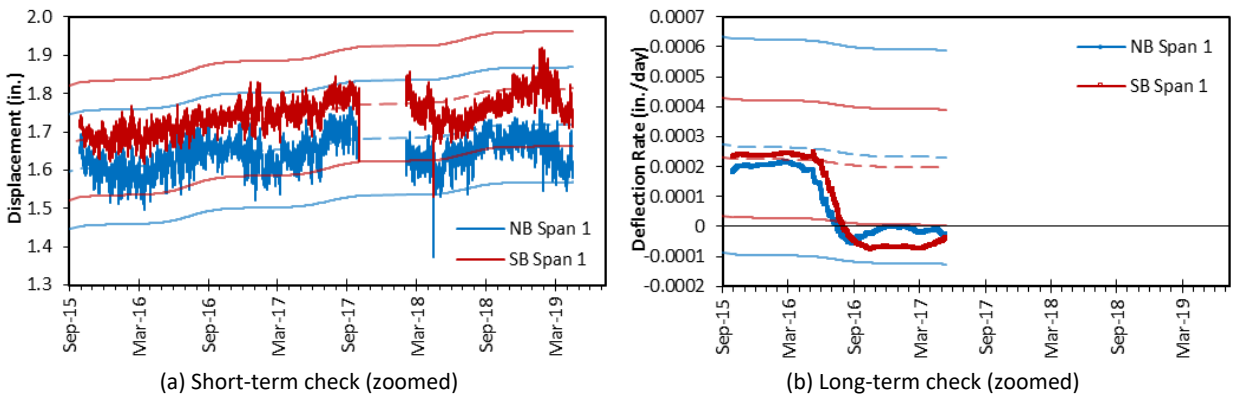

Figure B.5: Time-dependent linear potentiometer southbound Span 1 and northbound Span 1 data with short- and long-term checks.

Only the southbound Span 1 long-term check reported anomalous behavior following the data outage, despite the southbound Span 1 and northbound Span 1 time-dependent displacement behavior being similar. The reason for this discrepancy is the upper and lower bounds used to trigger an anomaly flag in the long-term check. As was mentioned previously, the expected rates of time-dependent behavior (dashed lines in Figure B.5b) were determined by weighted linear regression using the power curve, with the bounds chosen to minimize false positive flags. The training set for performing the regression on the computed slopes was all the data windows for slope computation that contained the first year of measured data. Because the window size for computing the slope was approximately two years, the training set effectively contained information from the first three years of time-dependent behavior. The upper and lower bounds were the mean plus or minus the summation of 10% of the mean estimate and 3 times the standard deviation of the residual of the regression with respect to the training set data. The residual of the regression with respect to the training set data was larger for the northbound Span 1 slope data set compared to the southbound Span 1 slope data set, which resulted in wider bounds for the northbound Span 1 long-term check. Thus, no long-term anomalous behavior was flagged for northbound Span 1, despite the similarity with southbound Span 1.

Inspection of the rates of time-dependent behavior in the northbound bridge and southbound bridge during the time of the southbound Span 1 long-term red flag showed that, in the data windows

beginning 2,000 to 2,300 adjusted age days (and ending at 2,500 to 2,800 (April 2019) adjusted age days, respectively), the Span 1 deflection rate decreased while the Span 3 rate increased, as shown in Figure B.6. The total rate of the contraction of the northbound and southbound bridges, shown in Figure B.7, appeared to consistently decrease, but more of the contraction was transferred to the north ends of the bridges than to the south ends. Similar behavior was previously observed in the northbound bridge (windows beginning 700 to 1,000 adjusted age days). The reason for this behavior was unclear, but one possibility may be that the structures tend to "walk" toward Abutment 1. Another possibility may be that Abutment 1 is not perfectly fixed, as was assumed for the extraction of the time-dependent deflections; it may move or settle with time.

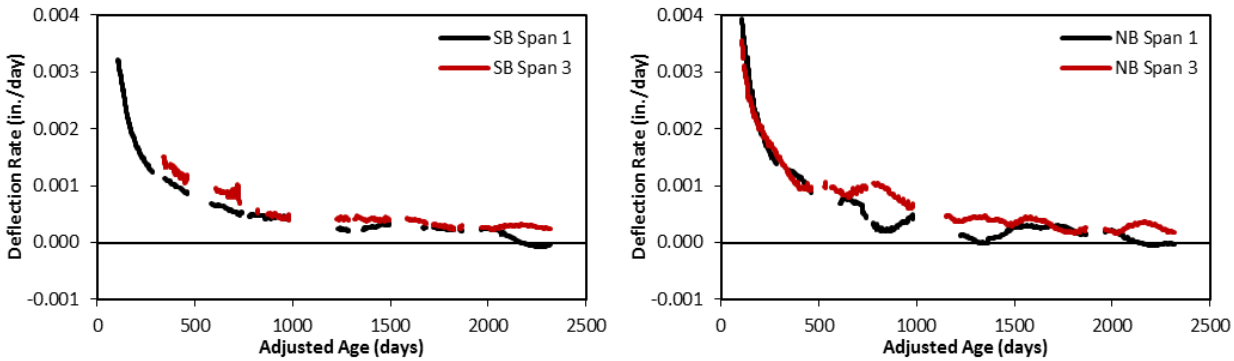

(a) Southbound Bridge (b) Northbound Bridge

Figure B.6: Adjusted-age rate of time-dependent deflections at expansion joints plotted with respect to adjusted age.

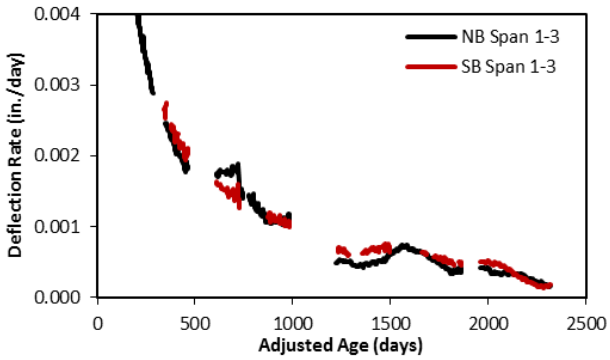

Figure B.7: Adjusted-age rate of time-dependent deflections of combined Span 1 and Span 3 linear potentiometer data plotted with respect to adjusted age.

OBSERVATIONS FROM RED FLAG INVESTIGATION

The southbound Span 1 long-term anomaly red flag beginning August 3, 2018 highlighted several possible shortcomings of the long-term anomaly detection algorithm. Changing the long-term anomaly detection routine on the I-35W bridge server was beyond the scope of this work; however, some possible improvements are proposed.

Given that the northbound and southbound structures are alike and the observed behavior tracks closely, the long-term behavior of both structures is likely to be similar. Therefore, the rule chosen to define the upper and lower bounds for the long-term anomaly detection scheme should result in expectation intervals (bounds) that are similar for corresponding locations on the two structures. For example, if similar anomalous behavior is observed on both structures, such as is the case with the time-dependent rates at northbound Span 1 and southbound Span 1, the long-term anomaly detection routine should ideally detect the abnormal behavior at both locations rather than at only one. A possible improvement to the long-term anomaly detection routine may involve hard coding upper and lower long-term check bounds for corresponding locations on the two structures (e.g., northbound Span 1 and southbound Span 1 have similar bound widths, and northbound Span 3 and southbound Span 3 have similar bound widths), where the bounds are chosen to detect rate behavior that is deemed abnormal.

The 500-adjusted age day (approximately two unadjusted years) window size used to compute the time-dependent rates was intended to minimize the impact of seasonal effects. Now that the seasonal dependence of the time-dependent displacements plays a relatively larger role in the bridge time-dependent behavior than earlier in the bridge's life when creep and shrinkage dominated longitudinal displacement behavior, missing data may impact the slope calculation to a greater extent in older age. Improving the long-term system checks in this regard may not be straightforward, unless the time-dependent extraction methodology was improved upon to reduce the seasonal dependence of the time-dependent displacements.

With the large amount of data from the structure in a presumed undamaged state, it is possible that Bayesian regression may be able to be used to provide bounds for detecting anomalies that occur over periods of months or even years. French et al. (2014) suggested that the Bayesian regression approach used in the short-term check should not be relied upon to detect long-term bridge behavior changes, as the methodology cannot distinguish (without prior knowledge) between a true positive due to structural deterioration and a false positive triggered by imprecise estimation of the time-dependent behavior. However, with over ten years of data, it may now be possible to use Bayesian regression to provide reliable bounds for detecting long-term anomalous behavior.

As a preliminary analysis, various durations for the Bayesian regression training set were investigated to characterize the reliability of the regression for long-term anomaly detection. Training sets included the first year of data, the first three years of data, the first five years of data, and the first ten years of data. In terms of Arrhenius-adjusted age, the 1-year, 3-year, 5-year, and 10-year training sets had durations of approximately 250, 750, 1250, and 2500 adjusted age days, respectively. The test set for each case

consisted of all data collected after the training set until April 18, 2019. The results from Bayesian regression on the time-dependent linear potentiometer data are presented in Figures B.8 and B.9 for Span 1 and Span 3 of the southbound bridge, respectively. The plots show the mean estimates using each of the time-dependent models for the training set durations specified previously. The consistency of the curve fit as the duration of the training set was expanded was used as a qualitative metric for the goodness of fit. For example, both CEB/FIP Model Code estimates were fairly consistent as the training set expanded for the southbound linear potentiometer data, implying that the early age behavior of the southbound structure could be fit well by both CEB/FIP models. However, this result did not guarantee that the long-term estimate given by the CEB/FIP models were accurate, but only that the fit was consistent for the first 10 years of collected data. As more data was used in the regression, the posterior estimates (i.e., the FEM estimates updated using measurements) from the different models converged. Therefore, it may be possible to implement the Bayesian regression methodology for long-term anomaly detection with a large amount of measured data.

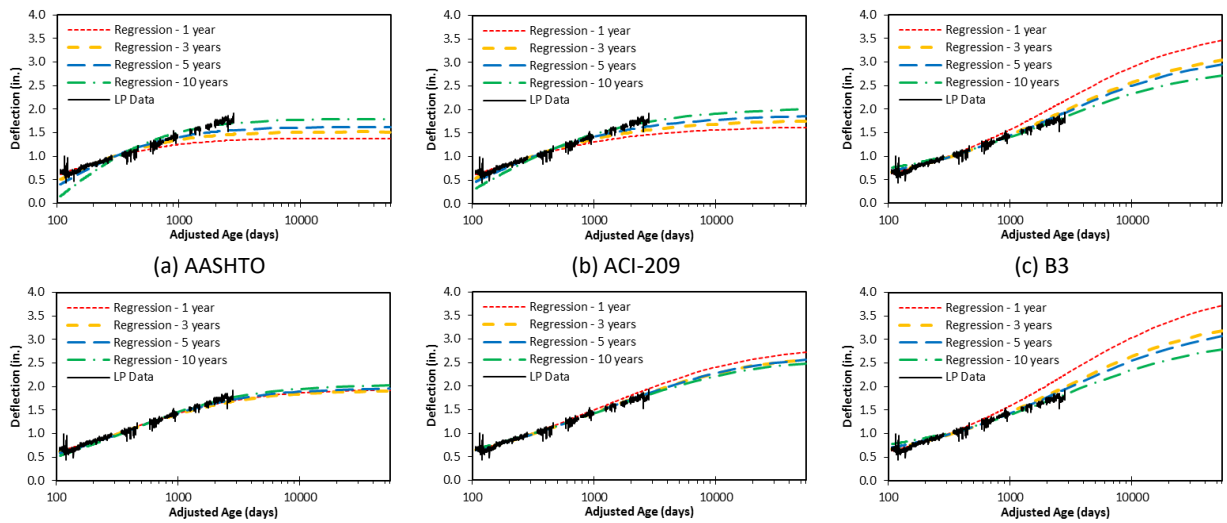

(a) AASHTO (b) ACI-209 (c) B3

(d) CEB/FIP Model Code 1978 (e) CEB/FIP Model Code 1990 (f) GL2000

Figure B.8: Bayesian regression of time-dependent linear potentiometer data from southbound bridge Span 1.

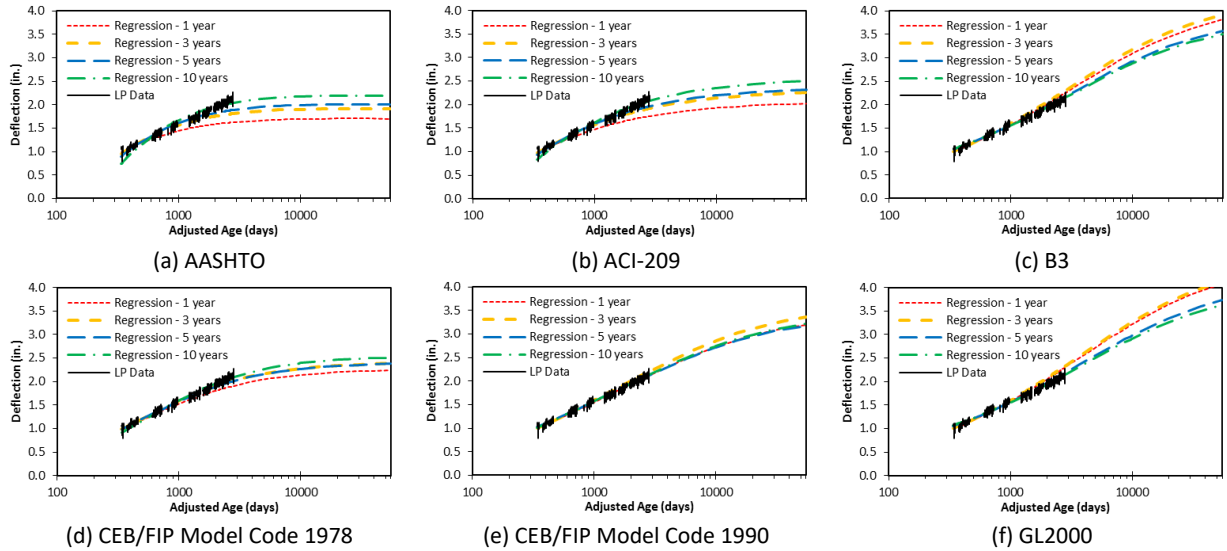

Figure B.9: Bayesian regression of time-dependent linear potentiometer data from southbound bridge Span 3.

In addition to considering possible improvements to the detection algorithms, several observations were made when analyzing the time-dependent data to determine the cause of the red flag for the southbound Span 1 long-term slope status beginning August 3, 2018.

When little to no temperature variation is measured through the depth of the cross section over an extended period of time (e.g., several days), the linear regression model may not accurately capture the behavior of the linear potentiometer readings over that time period. Such was the case for measured northbound and southbound Span 1 data over April 16, 2018 – April 18, 2018. A large regression approximation residual resulted in a spike in the time-dependent displacement data that was likely not representative of the movements at the Span 1 expansion joint.

In this work, time was corrected using a single Arrhenius adjusted age for the entire structure, calculated using temperature measurements at Location 7 (midspan of river span) of the southbound structure. Assigning an adjusted time derived from average bridge temperature was only as good as the assumption that the temperature at a single cross section was representative of the average temperature of the bridge (French et al. 2014). Using a different characterization of the average bridge temperature (e.g., calculated using a reduced number of temperature measurements) may introduce additional errors when comparing measurements to constant-temperature finite element analysis predictions.

An analysis was conducted to determine if fewer temperature sensors could be used in the calculation of the average and gradient temperature terms in the linear regression to extract the time-dependent behavior of the measured data. Such a question is reasonable to ask, as if a similar monitoring system were to be implemented on structures in the future, it would be desirable to know the minimum quantity of temperature sensors needed through the depth of the cross section to perform the task of time-dependent behavior extraction. For the I-35W St. Anthony Falls Bridge monitoring work involving

the linear potentiometers, isolation of the time- and temperature-dependent components of the data was accomplished using measurements from nine thermistors (six in the deck and three in the webs) at Location 7 of the southbound structure. At Location 7 of the northbound structure, four sensors measuring temperature (one in the deck, one in the web, and two in the bottom flange) were available. The northbound Location 7 sensors were not able to capture the temperature gradients in the deck; thus, the interpolated temperature profile through the depth of the cross section was significantly different for the northbound four-sensor case as compared to the southbound nine-sensor case. As a result, the area-weighted average temperature and temperature gradient terms used in the linear regression were different for the northbound four-sensor and southbound nine-sensor cases. Even though the temperature functions used in the linear regression were different, similar time-dependent displacements were extracted from the linear potentiometer data using the northbound four-sensor case and the southbound nine-sensor case.

Figure B.10 shows the short- and long-term checks on the linear potentiometer data using both the nine-sensor arrangement at southbound Location 7 (default) and the four-sensor arrangement at northbound Location 7. The differences between the southbound nine-sensor case and the northbound four-sensor case for the short-term check (Figure B.10a) were negligible. As mentioned previously, the Arrhenius adjusted age is dependent on the average bridge temperature characterization, which meant that the four-sensor case returned an adjusted age of 2968 adjusted age days (as opposed to 2817 adjusted age days for the southbound 9-sensor case) for April 18, 2019. As a result, the rate of time-dependent deflections calculated with respect to the Arrhenius adjusted age (Figure B.10b) were different for the four-sensor case and nine-sensor case. The northbound four-sensor case long-term bounds shown in Figure B.10b were determined using the rule prescribed for the southbound nine-sensor case. The wider bounds calculated for the northbound four-sensor case show that the algorithm chosen to determine the long-term bounds should be considered on a case-by-case basis. Nevertheless, it was concluded that a monitoring system relying on the four-sensor arrangement at Location 7 of the northbound bridge could provide similar anomaly detection capabilities as the current nine-sensor arrangement.

SUMMARY OF LP MONITORING SYSTEM STATUS

The following bullet points summarize the linear potentiometer monitoring system status red flag from 8/3/2018 through 12/22/2019:

- The monitoring system of the time-dependent linear potentiometer data has identified anomalous long-term deflections that would have been impossible to distinguish using the raw linear potentiometer data alone.
- From August 3, 2018 to December 22, 2019, the southbound Span 1 long-term slope status has returned a red flag, signaling anomalous long-term time-dependent behavior.

- While the monitoring system identified anomalous long- behavior in the southbound Span 1 data only, similar behavior was observed in the northbound Span 1 data.
- The total rate of the contraction of the northbound and southbound bridges appeared to consistently decrease, but more of the contraction was transferred to the north ends of the bridges than to the south ends.
- To continue serving its purpose in an effective manner, the long-term check algorithm may need to be updated to reflect the measured time-dependent behavior of the structure and other recent observations.

.

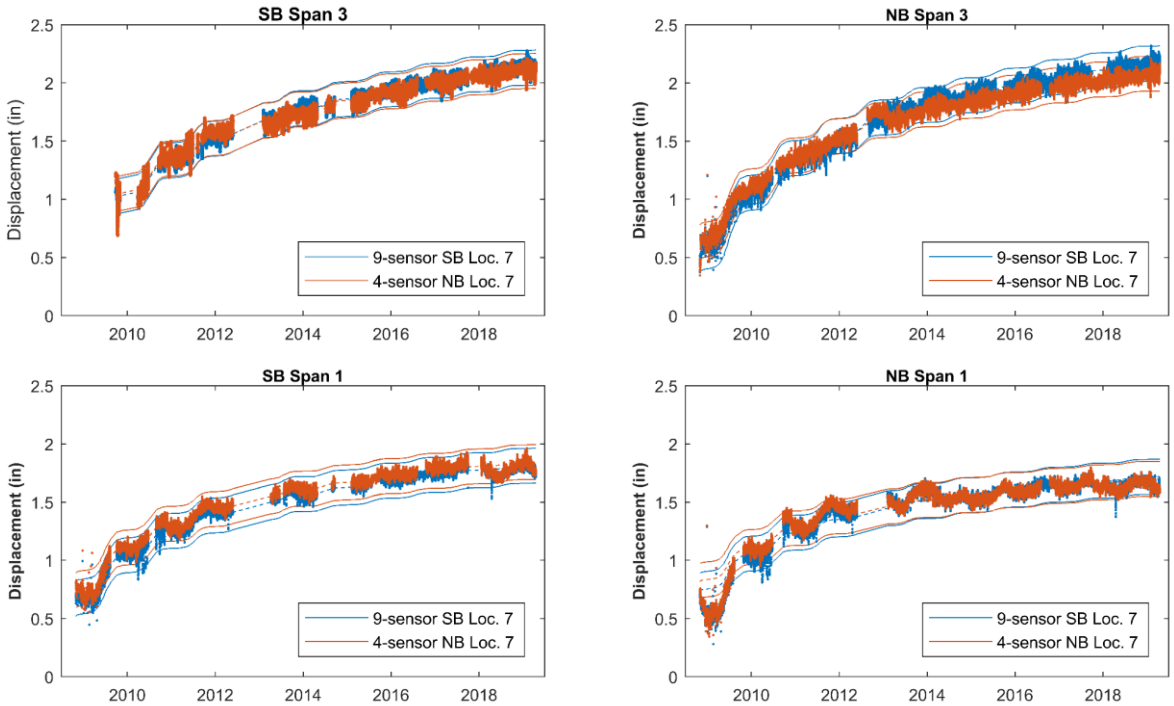

(a) Short-term check

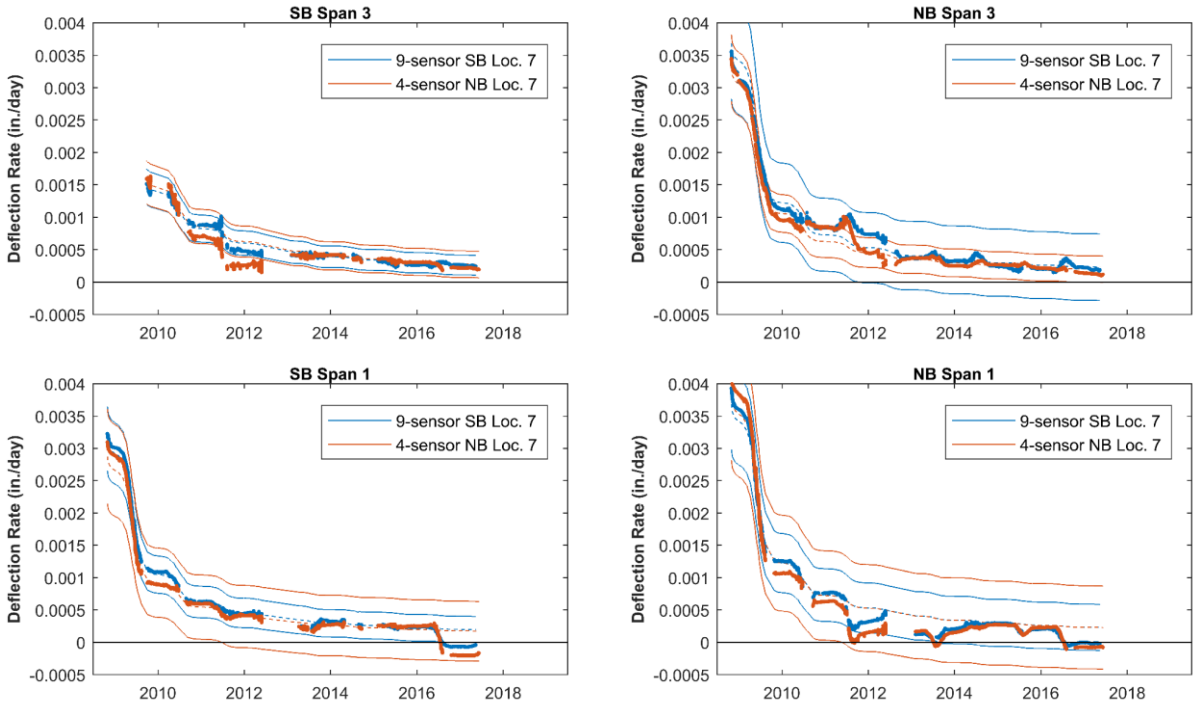

(b) Long-term check

Figure B.10: Time-dependent linear potentiometer data with short- and long-term checks, computed using 9-sensor arrangement at southbound Location 7 (default) and 4-sensor arrangement at northbound Location 7.